Sapienza University of Rome

Department of Astronautical, Electrical and Energy Engineering
PhD in Engineering and Applied Science for Energy and Industry

Thesis For The Degree Of Doctor Of Philosophy

Thermal Energy Storage integration in electrical grids and in energy industries for decarbonization

Thesis Advisors

Prof. Maria Carmen Falvo

Eng. Rocco Sorrenti

Candidate

Antonio Scafuri

2002558

Academic Year 2023-2024 (XXXVII cycle)

“Se tu puoi!

Tutto è possibile

per chi crede”

[Marco 9:23]

Abstract

In the current global context, where it is essential to comply with greenhouse gas emission limits to avoid surpassing the increase in average global temperature, renewable energy sources must replace traditional fossil fuels in the production of both electrical and thermal energy across various sectors, including industry. The inherent unpredictability of renewable energy sources makes it challenging to align energy production with real-time demand. For this reason, the introduction of energy storage systems is crucial, as they play a key role in balancing supply and demand. These systems allow for the storage of excess energy produced during periods of low demand, which can then be released when demand is higher, ensuring a more stable and reliable energy system.

In the various sectors where energy is required, numerous solutions are being proposed for energy storage technology. This doctoral thesis focuses on thermal energy storage systems for steam supply in industrial applications. Specifically, two types of storage systems based on fluidized sand beds will be presented: one charged directly by solar energy and the other by electrical energy. Both systems were designed and patented by Magaldi Power S.p.A. and are named STEM® (Solar Thermo-Electric Magaldi) and MGTES (Magaldi Green Thermal Energy Storage), respectively.

For the STEM® technology, which uses solar energy for charging, two innovative aspects stand out: an advanced algorithm for the integral correction of heliostat (solar tracking mirrors) aiming errors, which improves aiming accuracy and consequently increases the amount of solar energy collected in the fluidized bed; and the use of a biaxial inclinometer for each heliostat, which helps to reduce aiming errors caused by ground misalignments, thus improving system reliability.

For the MGTES technology, which utilizes electric resistances to charge thermally through Joule heating, a study was conducted to identify the most suitable heating system for the fluidized bed of sand particles. Simulations were carried out based on analytical models, comparing resistive elements designed to heat through conduction, convection, and radiation. Following the simulation phase, an experimental testing campaign was conducted to validate the results of the theoretical models, verifying the accuracy of the simulations and the actual performance of the heating systems studied.

To identify the most promising heating method, a qualitative analysis was performed alongside the quantitative assessment, aimed at evaluating critical factors relevant to the industrialization of technology. Key considerations included ease of installation, maintenance requirements, component replaceability, and compatibility of the technology with the storage medium. A strengths, weakness, opportunities, and threats analysis was conducted, encompassing the primary qualitative factors mentioned. The resulting matrices were then structured to systematically evaluate these aspects.

In the proposed scenario, where thermal storage systems are integrated within energy districts, a novel controlled microgrid concept becomes essential. In this framework, both electrical and thermal storage systems require optimal management. An effective Energy Management System (EMS) is critical to the efficient utilization of distributed energy resources. Considering these requirements, research has been initiated to develop an EMS model aimed at optimizing power flows to reduce both energy costs and CO_2 emissions. This topic will form the core of future research efforts.

Nello scenario mondiale attuale dove si rende necessario rispettare i limiti di emissione di gas serra per non valicare l'incremento della temperatura media globale, le fonti di energia rinnovabile dovranno sostituire i tradizionali combustibili fossili nella produzione di energia elettrica e termica nei vari settori incluso quello industriale. La non programmabilità intrinseca delle fonti di energia rinnovabili rende difficile far coincidere l'energia prodotta con la domanda in tempo reale. Per questo motivo, l'introduzione di sistemi di accumulo di energia è fondamentale, in quanto svolgono un ruolo chiave nel bilanciare la domanda e l'offerta. Questi sistemi consentono di immagazzinare l'energia in eccesso prodotta durante i periodi di bassa domanda, che può poi essere rilasciata quando la domanda è più alta, garantendo così un sistema energetico più stabile ed affidabile. Nei vari settori dove si necessità di energia, sono svariate le soluzioni che si propongono come tecnologia di accumulo. In questo lavoro di tesi di dottorato ci si focalizza sui sistemi di accumulo termico per la fornitura di vapore nel comparto industriale. In particolare, si presenteranno due tipi di sistemi di accumulo basati su letto fluidizzato di sabbia uno a carica solare diretta l'altro a carica elettrica. Entrambi i sistemi sono stati ideati e brevettati dalla Magaldi Power S.p.A. e denominati rispettivamente STEM® (Solar Thermo-Electric Magaldi) ed MGTES (Magaldi Green Thermal Energy Storage).
Per la tecnologia STEM®, per cui si prevede la carica solare, sono due gli aspetti innovativi da evidenziare: un algoritmo innovativo che prevede la correzione integrale degli errori di puntamento degli eliostati (specchi inseguitori solari) garantendo una maggiore efficienza di puntamento e quindi un incremento dell'energia solare raccolta all'interno dello letto fluido; l'utilizzo di un inclinometro biassiale per ogni eliostato, per aumentare la reiezione degli errori di puntamento dovuti a disallineamenti del terreno, migliorando così l'affidabilità del sistema.
Per la tecnologia MGTES, che prevede una carica termica mediante resistenze elettriche per effetto Joule, è stato realizzato uno studio per l'individuazione del sistema di riscaldamento più adatto al letto fluidizzato di particelle di sabbia. Sono state condotte simulazioni basate su modelli analitici confrontando elementi resistivi progettati per riscaldare attraverso conduzione, convezione e irraggiamento. Dopo la fase di simulazione, è stata realizzata una campagna di prove sperimentali per validare i risultati ottenuti dai modelli teorici, verificando l'accuratezza delle simulazioni e il comportamento reale dei sistemi di riscaldamento studiati.
Per identificare il metodo di riscaldamento più promettente, accanto alla valutazione quantitativa è stata eseguita un'analisi qualitativa, volta a valutare i fattori critici rilevanti per l'industrializzazione della tecnologia. Le considerazioni principali hanno riguardato la facilità di installazione, i requisiti di manutenzione, la sostituibilità dei componenti e la compatibilità della tecnologia con il mezzo di accumulo. È stata condotta un'analisi dei punti di forza, debolezza, opportunità e minacce, che comprendeva i principali fattori qualitativi menzionati. Le matrici risultanti sono state poi state strutturate per valutare sistematicamente questi aspetti.
Nello scenario proposto, in cui i sistemi di accumulo termici sono integrati nei distretti energetici, diventa essenziale un nuovo concetto di microgrid controllata. In questo contesto, sia i sistemi elettrici che quelli di accumulo termico richiedono una gestione ottimale. Un efficace *Energy Management System* (EMS) è fondamentale per l'utilizzo efficiente delle risorse energetiche distribuite. Tenendo conto di questi requisiti, è stata avviata una ricerca per sviluppare un modello di EMS volto ad ottimizzare i flussi di potenza per ridurre sia i costi energetici sia le emissioni di CO_2. Questo argomento costituirà il fulcro dei futuri sforzi di ricerca.

Contents

List of Figures......6

List of Tables......9

Acronyms......10

Chapter 1 Introduction......13

1.1 Global Warming......13

1.2 CO_2 emissions reductions pathway......15

1.2.1 CO_2 emissions mitigation......16

1.2.2 RES penetration......17

1.2.3 TES for driving the RES penetration......19

1.3 TES for Industrial decarbonization......22

Chapter 2 State of art of TES......27

2.1 Overview of TES......27

2.2 Latent Heat Storage......28

2.3 Thermochemical storage......30

2.4 Sensible Heat - Heat storage medium classification......32

2.4.1 Water......33

2.4.2 Molten Salts......33

2.4.3 Natural rocks......34

2.4.4 Solid Particles......35

Chapter 3 Magaldi Green Energy TES......38

3.1 MGTES......40

3.1.1 Overview and Components......40

3.1.2 Operation......42

3.2 STEM®......43

3.2.1 Overview and components......44

3.2.2 Operation......47

Chapter 4 Heliostat Control applied to STEM......49

4.1 MHC - Hardware and Algorithms......49

4.1.1 Functionalities......50

4.1.2 Astronomical and Kinematic Model 51
4.1.3 Heliostat calibration and integral error correction system....52
4.2 Experimental Test Results....54

Chapter 5 MGTES Charging System Characterization....57
5.1 Heating Modes....57
5.1.1 Convective Heating (CH)....58
5.1.2 Radiative Heating (RH)....59
5.1.3 Conduction Heating....60
5.2 Assumptions....60
5.3 Analytical evaluation....63
5.3.1 Imm-H Configuration....64
5.3.2 Flui-H Configuration....66
5.3.3 Ceil-H....67
5.4 Experimental Tests....70
5.4.1 Scaling up strategy....76
5.5 Heating Technologies Assessment....78

Conclusions....83
Key results on STEM® 83
Key results on MGTES 84

Bibliography....87

Appendix A Magaldi Heliostat Control....94

Appendix B Analytical Evaluation Code 99

Appendix C Ceil-heaters Experimental test....102

Appendix D Introducing to Optimization Model for a microgrid with integrated TES....104

List of Figures

Figure 1 Global energy-related and industrial process CO_2 emissions by scenario [2]
Figure 2 Global CO_2 Emission by sector, 2019-2022 [4]
Figure 3 CO_2 emissions reductions by mitigation measures in the NZE Scenario [7]
Figure 4 Total installed capacity and electricity generation by source in NZE Scenario
Figure 5 Changes in total energy supply by source in NZE Scenario [7]
Figure 6 Investments in grids and storage by region [14]
Figure 7 Global annual investment in solar PV and other generation technologies
Figure 8 Energy shifting
Figure 9 Global greenhouse gas emissions by sector and industrial segment [13]
Figure 10 Industrial temperature requirements, Germany [13]
Figure 11 Classification of chemical and thermochemical storage (left) Chemical storage and sorption storage classification (right) [31]
Figure 12 Thermochemical energy storage cycle: charging, storing and discharging [31]
Figure 13 Heat transfer fluid CSP application [38]
Figure 14 Scheme of a CSP plant using Molten Salts as TES [44]
Figure 15 Solar tower power plant with a packed-bed storage system
Figure 16 Free-falling solid particle receiver with an air curtain [60]
Figure 17 Staggered array of Λ–shape structures [62], Metallic porous blocks [63]
Figure 18 Schematic of a rotary kiln receiver [65]
Figure 19 Schematic of a laboratory-scale up-flow fluidized particle-in-tube receiver [69]
Figure 20 Fluidized sand bed in fluidization process
Figure 21 TES based on fluidized bed and auxiliaries' equipment
Figure 22 MGTES in Power-to-Heat configuration
Figure 23 MGTES Prototype, Magaldi Power S.p.A.'s production facility in Buccino (SA), Italy
Figure 24 Typical daily operation of an MGTES Module
Figure 25 STEM® concept: CS System with heliostats, beam down, and receiver with fluidized bed
Figure 26 Concept diagram of integrated receiver and its auxiliaries
Figure 27 Automation and control system of a STEM® module
Figure 28 STEM® 2 MW industrial-scale plant in San Filippo del Mela, Sicily (Italy)
Figure 29 Typical daily operation of a STEM® Module

Figure 30 MHC hardware and control connections between main components
Figure 31 Aiming trajectory calculation algorithm
Figure 32 MHC trajectory generation procedure, with integral error correction
Figure 33 2 MW industrial-scale plant in San Filippo del Mela, Sicily (Italy) [73]
Figure 34 Daily RMS pointing error trend along 5 months, showing the effect of BCS and integral error correction system
Figure 35 Main MGTES components with different modes for charging: convective, radiating, and fluidization air heating
Figure 36 Boundary layer development in convection heat transfer [93]
Figure 37 Radiation exchange: (a) at a surface and (b) between a surface and large [93]
Figure 38 Association of conduction heat transfer with diffusion of energy due to molecular
Figure 39 Conservation of energy for a steady-flow, open system
Figure 40 Imm-H heating mode simulation: Silica sand, 36 t, Power compressor ~ 10 kW
Figure 41 Flui-H heating mode simulation: Silica sand, 36 t,
Figure 42 Ceil-H Heating modes simulation: Silica Sand 36 t.
Figure 43 Small-scale test-rig, ~ 1 t
Figure 44 Pictures of the small-scale test-rig in Magaldi's Factory, Buccino (SA), Italy
Figure 45 Small-scale test-rig HMI
Figure 46 Process Test Protocol
Figure 47 Imm-H experimental tests: bed average temperature, heaters average temperature, air fluidization velocity over time
Figure 48 Imm-H experimental tests: sand bed temperatures at multiple locations over time
Figure 49 Imm-H experimental tests: heaters resistors temperatures over time
Figure 50 Imm-H heater temperature vs fluidized sand bed
Figure 51 Flowchart of the technology development of MGTES
Figure 52 Daily RMS pointing error trend along 5 months, showing the effect of BCS and integral error correction system
Figure 53 Main MGTES components with different modes for charging: convective, radiating, and fluidization air heating
Figure 54 SWOT Analysis Matrices for Imm-H and Ceil-H configuration respectively on the left and on the right
Figure 55 Human Machine Interface Magaldi Heliostat Control
Figure 56 MHC Block Diagram (Code)
Figure 57 General screen single heliostat access
Figure 58 GUI library hierarchy
Figure 59 Organization of the GUI management library

Figure 60 MHC Library Organization
Figure 61 Communication Serial Bus Topology RS485:: Daisy Chain, Master-Slaves
Figure 62 RS485 Library
Figure 63 Structure of VIs, subVIs and RS485 data type
Figure 64 Picture of an immersion heater tested in fluidized bed (A)
Figure 65 Picture of an immersion heater tested in fluidized bed (B)
Figure 66 Thermography and a picture of a radiant heater tested in fluidized bed
Figure 67 IR and visible frequency picture of Radiant Panel
Figure 68 Screen of Ceil-Heaters test
Figure 69 Screen of block diagram Ceil-Heaters test
Figure 70 Microgrid power flows through electric and thermal nodes [107].

List of Tables

Table 1 Industrial Sub-Sector Emissions and Heat Use [13]

Table 2 Long Duration Energy Storage categories [13]

Table 3 Characteristic Parameters of TES System [23][24][25]

Table 4 TES temperatures range

Table 5 Properties of some PCM [28][27]

Table 6 Thermochemical ES materials [37][31]

Table 7 Global pointing error statistics for 5 months, using different control type

Table 8 Global pointing error comparison with similar heliostat control systems in the scientific literature. Berenguel et al. value has been calculated by transforming the error from cm to mrad considering a heliostat at an average distance from the target of 100 m. Strachan and Houser pointing error has been calculated by using the Euclidean distance from the azimuth and elevation components

Table 9 1 t, small-scale test-rig hardware components

Table 10 Main data of the small-scale test-rig in Magaldi's Factory, Buccino (SA), Italy

Table 11 Qualitative assessment Imm-heaters and Ceil-Heaters configurations

Table 12 SWOT Analysis for Imm-Heaters

Table 13 SWOT Analysis for Ceil-Heaters

Table 14 Global pointing error statistics for 5 months, using different control types

Table 15 Global pointing error comparison with similar heliostat control systems in the scientific literature. Berenguel et al. value has been calculated by transforming the error from cm to mrad considering an heliostat at an average distance from the target of 100 m. Strachan and Houser pointing error has been calculated by using the Euclidean distance from the azimuth and elevation components

Table 16 Analytical and Experimental Results Comparison

Table 17 Input parameters for Analytical Simulation

Table 18 Ppv is the output power of PV plant, Tc is the PV cell temperature, Eb is the remaining capacity (charge) of batteries, Qst is the thermal energy stored in the TES, Ts (storage temperature) represents the state of charge of TES

Acronyms

ACAES *Adiabatic Compressed-air-energy storage*

APS *Announced Pledges Scenario*

CO_2 *Carbon Dioxide*

CAES *Compressed-air-energy storage*

CAPEX *CAPital EXpenditure*

CCUS *Carbon Capture, Utilization and Storage*

COP *Coefficient of Performance*

CS *Concentrating Solar*

CSP *Concentrating Solar Power*

CST *Concentrating Solar Thermal*

CSTS *Contactors as Secondary Tap Selector*

EMC *Electro-Magnetic Compatibility*

EMS *Energy Management System*

EV *Electric Vehicle*

GHG *Green-House Gases*

GME *Gestore Mercati Energetici*

Gt *Gigatons*

HMI *Human Machine Interface*

HTF *Heat Transfer Fluid*

IEA *International Energy Agency*

IRENA *International Renewable Energy Agency*

LH *Latent Heat*

LP *Linear Programming*

LDES *Long Duration Energy Storage*

MEMS *Micro Electro Mechanical System*

MENA *Middle East North Africa*

MGTES *Magaldi Green Thermal Energy Storage*

MHC *Magaldi Heliostat Control*

MILP *Mixed Integer Linear Programming*

NZE - *Net Zero Emissions*

OLTC *On-Load Tap Changers*

OPEX *OPerational EXpenditure*

P2H *Power-to-Heat*

P2P *Power-to-Power*

PLC *Programmable Logic Controller*

PV *PhotoVoltaic*

RES *Renewable Energy Storage*

SH *Sensible Heat*

STEM *Solar Thermo-Electric Magaldi*

STEPS *Stated Policies Scenario*

SWOT *Strengths Weaknesses Opportunities Threats*

TES *Thermal Energy Storage*

TSO *Transmission System Operator*

UPS *Uninterruptible Power Supply*

UNFCCC *United Nations Framework Convention on Climate Change*

ZVS *Zero Voltage Switching*

Chapter 1
Introduction

This chapter underscores the critical need for an energy transition across all sectors that currently rely on fossil fuels for electricity and thermal energy production. The reduction of fossil fuel dependence necessitates the integration of renewable energy sources (RES), which are characterized by their intermittent and non-dispatchable nature. To enable a more effective integration of RES and to address their inherent variability, energy storage systems (ESS) are essential for aligning energy supply with demand.

The chapter places a particular emphasis on the decarbonization of the industrial sector, where fossil fuels are extensively used for high-temperature heat and process energy. In this context, Thermal Energy Storage (TES) systems play a pivotal role, facilitating the generation and storage of thermal energy derived from RES. TES enables the stabilization of thermal energy supply, thereby enhancing the feasibility of integrating RES into industrial processes and reducing greenhouse gas emissions associated with fossil-based thermal energy production.

1.1 Global Warming

As outlined in the foreword of the United Nations Framework Convention on Climate Change (UNFCCC) document [1], climate change and its detrimental impacts represent a global concern for humanity. The Convention highlights that human activities have significantly raised atmospheric concentrations of greenhouse gases, thereby intensifying the natural greenhouse effect. This exacerbation is projected to lead to an additional warming of the Earth's surface and atmosphere, posing threats to natural ecosystems and human well-being. The global mean surface temperature has risen by approximately 1.2 degrees Celsius (°C) above pre-industrial levels, a change that has manifested in extreme weather events worldwide, such as heatwaves and droughts. These climatic phenomena have caused substantial harm to affected regions, reduced output from hydro and thermal power sources, and sharply increased demand for air conditioning, placing considerable pressure on energy systems.

In [2], several scenarios are presented to assess the current global energy landscape and its future trajectory. The Stated Policies Scenario (STEPS) provides a forecast based on existing policy frameworks, encompassing energy, climate, and industrial regulations. The Announced Pledges Scenario (APS) assumes that all national energy and climate targets publicly committed by governments will be fully realized and on schedule. Lastly, the Net Zero Emissions by 2050 Scenario (NZE Scenario) is a normative pathway for the energy sector to achieve net-zero CO_2 emissions by 2050, aiming to limit global warming to 1.5°C [2].

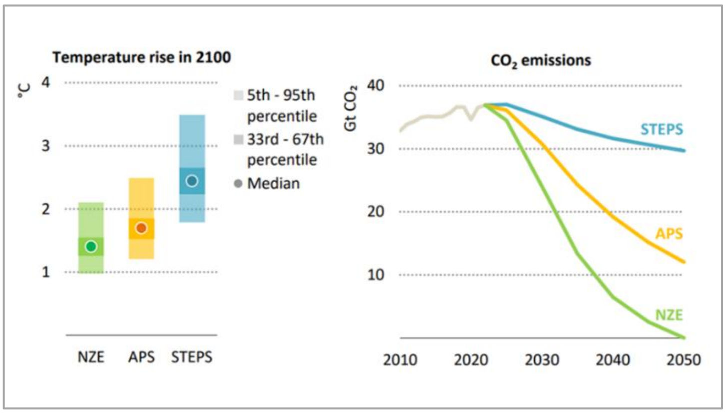

Figure 1 Global energy-related and industrial process CO_2 emissions by scenario [2]

In the Stated Policies Scenario, the global average surface temperature rises to 1.9°C above pre-industrial levels by 2050 and is projected to rise to 2.4°C by 2100 and higher. Due to uncertainties in the Earth's response to future emissions, there is a 1 in 3 chance that the temperature increase in 2100 will exceed 2.6°C in the STEPS, and a 1 in 20 chance that the temperature increase will exceed 3.5°C in the STEPS. In the Announced Pledges Scenario, the temperature rise is slower, especially after 2030, reaching about 1.7°C in 2100. In the Net Zero Emissions by 2050 scenario, the temperature rise peaks at just under 1.6°C around 2040, before falling back to around 1.4°C in 2100. All further temperature rises carry risks: those in the STEPS would risk particularly extreme consequences for global ecosystems and human well-being. Global energy-related CO_2 emissions rise to an historic high of 37 gigatons of carbon dioxide (Gt CO_2) in 2022. In the STEPS, emissions remain mostly flat until the late 2020s. They then slowly decline to 30 Gt CO_2 in 2050. Emissions fall by just over 2% per year to 31 Gt CO_2 in 2030 and then further to 12 Gt CO_2 in 2050 in the APS. In the NZE scenario, emissions decrease by over 5% per year to 24 Gt CO2 in 2030 and then reach zero in 2050. The NZE scenario also assumes rapid reductions in CO_2 emissions from land use, reaching net zero immediately after 2030, and in emissions of all non-CO_2 greenhouse gases.

The number of countries that have committed to achieving net zero emissions by mid-century or soon after continues to grow, but so do global greenhouse gas emissions. This gap between rhetoric and action must be bridged if we are to have a chance of achieving zero emissions by 2050. To do so requires a complete transformation of the energy systems that underpin our economies [3]. As can be seen from Figure 2, the sectors causing the most CO_2 emissions are the power generation 'power' sector and industry.

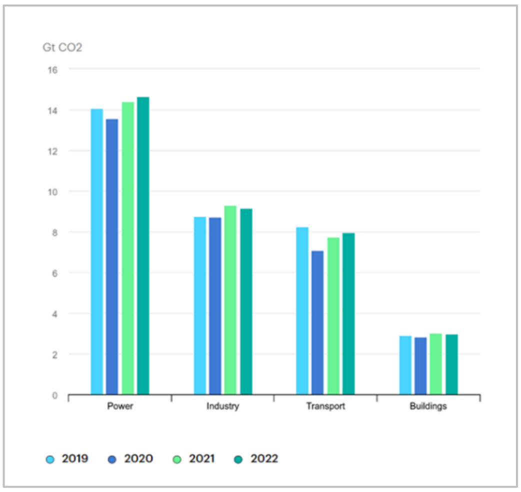

Figure 2 Global CO_2 Emission by sector, 2019-2022 [4]

CO_2 emissions from the energy sector remain alarmingly high, reaching a new record of ~15 gigatons (Gt) in 2022. Instead of beginning to decline as predicted in the 2021 NZE report, demand for fossil fuels has increased, driven by the 2022 energy crisis after Russia's invasion of Ukraine, and so has investment in supply. Progress in energy access has stalled and millions of people still lack access to electricity, particularly in the sub-Saharan regions of Africa.

The NZE sets out a concrete roadmap for the energy sector to limit global warming. In the political arena, the awareness that we must act in unison to achieve these goals has led to the establishment of important agreements and collaborations between states such as the United Nations Framework Convention on Climate Change (UNFCCC) secretariat [5]. The Convention has an almost universal membership (198 Parties); the ultimate objective of the Convention and any related legal instruments that the Conference of the Parties may adopt is to achieve stabilization of greenhouse gas concentrations in the atmosphere at a level that would prevent dangerous anthropogenic interference with the climate system. Such a level should be achieved within a time frame sufficient to allow ecosystems to adapt naturally to climate change, to ensure that food production is not threatened and to enable economic development to proceed in a sustainable manner. This concept is summarized by the well-known main objective of keeping the global average temperature increase in this century as close as possible to 1.5°C compared to pre-industrial levels.

1.2 CO_2 emissions reductions pathway

Human activities, principally through emissions of greenhouse gases, have unequivocally caused global warming, with global surface temperature reaching 1.1°C above 1850-1900 in 2011-2020. Global greenhouse gas emissions have continued to increase, with unequal historical and ongoing contributions arising from unsustainable energy use, land use and land-use change, lifestyles and patterns of consumption and production across regions, between and within countries, and among individuals [6].

1.2.1 CO_2 emissions mitigation

For the above reasons, an immediate and profound change is needed, which implies the reduction of CO_2 emissions. The NZE Scenario indicates the path to be taken to achieve zero emissions by 2050. Achieving net zero emissions in the energy sector by 2050 will require the use of all available measures to reduce emissions, as depicted in Figure 3. In the short term, almost all emission reductions will come from technologies and measures that are available, scalable and cost-effective today. The most important of these is the rapid deployment of renewable energy, particularly solar PV and wind, which together account for 4 Gt CO_2 of emissions reductions by 2030. This is equivalent to the total emissions of the European Union, Japan and Korea combined today. The next major driver of emissions reductions is electrification [7]. As the electricity sector becomes increasingly decarbonized, it delivers emissions reductions through the increased use of technologies such as electric vehicles (EVs) and heat pumps in buildings and light industry. In the NZE scenario, electrification both saves energy demand and reduces emissions by around 3Gt by 2030. In the NZE scenario, electrification provides both significant savings in energy demand and reduces emissions by about 3 Gt by 2030. Measures such as more efficient end-use of emission-intensive materials and reduced material intensity of production also contribute to emissions reductions in the short term, as do changes in consumer behavior such as reducing indoor temperatures and driving speeds on highways. This diverse portfolio of measures reduces emissions by more than 2Gt in 2030 [7]. Without such measures to reduce wasteful material and energy use, the transition would be much more difficult. Fuel switching also contributes to emissions reductions by 2030 in the NZE scenario. This includes switching from fossil fuels to additional renewable options such as bioenergy, hydropower, solar thermal and geothermal, as well as increasing the use of nuclear power technology and switching from coal to natural gas. Together, these measures provide more than 3Gt of emission reductions by 2030. Improvements in the energy efficiency of appliances, equipment, trucks, aircraft and building envelopes further reduce emissions by just under 2 Gt. Hydrogen and Carbon Capture, Utilization and Storage (CCUS) take time to scale up even in the NZE scenario, but together they deliver a further 1Gt of reductions by 2030.

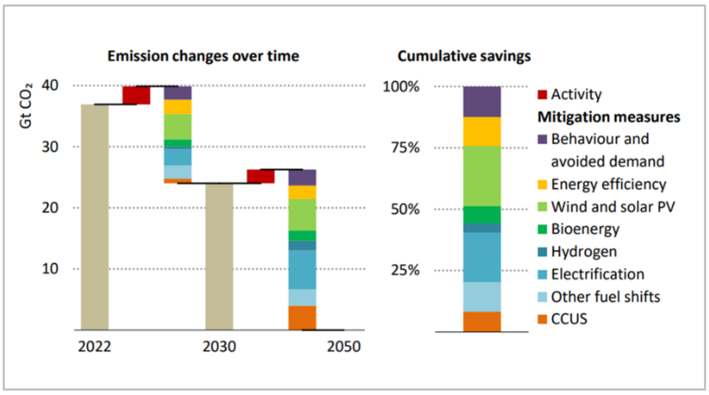

Figure 3 CO_2 emissions reductions by mitigation measures in the NZE Scenario [7]

The outlook changes in the period to 2050. Active measures in emission-intensive sectors such as steel, cement and long-distance transport are needed to achieve net-zero emissions. In the 2030-2050 period, CCUS, hydrogen and hydrogen-based fuels together account for a fifth of the emissions reductions. The contribution of electrified transport is growing, with electric vehicles now dominating the car, motorcycle and trucks, and with further electrification of buildings and industry. As a result, electrification contributes almost a quarter of the emissions reductions between 2030 and 2050. In 2022-2050, photovoltaics and wind power are the main contributors to the energy sector's emissions reductions (roughly 25%). A further 25% comes from measures to reduce demand through energy efficiency, more efficient use of materials and behavioral changes. As electricity generation is progressively decarbonized, increased electrification in the transport, industry and buildings sectors delivers 20% of the abatement. Expansion of bioenergy and other fuel switching accounts for just under 20%, and hydrogen and CCUS for just under 15%.

1.2.2 RES penetration

As per Figure 3, Solar PV and wind are the main drivers for reducing emissions from the power sector, with their combined share in global electricity generation rising from 12% in 2022 to 40% in 2030 and 70% in 2050. As depicted in Figure 4, the addition of solar PV increases by almost a factor of four to 820 GW by 2030, a quarter of which is dedicated to the production of hydrogen. Wind power additions reach 320 GW by 2030, with more than 30% of this coming from offshore and just over 10% of all wind power being dedicated to the production of hydrogen. Photovoltaics becomes the largest in 2030 and remains so until 2050, while wind becomes the second largest.

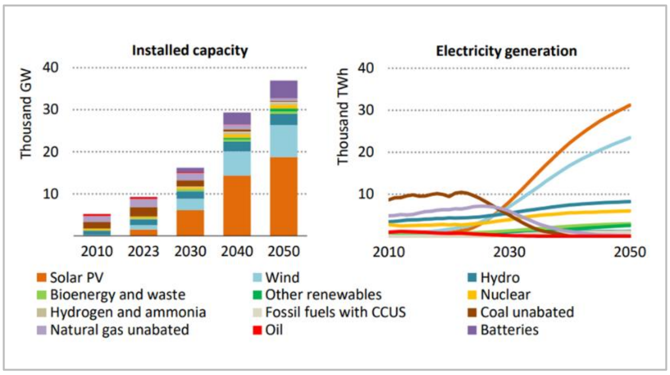

Figure 4 Total installed capacity and electricity generation by source in NZE Scenario [7]

In terms of energy consumption forecast, the same situation can be found: there is a strong increase in wind and solar PV, although the contribution to primary energy is not the best indicator of their role in the energy system, as they have lower conversion losses. Total fossil fuel demand falls by just over a quarter, or 140 EJ, by 2030. Coal falls the most, by just under 75 EJ, reflecting the higher maturity of emission reduction technologies in power generation, where most coal is used today. Oil demand falls by about 39 EJ. Natural gas declines the least, by about 26 EJ, partly reflecting its increasing use in combination with CCUS to produce hydrogen.

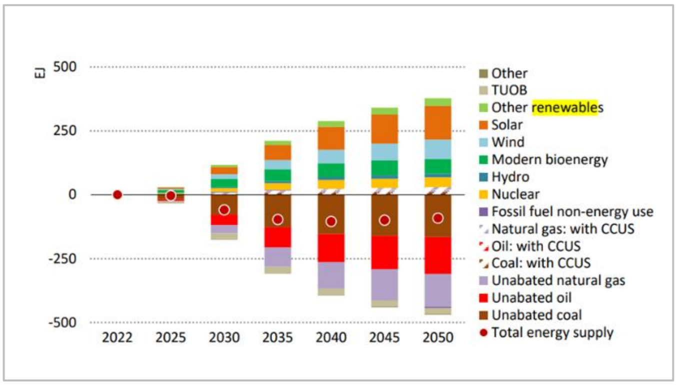

Figure 5 Changes in total energy supply by source in NZE Scenario [7]

The increase in fossil fuel use associated with CCUS is much smaller than the decrease in unabated fossil fuel use. Unabated fossil fuel demand falls by about 150 EJ by 2030, while fossil fuel use combined with CCUS rises by about 7.5 EJ by 2030, despite the strong push for CCUS in the NZE scenario. Total energy supply is almost 10% or 60EJ lower in 2030 than in 2022, even with global economic growth of more than a quarter. This implies dramatic progress in reducing energy intensity from around 2% per year today to over 4% by 2030. Improvements in the technical efficiency of appliances, motors and building envelopes are key, but a significant part of this acceleration in intensity improvement is due to a shift to more efficient energy sources such as electricity. Behavioral changes also contribute to reducing energy demand. After 2030, the energy supply pattern continues to evolve rapidly and is transformed by 2050. Solar energy, including solar thermal and solar PV, provides almost 140 EJ in 2050, almost equivalent to the total energy supply of natural gas today. Modern bioenergy provides about 100 EJ and wind about 85 EJ. In total, renewables provide almost three-quarters of the total energy supply in 2050. Retired fossil fuels with CCUS account for a further 5%. From around three-quarters of total energy supply in 2022, the use of fossil fuels, excluding those used for non-energy purposes, will fall to around 5% in 2050. Their emissions are offset by carbon capture technologies. Overall, including non-energy uses, fossil fuels contribute less than a fifth of total energy supply in 2050, reversing their current share of about four-fifths of total energy supply, including non-energy uses.

The increasing penetration of solar PV and wind in the NZE scenario requires more flexibility and stability in the power system. Due to new demand patterns and the variable output of solar PV and wind, hourly flexibility requirements quadruple between today and 2050. Seasonal variability will also increase in many regions in the NZE scenario, requiring hydropower, low-emission thermal power plants and new forms of long-term storage, including hydrogen. In addition, the high share of inverter-based resources, such as wind, solar PV and batteries, increases system stability challenges.

Batteries are well suited to provide flexibility to the electricity system on the scale of seconds, minutes or hours, and can enhance the stability and reliability of the electricity grid by providing a fast frequency response. Global utility-scale battery capacity reaches 1,000 GW in the NCE, representing around 15% of all dispatchable power. Hydropower is already a major source of storage, but others, including thermal and gravity storage, have also emerged.

1.2.3 TES for driving the RES penetration

Ever-growing decarbonization commitments are transforming the world’s energy system at an unprecedented rate. In 2020, 127 GW of solar and 111 GW of wind power were installed worldwide [8]. However, the volatility nature of renewables such as wind and solar means that they are not dispatchable, and solutions are needed to support greater penetration of renewables, a key one being energy storage.

Several solutions are currently available for grid-scale electricity storage. At present, 127 GW and about 9000 GWh of pumped hydro are installed worldwide [9], making up 95% of the overall global storage capacity, but further deployment is bound to favourable geographical locations. Compressed air energy storage (CAES) is an option that stores energy as compressed air in underground caverns. When thermal storage is added to the system, it is called adiabatic CAES or ACAES, yielding an increased efficiency of up to 70% [10]. There are currently two commercial CAES plants in operation (290 MW and 110 MW, respectively), plus a number of adiabatic demonstration facilities, but this technology is also constrained by geology. On a smaller scale, supercapacitors, flywheels, and batteries are deployed [11]. These storage solutions are best suited to short charge/discharge periods due to their higher cost per unit capacity [12] and the existing link between power and energy storage capacity. However, there are promising set of technologies with low specific cost and not suffering from capacity-power coupling or geographical constraints, known as Long Duration Energy Storage (LDES).

Multiple long-duration energy storage technologies are currently available on the market and under development. These technologies can provide more than eight hours of energy using a variety of electrochemical, mechanical, thermal, and chemical storage media. It is clear that many of these technologies have been under development for over a decade and frequently employ existing motors, pumps and other equipment already utilized in other industries. The importance of long duration energy storage technologies will undoubtedly increase in line with an increasing saturation of intermittent renewable energy supplies on electric grids across the globe [13]. LDES technologies paired with renewables could reduce global industrial greenhouse gas emissions by 65%. The above is stated by the LDES Council, a global non-profit organization with a clear mission: to decarbonize global energy systems by 2040. The Council is committed to developing, deploying and integrating LDES to achieve this goal. The LDES Council is committed to facilitating the transition to a more sustainable and resilient energy future. To achieve this, the Council is encouraging policies, fostering innovation, and promoting collaboration among our members and stakeholders in the energy industry. The LDES Council is the leading voice in advocating for the widespread adoption of diverse long-duration energy storage technologies. It provides guidance and reports to enable the integration of renewable energy sources and enhance grid stability using LDES technologies. The goal is to achieve a flexible, secure, reliable, affordable, and fossil fuel-free energy system. It is clear that there is a need to reinforce the network and storage systems. This trend is already underway indeed it is evidenced by the significant investments (Figure 6) made in the electricity grid and storage systems in recent years.

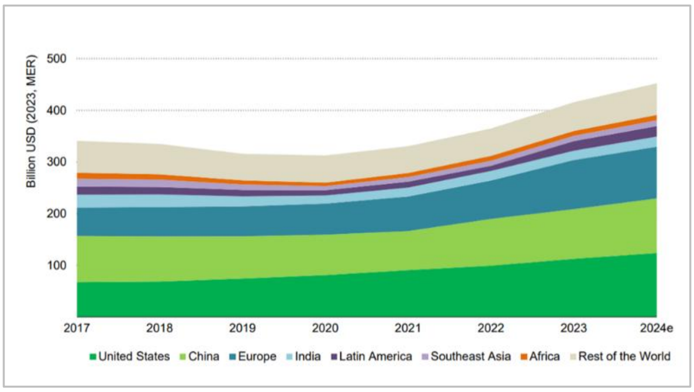

Figure 6 Investments in grids and storage by region [14]

Following a sharp decline triggered by the global pandemic, the investment landscape showed a strong rebound starting in 2020, with momentum building throughout 2021. By the end of 2022 and continuing into 2023, investments surged to unprecedented levels, reflecting renewed confidence across various sectors. This resurgence was fueled by several factors, including government stimulus packages, low interest rates, and the accelerated digital transformation of industries. As a result, overall investment activity witnessed an impressive growth of approximately 30%, marking a robust recovery and surpassing pre-pandemic levels. This upward trend highlights the resilience of markets and their capacity to adapt to rapidly changing conditions [8].

The remarkable surge in investments in storage systems is undeniably linked to the explosive growth of solar photovoltaic (PV) energy. As depicted by Figure 8, projections indicate that by 2024, investments in solar PV technology within the power sector will exceed an astounding 500 billion US dollars, outpacing the combined total investment in all other power generation sources. This represents a staggering 100% increase compared to 2021 [16]. While a potential deceleration in growth is expected in 2024 due to decreasing PV module prices, solar energy remains a cornerstone in the ongoing transformation of the global power sector.

In fact, in 2023, each dollar invested in wind and solar PV generated 2.5 times more energy than the same investment did just a decade earlier, highlighting the dramatic efficiency improvements in renewable technologies. The shift in investment focus is even more striking when comparing clean energy to fossil fuels: in 2015, the investment ratio of clean power to unabated fossil fuel power was about 2:1. By 2024, this ratio is projected to leap to 10:1, emphasizing the increasing dominance of renewable energy sources in global energy portfolios.

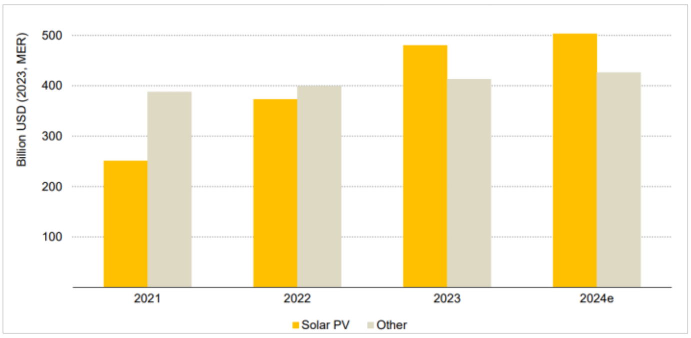

Figure 7 Global annual investment in solar PV and other generation technologies [14]

The rapid expansion of solar and wind energy has also had a notable impact on energy markets. In some countries, the influx of renewable power has contributed to a drop in wholesale electricity prices, with prices even turning negative during periods of high wind and solar generation. While this benefits consumers, it presents new challenges for producers, particularly in terms of earnings on the spot market. These challenges further underscore the critical need for complementary investments in energy storage and system flexibility to stabilize supply and maximize the value of renewable energy resources, ensuring a smooth transition to a low-carbon energy future [17].

The Figure 8 illustrates the concept of energy shifting in solar power generation, particularly highlighting the role of energy storage in addressing the mismatch between solar energy production and electricity demand. Solar energy generation peaks during midday, typically when the demand for electricity is lower. In contrast, demand surges in the early morning and evening, which do not coincide with the periods of maximum solar energy availability.

Energy storage systems play a crucial role by storing excess energy generated during peak solar hours and then releasing it during times of higher demand, such as morning and evening peaks. This process, referred to as energy shifting, enables a more balanced and efficient use of solar power, ensuring that energy supply meets demand even when the sun is not shining. As a result, storage solutions are essential in optimizing solar energy use, reducing reliance on traditional power sources, and enhancing grid stability [18].

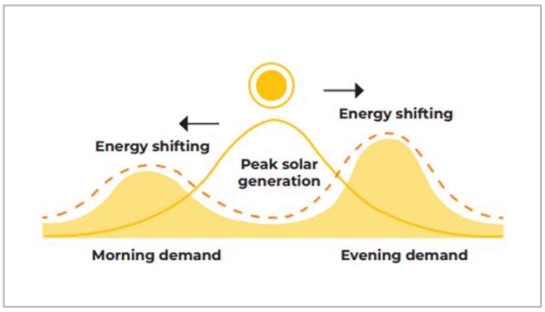

Figure 8 Energy shifting [22]

Indeed, as depicted by the Figure 8, the peak of solar generation occurs in the middle of the day, instead the maximum energy demand happens at the morning and at the evening. Using energy storage, it is possible to have a time shift of the energy, synchronizing demand and generation energy [22].

Summarizing, as RES penetration increases, the TES becomes a vital technology to manage the variability of renewable energy, particularly for large-scale applications. TES is the process of storing energy in the form of heat or cold, which can then be used later to produce electricity or provide heating/cooling.

1.3 TES for Industrial decarbonization

The industrial sector plays a crucial role in driving the global economy, but it also represents a significant contributor to environmental degradation. Industrial activities are responsible for approximately one-third of the world’s annual greenhouse gas emissions [13]. In 2020, these emissions reached an estimated 10 billion tons of CO_2 equivalent, and, without targeted interventions, this figure is projected to nearly double by 2050. A significant portion of this increase is expected to originate from developing economies.

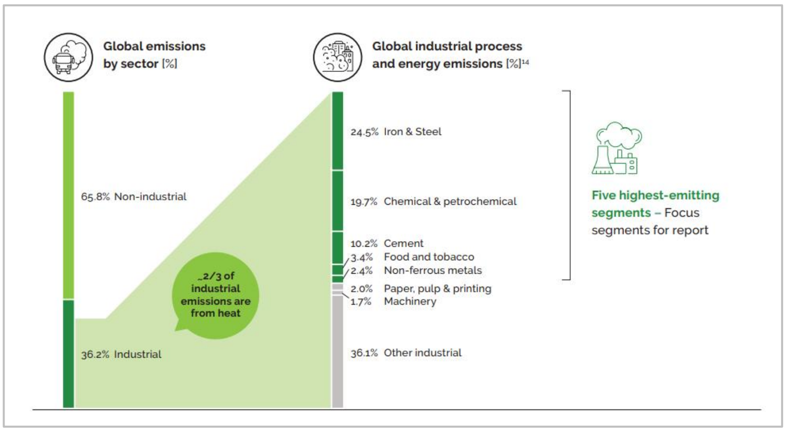

Figure 9 Global greenhouse gas emissions by sector and industrial segment [13]

Approximately half of all industrial greenhouse gas emissions are attributable to the heat requirements of production processes. These emissions remain substantial because the vast majority of industrial heat is currently generated by the combustion of fossil fuels. Industrial processes demand significant quantities of heat, often at precise temperature levels (in Table 1 some examples). This dependency on fossil fuel-based heat not only contributes to high emissions but also challenges the transition to sustainable energy sources.

Projections indicate that the demand for industrial heat will increase by 34% between 2019 and 2040, with the most significant growth occurring in the low- and medium-temperature heat segments [19]. This surge in demand is closely linked to economic and population growth, as well as a global push towards achieving energy independence. As industrial heat consumption rises, there is an urgent need for innovative solutions, such as the integration of renewable energy sources and advanced energy storage systems, to mitigate emissions and ensure a sustainable transition. Without these interventions, the current trajectory threatens to undermine global efforts to reduce emissions and achieve long-term climate goals.

Industry Sub-Sector	Reported CO_2 Emissions [MMTC0_2E/YR]	Industry Process-Heat Type/Purpose	Process Heat Temp (°C)	Average Plant Heat Use [TJ/DAY]*
Petroleum Refineries: Gasoline, Diesel, Kerosene	1.24	Combustion gases/ atmospheric crude fractionator and heavy naphtha reformer	600	8.23
Iron and Steel Mills	51	Combustion gases/coke production	1100	2.42
		Combustion gases/steel production	1700	
		Electricity/steel production	2200	
Paper Mills	32	Steam/stock preparation	150	21.1
		Steam/drying	177	

Paperboard Mills	24	Steam/stock preparation	150	21.1
		Steam/dry ing	177	
Pulp Mills	12	Combustion gases/ electricity production	800	0.67
		Steam/wood digesting, bleaching, evaporation, chemical preparation	200	1.15
		Steam/evaporation, chemical preparation	150	1.15
All Other Basic Chemical Manufacturing	21	Combustion gases/ primary reformer; steam/ methanol distillation	900	12.9
Ethyl Alcohol Manufacturing	18	Combustion gases for steam/ byproduct drying (corn dry mills)/pretreatment and conditioning (lignocellulosic processes)	266	1.76
		Steam/distillation	2.33	
		Steam/electricity production	454	
Plastics Material and Resin Manufacturing	17	Steam/distillation	291	10.6
Petrochemical Manufacturing	16	Combustion gases/ cracking furnace	875	2.37

Table 1 Industrial Sub-Sector Emissions and Heat Use [13]

Decarbonizing the industrial sector necessitates a comprehensive shift from current technologies reliant on fossil fuels to electrification strategies that can integrate and optimize the use of renewable energy sources and storage system to satisfy varying heat demands across different temperature ranges. Electrifying industry, however, presents a substantial challenge, as industrial processes require a wide spectrum of temperatures, from low to high, to meet the diverse needs of manufacturing sectors as shown by Figure 10.

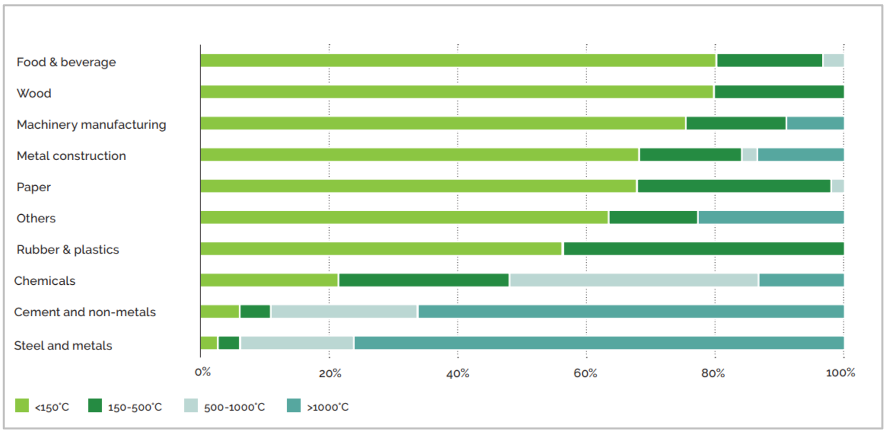

Figure 10 Industrial temperature requirements, Germany [13]

The chart highlights the complexity of decarbonizing the industrial sector, as each industry has distinct heat requirements. Sectors relying on high-temperature heat present significant challenges for electrification, while industries with lower heat demands may more readily transition to renewable solutions. This visualization underscores the need for tailored approaches in achieving industrial decarbonization across diverse sectors.
The industries presented in the bar chart can be categorized into two distinct groups based on their heat demand: the first group, requiring temperatures below 500°C, and the second, operating between 500°C and 1000°C. The first group, which includes sectors such as food and beverage, wood, and paper, appears more conducive to electrification, as lower temperatures can be efficiently supplied by existing technologies which are already mature and can be implemented to decarbonize these sectors with relatively fewer barriers. Conversely, the second group, comprising industries such as cement, steel, and chemical production, requires significantly higher temperatures, making the electrification process more complex. High-temperature processes above 500°C are less compatible with technologies, and the development of more advanced solutions—such as high-temperature heat pumps, electric arc furnaces, or thermal storage systems—is essential for decarbonizing these industries. Given the substantial energy needs and technical challenges associated with achieving these temperatures, electrifying this second group poses a greater challenge, and will likely require more time, innovation, and investment in research and development [21].
In light of the intermittent nature of renewable energy sources and the necessity for heat on demand, which in some cases must be provided continuously on a 24/7 basis, the implementation of a long-duration energy storage (LDES) system is imperative to guarantee the uninterrupted provision of services. The table below illustrates the classification of LDES systems into distinct categories.

	Electrochemical	Thermal	Chemical	Mechanical
Description	Energy storage systems generating electrical energy from chemical reactions	Solutions stocking thermal energy by heating or cooling a storage medium	Chemical energy storage systems store electricity through the creation of chemical bonds	Solutions that store energy as a kinetic, gravitational potential or compression/pressure medium
Types	- Flow - Metal anode - Non-Metal Chemical Storage	- Sensible heat - Latent heat - Thermochemical	- Green hydrogen - Methane - Ammonia - Methanol	- Compressed air energy storage - Liquid air energy storage - Pumped hydro storage - Gravity based storage - Liquid CO_2
Advantages	- Flexibility - Declining long-term costs - Wide operating range	- No degradation - Cycling throughout the day - Modular options available	- Potential range of footprint and RTE with relative higher C-rates - Technology options either have inexpensive materials or require less expensive materials than LiB	- No degradation - Proven via established technologies (pumped hydro) - Considered safe - Attractive economics

Table 2 Long Duration Energy Storage categories [13]

This introductory paragraph, which highlights the reasons why the introduction of TESs is important in the world energy scenario and especially for the industrial sector, is followed by the state of the art of TESs, a paragraph presenting Magaldi Green Energy technologies, and finally the paragraphs explaining the innovative control algorithms for the STEM® system and the characterisation of the charging system of the MGTES system, with conclusions.

Chapter 2

State of art of TES

This chapter presents a comprehensive overview of TES systems, categorizing them based on various technologies, heat storage media (HSM), and operational temperature ranges. It delves into the fundamental characteristics of each type, highlighting their advantages, limitations, and potential applications across different sectors. Special attention is given to TES systems that employ solid particle-based HSM, with an in-depth analysis of their thermal performance, energy density, and suitability for high-temperature applications. This study provides valuable insights into the emerging role of solid particle-based TES technologies in advancing energy storage solutions

2.1 Overview of TES

TES systems accumulate energy in the form of heat inside a HSM, enclosed in one or more insulated containers to minimize energy losses towards the outside; TES systems are equipped with heat exchangers for thermal energy transfer, to charge or discharge the storage. There are a variety of technologies for storing thermal energy as sensible heat (SH), latent heat (LH), or thermochemical energy (TC). Sensible heat storage systems involve a temperature increase or decrease as a result of heat transfer; conversely, in latent heat storage systems the heat absorption and release take place during the phase change of the storage material, at constant temperature. Thermal chemical storage systems are based on the absorption and release of energy in reversible chemical reactions [23], following a more detailed explanation about these three typologies focusing on the sensible heat storage main topic of this thesis. The typical characteristics of TES systems are:

- **Capacity**: The capacity of a TES system refers to the amount of thermal energy it can store. It is typically measured in joules (J), kilowatt-hours (kWh). This parameter can be expressed per unit of mass too (kWh/t).
- **Power**: The power of a TES system indicates the rate at which the system can store or release thermal energy. It is measured in watts (W) or its multiples (kW, MW, etc.)
- **Efficiency**: The efficiency of a TES system measures the amount of stored energy that can be effectively recovered and utilized. It is expressed as a percentage (%).
- **Storage Period**: The storage period refers to how long (hour, day, weeks, months) thermal energy can be stored before significant losses occur or before it is used.
- **Costs**: TES system costs include both capital expenditure (CAPEX), related to the purchase and installation of the system, and operational expenditure (OPEX), associated with operation and

- maintenance.

TES system	Capacity [kWh/t]	Power [MW]	Efficiency [%]	Storage Period [h, d, w, m]	Cost [€/kWh]
SH-TES	10÷50	10^{-3}÷50	50÷94	day/months	0.1÷30
LH-TES	50÷150	10^{-3}÷10	75÷90	hour/weeks	0.4÷70
TC	120÷250	10^{-2}÷5	75÷90	day/months	10÷130

Table 3 Characteristic Parameters of TES System [23][24][25]

Additionally, the TES can be grouped respect to the operating range temperature:

Category	Temperature Range
Cold TES systems	T < 20 °C
Low-Temperature TES systems	20 °C <T < 100 °C
Mid-Temperature TES system	100 °C < T < 250 °C
High/very-high Temperature	T > 250 °C

Table 4 TES temperatures range

2.2 Latent Heat Storage

Latent heat TES (LHTES) relies on the storage material absorbing or releasing heat as it undergoes a solid to solid, solid to liquid or liquid to gas phase change or vice versa. The storage capacity of a LHS system with a PCM [26] is given by:

$$Q = \int_{T_i}^{T_m} mC_p dT + ma_m \Delta H_m + \int_{T_m}^{T_f} mC_p dT \quad (2.1)$$

where a_m is the fraction melted, ΔH_m is the heat of melting per unit mass (J/kg). LHS offers a high storage density with a narrower temperature range between storing and releasing heat [27].

LHTES systems operate on the principle of storing and releasing thermal energy through the phase change of a storage material, known as a Phase Change Material (PCM). One of the key advantages of LHTES is its ability to achieve high energy storage density while maintaining a near-constant temperature during the phase transition, which is beneficial for many thermal applications. PCMs are available across a wide range of temperatures, making them adaptable for various use cases. For large-scale, low-temperature storage applications, materials like water (used in ice storage systems) and aqueous salt solutions (for sub-zero temperatures) are already commercially available.

PCMs can be broadly categorized into three main groups: inorganic compounds, organic compounds, and eutectics, which are mixtures of inorganic and organic materials. Table 5 provides a summary of the properties of various PCMs [28]. Among these, paraffin-based PCMs, which belong to the alkane family of hydrocarbons, have been extensively researched due to their high latent heat of fusion, chemical stability, low vapor pressure, resistance to phase segregation, and relatively low cost. One of the primary objectives in the development of LHTES systems is to improve the efficiency of the PCM charging and discharging processes. Ongoing research is focusing on enhancing the heat transfer properties within these systems.

PCM	Melting [°C]	Latent heat [kJ/kg]
Paraffin C14	5.5	228
Paraffin C21-C30	66-68	189
Non paraffin Formic acid	7.8	247
Non paraffin Capric acid	32	152.7
Non paraffin Stearic acid	69.4	199
Benzamide	127.2	169.4
Salt hydrateNaC03-10H2O	32	246.5
Salt hydrateMgC12 6H20	117	168.6
Metal Gallium	30	80.3
Salt LiN03	253	373
Salt NaN03	307	172
Salt KN03	336	116
Salt Li2C03	732	509
Eutectic o/o (34-66%wt)	24	147.7

Table 5 Properties of some PCM [28][27]

Among PCMs in Table 5, classes of materials, including hydrated salts, paraffin waxes, fatty acids, the eutectics of organic and non-organic compounds and polymers find industrial application in relation to the temperature ranges over which the TES phase transition occurs:

- low temperature PCMs: with phase transition temperatures below 15°C, usually used in air conditioning applications and the food industry.
- mid temperature PCMs, the most popular – with phase transition temperatures in the range 15–90°C with solar, medical, textile, electronic and energy-saving applications in building design.
- high temperature PCMs with a phase transition above 90°C developed mainly for industrial and aerospace applications [29].

The PCM should be readily available in large quantities at low. In practice, those criteria are not fully met by most PCMs. However, recent progress in the design and characterization of novel materials for energy storage, including nanomaterials, has opened new possibilities for enhanced performance with extended lifetimes [27].

2.3 Thermochemical storage

Chemical TES can generally be classified into two main types: chemical storage and thermochemical storage. Thermochemical storage systems are further divided into open and closed configurations. The open system primarily relies on adsorption processes, in which a desiccant material is used in conjunction with heat storage to complete the sorption cycle. In contrast, closed systems operate with a sealed working fluid, isolated from the external atmosphere, ensuring a controlled internal cycle [30].

Within closed thermochemical storage systems, two distinct processes can be identified: adsorption, where a substance adheres to the surface of a solid or liquid, and absorption, where the substance is incorporated into the bulk of the material. Figure 11 (left) provides a detailed classification of chemical and thermochemical storage systems. It is important to note that clear distinctions between terms such as chemical storage, thermochemical storage, and sorption storage are often challenging to delineate, as these processes can overlap or share similar mechanisms [31]. Figure 11 (right) presents a classification framework for chemical and sorption-based storage systems.

In chemical energy storage (ES), the stored chemical energy can be converted into other forms of energy through a chemical reaction, offering significant potential for energy transformation and storage in various applications

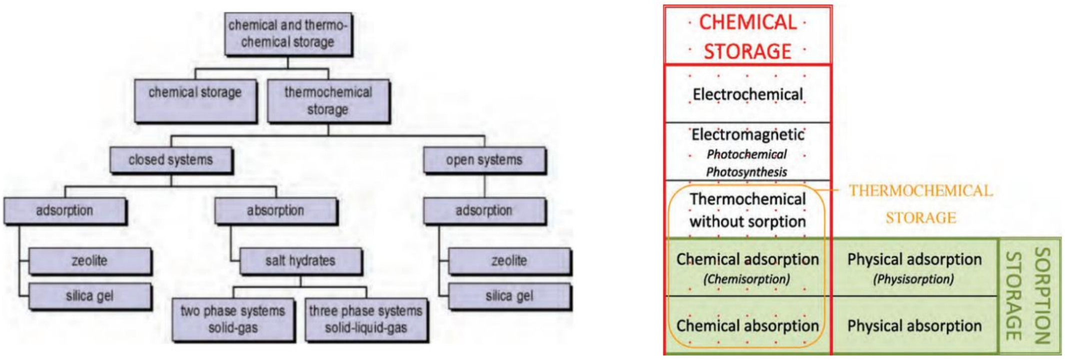

Figure 11 Classification of chemical and thermochemical storage (left) Chemical storage and sorption storage classification (right) [31]

The term sorption can be used to describe the phenomenon of the fixation or capture of a gas or vapor (sorbate) by a substance in a condensed state (solid or liquid), which is called the sorbent. Depending on the type of binding that takes place, sorption can be divided into physical sorption and chemical sorption. In general, sorption includes both absorption and adsorption. Absorption and adsorption are different phenomena, but they have in common that both involve the physical transfer of a volume of mass or energy. Specifically, absorption is related to the transfer of a volume into a volume, i.e. it is the permeation or dissolution of a volume of energy or mass (absorbate) into another volume of energy or mass (absorbent). In chemical engineering, the term adsorption is used to describe the process of separation in which certain components of a phase of a fluid are transferred to the surface of a solid adsorbent. Adsorption refers to the transfer of volume to a surface. It is an accumulation or massing of energy or matter (adsorbate) on a surface (adsorbent) [31][32][34].

Sorption and thermochemical storage systems are based on performing a reversible chemical reaction (or desorption), which allows absorption of heat in the course of the decomposition (desorption) process that is endothermic. A reverse synthesis reaction is exothermic and results in giving stored heat back. In this reversible physic-chemical reaction, C is the thermochemical material (TCM). With heat supply, C can be dissociated into components A and B, which can be any phase and stored separately. Both A and B are reactants as working pair or sorption couple, and C will be formed with a heat release when put A and B together [31][35].

A general thermochemical ES cycle includes three main processes:

- charging: the charging process is an endothermic reaction. A required energy resource is used for dissociation of compound C.
- Storing: after the charging process, A and B will be formed and both are stored in this stage and
- discharge, A and B are combined in an exothermic reaction and material C is regenerated. Meanwhile, the recovered energy is released from this phase [36].

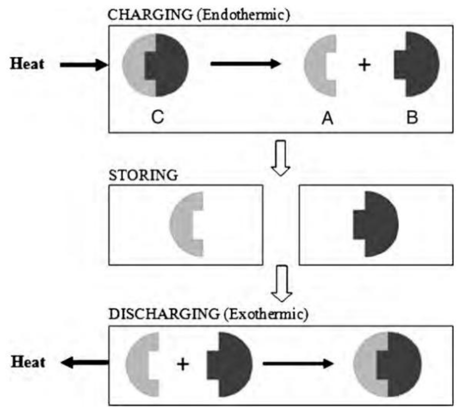

Figure 12 Thermochemical energy storage cycle: charging, storing and discharging [31]

One of the most promising applications of thermochemical storage systems, particularly in building energy management, is the sorption method. This method leverages the adsorption of water vapor onto sorbent materials such as molecular sieves and silica gel. For instance, zeolite has a heat energy density of around 200 kWh/m³, while silica gel offers approximately 230 kWh/m³. Typically, sorbent and sorbate (water or water vapor) require two separate storage tanks.

Thermochemical storage systems can be configured into two main cycles: open thermochemical and closed thermochemical. The major advantages of TCS technology are its high energy density, reaching up to 500 kWh/m³, and its potential for long-term or seasonal energy storage. Despite these benefits, several challenges remain, including material degradation during repeated charge-discharge cycles and ensuring full reversibility of the reactions. These issues necessitate further investigation to improve the reliability and longevity of TCS systems.

Nowadays, there are a number of materials and reactions that conform to thermochemical energy storage systems. Some of the promising thermochemical storage materials that have been recently identified are listed in Table 6. The table also provides the values of ES density and reaction temperature, which are two important factors for material selections [31].

Material	Density® [kg/m^3]	Energy density [MJ/m^3]
Aluminium oxide, Al2O3	3970	4320
Barium oxide, BaO	5720	4906
Borax, Na2B4O2, 10H2O	1730	1218
Calcium oxide, CaO	3300	6158
Magnesium oxide, MgO	3580	6874

Table 6 Thermochemical ES materials [37][31]

2.4 Sensible Heat - Heat storage medium classification

Sensible heat storage (SHS) stores thermal energy by raising a solid or liquid temperature. The principle is based on changing the heat capacity and temperature of the material during charging and discharging. The amount of heat stored is a function of the specific heat of the medium, the temperature change and the mass of the storage medium as describes the equation below:

$$Q = \int_{T_i}^{T_f} mC_p dT = mC_{ap}(T_f - T_i) \qquad (2.2)$$

where Q is the quantity of heat stored (J), T_i initial temperature (°C), T_f final temperature (°C), m is the mass of heat storage medium (kg), C_p the specific heat (J/kg°C), C_{ap} is the average specific heat between T_i and T_f (J/kg°C).

In this thesis work, storage of thermal energy in HSM, or in heat transfer fluid (HTF) as an SH is considered. The HTF plays a critical role in TES, indeed it is a fluid (liquid or gas) used to transport heat from one location to another within a system. In the context of TES systems, the HTF absorbs heat from a heat source (e.g., solar energy, industrial waste heat, or electrical heating elements) and transfers it to the storage medium or to the point of use.

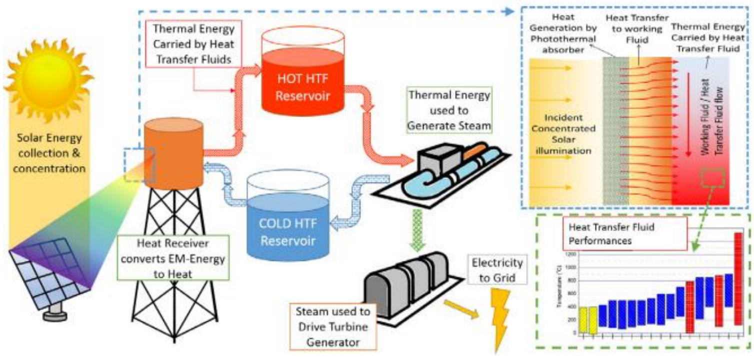

Figure 13 Heat transfer fluid CSP application [38]

In some cases, the HSM and HTF may coincide [39]. Various types of HTF and/or HSM are presented in the following, with some of their key advantages and disadvantages.

2.4.1 Water

The most commonly used HTF is water/steam, due to its low cost and high availability. Unfortunately, it's not convenient to build high-capacity steam-based TES systems, since large or high-pressure reservoirs are needed to store water at high temperatures, due to its thermo-physical properties. On the other hand, water poses no environmental problems. For this reason, water-based TES systems are only suitable for low to medium temperature residential applications [23].
In a pressurized system, the tanks store water for both low-(< 10°C) and mid-temperature storage. The costlier pressurized systems can store water up to 120-130°C, with an expansion of 30 to 40%. Storage volumes of up to 50,000 m^3 are used for large-scale applications (e.g. district heating). Water is also used for underground TES (UTES), being a relevant variant of SH-TES technology based on pumping hot or cold water underground. In this case, an aquifer TES can be involved as a tank as well as a cavern TES or a borehole TES. A real application where the water is used like HTF is [40], a 10 MW_e CSP plant with Fresnel collector situated in Llo, Cerdagne, France.

2.4.2 Molten Salts

One of the most widely used material in TES systems is Molten Salts (MS), employed as both HTF and HSM in CSP plants [41]. In CSP systems, sunlight is concentrated towards a focal point, from which the HTF transports thermal power to a steam generator as depicted in Figure 14. CSP plants can be easily coupled with TES systems, that allow to store thermal energy to be used later when solar irradiation is low, i.e. at night or during adverse weather conditions [42], making CSP plants highly dispatchable [43].

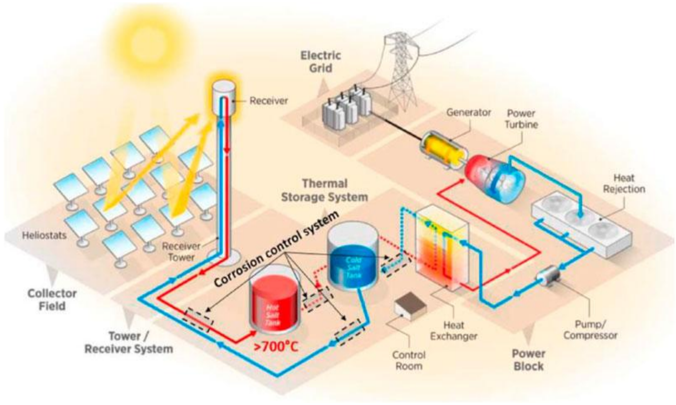

Figure 14 Scheme of a CSP plant using Molten Salts as TES [44]

MS were introduced to address the disadvantages of using diathermic oils such as thermal instability above 400°C, the need for pressure design above 300°C, flammability [45]. Molten salts have been used extensively in some CSP plants as HSM, in conjunction with diathermic oils as HTF. Afterwards, due to the above-mentioned problems with oils, MS started to be used as HTF as well, totally eliminating diathermic oils [46]. However, alloys corrosion in MS applications restricts the development of these technologies [47], in fact to mitigate this effect the operating temperatures of conventional MS plants is limited to less than 570°C and can maximally reach 800°C. Furthermore, MS must be maintained above their freezing temperature, i.e. approximately 220°C [48], and minimize the freezing risk at ambient temperature, which can be a major problem in the event of faults. Significant efforts are being made to identify new molten salts with lower melting points [49], but these drawbacks lead to consideration of other TES technologies using different materials such as natural rocks or solid particles [50].

2.4.3 Natural rocks

Natural rocks have got important characteristics such as high thermal and chemical stability in a wide temperature range, low thermal expansion coefficient, high specific heat and high melting point (greater than 900°C for the majority of rocks). For these reasons, natural rocks are suitable as HSM in TES systems [51][52].

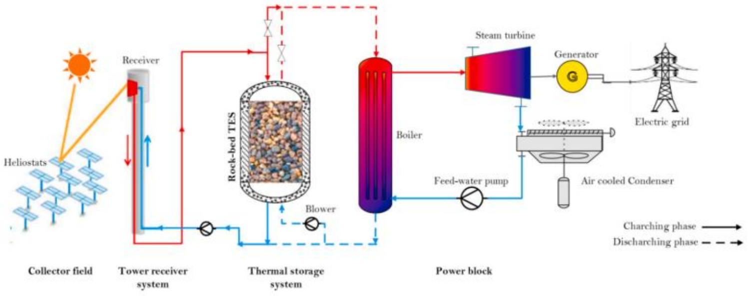

Figure 15 Solar tower power plant with a packed-bed storage system [51]

Furthermore, they are abundant and freely available in many areas, easily transportable and disposable because they are non-flammable and non-toxic [53]. Similar applications use commercial refractory ceramic as storage medium, using air as HTF [54]. These solutions involve high auxiliary consumption due to elevated HTF pressure drops [55]. Although natural rocks and ceramic have important characteristics for the TES, on the other hand they have showed some deterioration problems due to many thermal cycles. Another aspect is low thermal conductivity, which is a drawback for a thermal storage system [56].

2.4.4 Solid Particles

The deterioration problems were addressed exploring TES systems with solid particles as HSM, such as sand. However, the low thermal conductivity remains a challenge for sand-based TES system. In [57], HSM conductivity was enhanced adding discarded metallic chips to the sand bed; another solution is the use of fluidized sand beds. To date, solid particles have been widely used in the context of CSP plants with TES; in [58], many solid particles solar receiver solutions have been researched and developed. The different technologies can be categorized into three types, depending on the particle flow in the receiver: downflow, up-flow and horizontal flow [59]. In downflow receivers, the flow of solid particles is from top to bottom. Several receivers of this type have been devised. The most important are the free-falling Figure 16, chocked flow and rotating kiln receivers.

Figure 16 Free-falling solid particle receiver with an air curtain [60]

Although free-falling solar receivers have the advantage of simplicity and low operating and maintenance costs, the particles fall too rapidly to fully absorb sunlight [61]. The main characteristic of choked-flow receivers is to reduce the falling velocity of the particles, i.e. to increase the residence time of the particles in the solar radiation, leading to a greater absorption of solar energy flux. Several variants have been studied, including Λ-shaped receivers, porous receivers Figure 17, fluidized counter-flow beds.

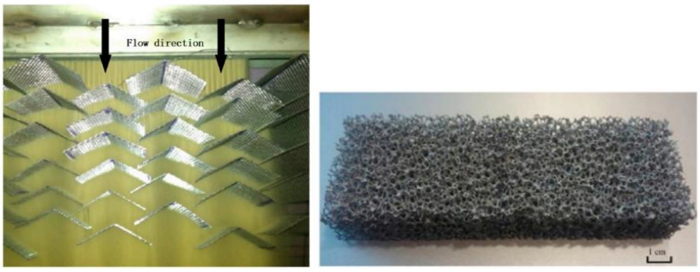

Figure 17 Staggered array of Λ–shape structures [62], Metallic porous blocks [63]

Rotary kiln receivers have a rotating cavity at the top of a tower that receives solar radiation. Due to centrifugal force, the rotating cavity increases the residence time of the solid particles in the solar radiation [64].

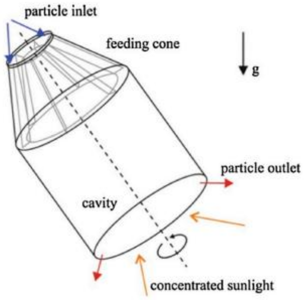

Figure 18 Schematic of a rotary kiln receiver [65]

Up-flow technology involves the flow of solid particles from bottom to top. This technology is widely used in oil refining, chemical, metallurgical and other industries. In the renewable energy sector, up-flow technology is used in spiral solar receivers, tube receivers, air receivers and fluidized bed receivers [66]. Apart from spiral solar receivers, where spirals vibrated by an electromagnet are used to move the particles from bottom to top [67], the other applications use air to move the particles. An air duct system is located at the base of the receiver and inflates air to move the solid particles upwards [68].

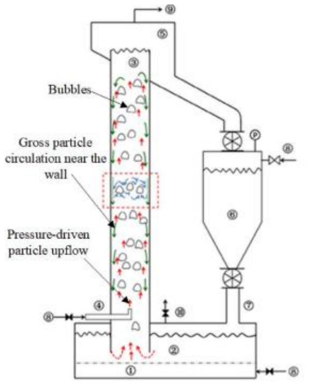

① Windbox, ② fluidized bed dispenser with ③ upflow fluidized bed, ④ secondary air injector, ⑤ disengagement chamber, ⑥ pressurized hopper, ⑦ downcomer, ⑧ compressed air, ⑨ to fines filtration, and ⑩ pressure relief valve.

Figure 19 Schematic of a laboratory-scale up-flow fluidized particle-in-tube receiver [69]

Chapter 3
Magaldi Green Energy TES

Founded in 2021, Magaldi Green Energy is a start-up of the Magaldi Group (incorporated in 1929) specializing in the research, development, and commercialization of cutting-edge technologies for the generation and storage of renewable energy. The company aims to be at the forefront of the energy transition, driving the shift towards a sustainable energy future. Its mission is to develop disruptive technologies that not only facilitate the decarbonization of energy-intensive industrial processes but also enhance the flexibility and resilience of the electrical grid by offering advanced energy storage solutions and grid support services. Through these innovations, Magaldi Green Energy seeks to play a pivotal role in reducing greenhouse gas emissions and enabling the widespread integration of intermittent renewable energy sources into the energy system [73].

Magaldi Green Energy has developed and patented a new TES technology based on fluidized bed which consists of an insulated tank containing a fluidized particles bed. As a storage material, fluidizable solid silica sand particles are used. Sand is an economical, easy to procure, environmentally friendly, non-toxic, non-flammable and easy to dispose of material. In addition, silica sand particles are stable up to over 1000°C. The fluidized particles bed can operate in three phases:

- **Charge**: in this phase solid particles are heated in order to store the energy in input. In this phase the fluid bed is active to enhance the heat transfer and thermal diffusivity for distributing heat uniformly over the entire volume of the bed.
- **Storage**: in this phase the fluidization is switched off, and the sand packs at the bottom of the module allow the absorbed energy to be stored for days or even weeks. Energy losses are minimized due to the lack of convection and the tank's insulation, which restricts heat exchange with the exterior of the casing.
- **Discharge**: the integrated heat exchanger embedded within the fluidized bed of sand particles is reversed to discharge the system. Activating the fluid bed, accumulated energy is released by means of in-bed heat exchangers, to the heat transfer fluid typically superheated steam (up to 600°C) or other high-temperature fluids required by industrial processes (such as hot air).

A fourth phase can be considered, in fact this technology is able to charge and discharge simultaneously the storage system. In this phase the fluidized bed of sand particles is on and allows to absorption the input energy at same time the heat exchanger release the energy stored previously.

Below is a picture of the fluidized sand bed during the fluidization process.

Figure 20 Fluidized sand bed in fluidization process

To ensure proper operation of the fluidized sand bed, several auxiliary components are required, including an air compressor, air pre-heater, air filter, air fan, and heat exchanger, as illustrated in Figure 21.

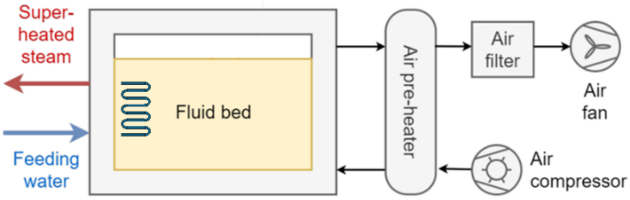

Figure 21 TES based on fluidized bed and auxiliaries' equipment

The components of the TES that make up the auxiliary equipment of the fluidized bed can be organized into subsystems, which form the foundation for the operation of the entire technology:

- **Sand Particles Bed**: The sand is contained in a large, insulated metal tank. The system includes sensors, such as thermocouples at various locations and heights, to monitor temperature uniformity, thermal diffusivity and the amount of stored energy. Pressure transmitters are also used, these ones, together with thermocouples, allow to supervise the fluidization state of the sand bed.
- **Fluidization System**: To enhance heat exchange during charging and discharging, the sand bed is kept in a fluidized state. A compressor blows air into the sand bed through dedicated injection nozzles located at the bottom of the tank, while a fan extracts air from the top and directs it into a filter to remove sand particles before releasing it outside. The compressor and fan are controlled together to maintain the correct airspeed and pressure, ensuring proper fluidization of the bed, which allows immersed metal elements to expand freely without encountering issues. Additionally, an air-to-air heat exchanger pre-heats the cold air entering the tank by recovering heat from the hot exhaust air, which is cooled down to nearly room temperature, thus improving system efficiency.
- **Steam Generation System**: Multiple heat exchangers are immersed in the sand bed, connected either in

series or parallel depending on the application. A pump forces the heat transfer fluid (HTF) to circulate through these exchangers, absorbing heat from the fluidized sand bed. The system maintains a constant output temperature and pressure for the HTF, as required by industrial processes.

Fluidized sand bed technology is the heart of Magaldi Green Energy's TES, from this concept two types of plants can be declined: **MGTES** and **STEM®**. In the first case, the TES is heated by electric resistors by the Joule effect, while in the second case the TES is directly heated by direct solar radiation.

3.1 MGTES

Magaldi Green Energy, a start-up that is part of the Magaldi Group incorporated in 1929, developed the MGTES: an innovative technology to produce green thermal energy – steam or hot air – which can be used directly in industrial plants or for generating electricity by using steam turbines, Figure 22. MGTES, primarily composed of eco-friendly materials like silica sand and steel, offers a flexible modular design adaptable to various process temperatures, storage durations, and energy demands, positioning it as a key player in global decarbonization efforts. This system, whose expected useful life is 30+ years, has all credentials to play a crucial role in the global decarbonization process [74].

3.1.1 Overview and Components

MGTES is a sensible heat TES technology consisting of an insulated tank containing a fluidized sand bed that can be heated either by electrical resistors via the Joule Effect (according to Power-to-X paradigm) or by a HTF, typically steam or hot gases (Heat-to-X applications) [76]. The stored energy can be extracted when needed in the form of superheated steam or hot air, which can be used directly for industrial purposes (X-to-Heat applications) or, when connected to a power block, to generate electricity (X-to-Power applications).

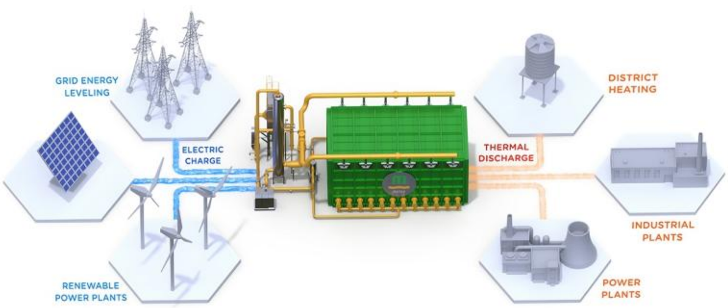

Figure 22 MGTES in Power-to-Heat configuration

In the current market context, MGTES technology is particularly well-suited to Power-to-Heat (P2H) applications, supplying mid-temperature industrial processes, such as those involved in the production of paper, food, and beverages. In these applications, MGTES can partially or fully replace traditional gas boilers, absorbing excess energy from renewable sources and mitigating the negative effects of their intermittent and unpredictability. This makes a significant contribution to power system adequacy and grid security. A first semi-industrial scale prototype of the Power-to-Heat MGTES (Figure 23) has been constructed at Magaldi Power S.p.A.'s production facility in Buccino (SA), Italy. The present discussion focuses on Power-to-Heat applications, particularly the electrical charging system.

Figure 23 MGTES Prototype, Magaldi Power S.p.A.'s production facility in Buccino (SA), Italy

MGTES system utilizes simple silica sand as its storage medium, contained within a large metal tank with thermally insulated walls to minimize heat loss. Despite silica sand having less favorable thermophysical properties compared to other materials suitable for sensible heat storage—such as concrete or cast iron—its low cost makes it an attractive option. Sand has a density of approximately 1500 kg/m^3, a specific heat capacity of around 1 kJ/kg/K, and a volumetric heat capacity of about 1500 $kJ/m^3/K$. Though these values are lower than those of concrete (2340 kg/m^3, 2150 $kJ/m^3/K$) and cast iron (7900 kg/m^3, 6560 $kJ/m^3/K$), the cost advantage of sand (~0.1 €/kg) compared to cast iron (~1 €/kg) makes it economically viable. In addition, sand is an environmentally friendly material, easy to procure and dispose of at the end of the plant's life. The typical size of an MGTES module ranges from 125 to 500 tons of sand, offering thermal storage capacities between 12 and 80 MWh, depending on the amount of sand and the working temperatures. Standard modules operate within a temperature range of 300°C to 600°C, with hot sand reaching up to 600°C. The storage of electrical energy is enabled by a charging system composed of key components, including electrical resistors, power control units, and protective distribution panels. These elements work in tandem to regulate, safeguard, and distribute electrical energy efficiently within the system. In a general configuration the resistors can be positioned in various sections of the system.

The following sections will explore the analysis of different resistor placements within various components of the system, with particular focus on the rationale for selecting the immersion of heating elements directly into the fluidized sand bed. This configuration was chosen to maximize thermal conductivity and heat transfer efficiency, ensuring optimal energy conversion and uniform temperature distribution within the system. The study examines the advantages of this positioning in relation to other potential locations, with considerations of both operational performance and system architecture.

3.1.2 Operation

The MGTES system is designed to capture thermal energy from intermittent renewable sources, store it, and release it as superheated steam. A critical component in achieving this functionality is the air fluidization system. During operation, the fluidization system enables the sand bed to achieve a state of fluidization, enhancing the thermal diffusivity across the entire volume of the bed. In this fluidized state, the sand bed exhibits high thermal conductivity, behaving as an efficient heat conductor.

The degree of fluidization is primarily governed by the velocity of the air blown through the system.

Below is a more detailed analysis of this critical parameter:

- Fluidization velocity is a critical parameter in distinguishing between two primary categories of fluidized beds. When the fluidization velocity is below the terminal settling velocity of an individual particle, the system is classified as a stationary fluidized bed (or packed bed), more commonly referred to as a bubbling fluidized bed. In this configuration, the majority of the particles remain suspended within the bed, while the gas (air in MGTES case) or fluid forms bubbles as it percolates through the particle matrix. This bubbling behavior promotes enhanced gas-solid contact, while still maintaining a relatively dense particle phase, making bubbling fluidize bed systems particularly suitable for processes that require lower fluidization velocities and stable thermal or chemical gradients within the bed [75].

When the air velocity exceeds the minimum fluidization velocity, the bed becomes fully fluidized, facilitating optimal heat transfer. Conversely, if the air velocity falls below the minimum fluidization threshold, the bed reverts to a packed state, characterized by minimal thermal diffusivity, in which it acts as a thermal insulator. This dual behavior allows the system to effectively store and manage thermal energy based on the operational needs [76].

Below, Figure 24, is a representation of a typical 24-hour operation of the MGTES system. The upper graph illustrates the electrical power supplied to the resistors, while the lower graph displays the heat output. The variables P_{e_max} and P_{th_max} represent, respectively, the maximum electrical power that the resistors can absorb, and the maximum thermal power output delivered by the heat exchanger immersed in the fluidized bed. This analysis highlights the dynamic energy conversion process, where electrical energy is intermittently stored and then converted to thermal energy based on system requirements, ensuring continuous heat delivery for industrial processes.

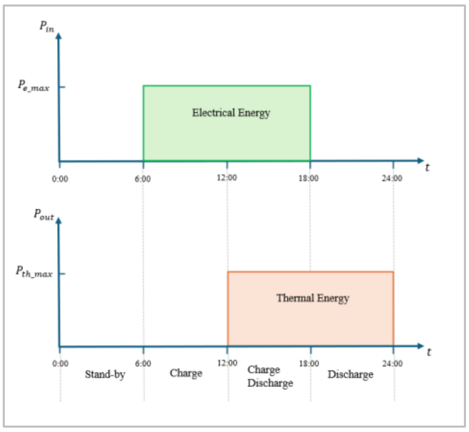

Figure 24 Typical daily operation of an MGTES Module

In a typical daily operation, the MGTES system begins in a standby state at the start of the day. In this condition, the fluidized bed acts as thermal insulation, with minimal energy exchange with the external environment, aside from minor losses due to the high degree of tank insulation.

Later in the day (around 6:00 AM), the MGTES system begins receiving electrical energy input, initiating the fluidization system. This activation enhances thermal diffusivity and the heat transfer coefficient between the resistive elements and the sand. During this phase, the storage system's temperature rises as it enters the charging phase. Unlike electrochemical storage systems, a TES configured for Power-to-Heat (P2H) applications can simultaneously undergo both charging and discharging phases (from 12:00 PM to 6:00 PM). In this scenario, the fluidization of the bed ensures a high heat transfer coefficient between the resistive elements and heat exchanger with the sand particles, allowing efficient energy storage and release.

As daylight diminishes and renewable energy sources are depleted, no further energy input is provided to the resistors, and the charging phase concludes. Despite the cessation of energy input, the system can continue supplying thermal power thanks to the energy stored throughout the day. At this point, the MGTES enters the discharge phase, with the fluidization system remaining active to maintain a high heat transfer coefficient between the sand particles and the thermal exchanger.

Once the temperature of the fluidized bed reaches a minimum threshold, below which the system is considered fully discharged, the fluidization can be turned off. If the system is only partially discharged and no further thermal power is required, the fluidization system can also be deactivated, allowing MGTES to retain the remaining thermal energy within the packed bed until the next day.

3.2 STEM®

Magaldi Green Energy, developed the STEM® system, a modular beam-down CSP/CST technology utilizing sensible heat TES. TES allows CSP/CST plants to generate electricity and thermal energy beyond sunlight hours, increasing their contribution to the energy grid or to the industrial process. Using HSM silica sand, which remains stable up to 1500°C, STEM® can operate at high temperatures without cycle degradation. Its compact design integrates the solar receiver, heat exchanger, and TES in one unit, offering scalable and efficient energy solutions. STEM® provides thermal energy and steam for a range of applications, from industrial processes to desalinization, supporting sustainable development, especially in remote or off-grid areas. With a projected lifespan of over 30 years, STEM® is poised to play a significant role in global decarbonization efforts, aligning with the growing trend of TES-equipped CSP/CST installations.

3.2.1 Overview and components

STEM® uses a fluidised bed of sand as a heat storage medium. Unlike MGTES technology, which uses an electrical resistor to store energy, STEM® stores energy directly from solar radiation and releases thermal energy in the form of superheated steam.
As illustrated in Figure 25, the main components of a STEM® plant are heliostats fields, secondary reflectors (beam-down) and integrated solar receiver. Solar radiation is reflected by tracking mirrors (heliostats) towards secondary mirrors (beam-down reflector), which concentrate it directly onto a central receiver, containing the fluidized bed [77].

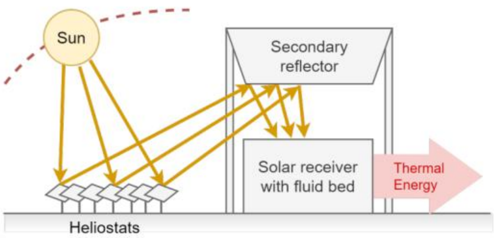

Figure 25 STEM® concept: CS System with heliostats, beam down, and receiver with fluidized bed

- **Heliostats field**: Comprising approximately one thousand heliostats, this system is a critical component of technology, as it facilitates solar tracking. The heliostats are rectangular in shape, and extensive techno-economic analyses have determined that the optimal size for this type of installation is 7 square meters per heliostat. To optimize communication and maximize pointing accuracy, both of which are essential for the overall efficiency of the system, the heliostat field is typically divided into subgroups. This configuration allows for improved control and management of the solar tracking process, directly influencing the system’s energy capture and operational performance.
- **Secondary Reflector**: Also referred to as a beam-down reflector, this component consists of multiple reflective surfaces, each corresponding to a heliostat subfield. These surfaces are precisely oriented to

redirect solar radiation downward into the solar receiver's aperture. The reflecting surfaces are constructed from high-reflectivity material sheets, adhered to finned panels designed for thermal management, and supported by a steel framework. Unlike conventional central receiver systems, where the receiver is positioned at the top of a tall tower, the beam-down system offers the significant advantage of easier access to the solar receiver, which is located at ground level. This design leads to notable reductions in installation and operation and maintenance (O&M) costs. However, one drawback of beam-down systems is that solar radiation undergoes two reflections, which introduces additional losses in the secondary reflector, potentially affecting overall system efficiency. However, the negative impact of the double reflection is minimized by precise optical design and the use of high-reflectivity secondary mirrors [78][79].

- **Solar Receiver**: The integrated solar receiver is a fluidized bed boiler, made of a cylindrical body, internally insulated and refractory lined, provided with an aperture on the top side, to allow the inlet of solar radiation reflected by the beam-down. The solar flux directly irradiates the fluidized sand bed which allows an effective absorption and transfer of solar energy to the entire bed inventory [80]. Solar energy is stored in the bed inventory as sensible heat and can be transferred when requested to the heat exchangers suitably immersed into the sand bed for superheated steam generation [81].

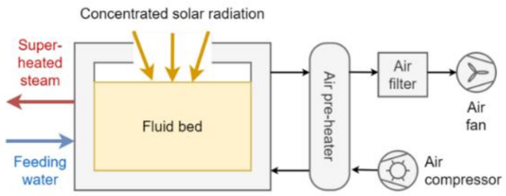

Figure 26 Concept diagram of integrated receiver and its auxiliaries

The auxiliary components are similar to those described in the previous section and are shared with the MGTES twin technology.

- **Automation and Control system**: it includes two different blocks: the first one controls the module heliostats field, while the second deals with Integrated Solar Receiver process. The supervision system of an entire STEM® plant, composed by several modules, coordinates the logics of the modules, according to the Power Block (or thermal load) operation as illustrated by Figure 27.

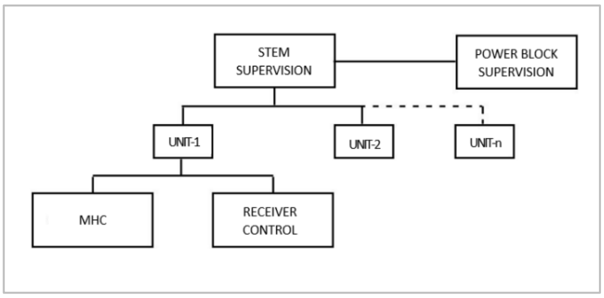

Figure 27 Automation and control system of a STEM® module

This thesis focuses on the control of heliostat fields, with particular emphasis on the Magaldi Heliostat Control (MHC) system, which was developed by the Automation and Control Office within the R&D Division of Magaldi Power.

My internship activities and the development of my Master's thesis immediately involved me in the development of the MHC system, starting with the help of an external company. Upon joining Magaldi Power, I aimed to internalize the entire system to gain full control over its know-how. Initially, I worked alone on the development of MHC, creating a demonstrative prototype that was extensively tested. As the project grew and the need for a reliable system capable of being integrated into an industrial and energy context became apparent, the development team expanded, and I had the opportunity to manage and coordinate it. My role was to integrate and oversee the team’s efforts to ensure a coherent and efficient development process. The successful realization of the MHC system is a testament to both my individual contributions and the collaborative effort of the entire team.

The first experimental STEM® plant, with 100 kW of solar power incident on the heliostats field, was built inside Magaldi industrial facility in Buccino, in the province of Salerno (Italy). A 2 MW industrial-scale plant (Figure 28), comprising 537 heliostats (subdivided into 4 fields), was realized inside the A2A Integrated Energy Pole in San Filippo del Mela, in the province of Messina, Sicily (Italy). The plant was established there to fulfil the request of A2A, aiming to include innovative technologies in its Energy Pole.

Figure 28 STEM® 2 MW industrial-scale plant in San Filippo del Mela, Sicily (Italy)

3.2.2 Operation

As per MGTES, STEM® system has been designed to capture thermal energy from intermittent renewable sources (solar irradiance), store it, and release it as superheated steam. A critical component in achieving this functionality is the air fluidization system. During operation, the fluidization system enables the sand bed to achieve a state of fluidization, enhancing the thermal diffusivity across the entire volume of the bed. In this fluidized state, the sand bed exhibits high thermal conductivity, behaving as an efficient heat conductor.
Below, Figure 29, is a representation of a typical 24-hour operation of the STEM® system. The upper graph illustrates the solar irradiance in input to the heliostats fields, while the lower graph displays the heat output. The variables I_{max} and P_{th_max} represent, the solar irradiance peak toward the heliostats and the maximum thermal power output delivered by the heat exchanger immersed in the fluidized bed respectively.

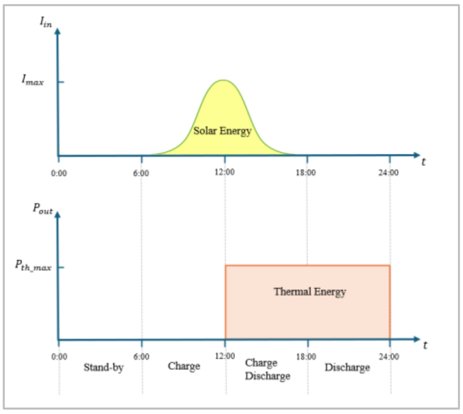

Figure 29 Typical daily operation of a STEM® Module

In a typical daily operation, the STEM® system begins in a standby state at the start of the day. In this condition, the fluidized bed acts as thermal insulation, with minimal energy exchange with the external environment, aside from minor losses due to the high degree of tank insulation.
Later in the day, around 6:00 AM (It is important to note that the time at which solar irradiance becomes sufficient to operate the auxiliary components is influenced by the latitude of the plant location and the time of year.), the STEM® system begins receiving solar irradiance, initiating the fluidization system. This activation enhances thermal diffusivity and makes the fluidized bed a thermal conductor. During this phase, the storage system's temperature rises as it enters the charging phase. Unlike electrochemical storage systems, the STEM® can simultaneously undergo both charging and discharging phases (from 12:00 PM to 6:00 PM). In this scenario, the fluidization of the bed is kept on and ensures a high heat transfer coefficient between the heat exchanger and the sand particles, allowing efficient energy storage and release.
As daylight diminishes and solar irradiance is depleted, no further energy input is provided to the bed, and the charging phase concludes. Despite the cessation of energy input, the system can continue supplying thermal

power thanks to the energy stored throughout the day. At this point, the STEM® enters the discharge phase, with the fluidization system remaining active to maintain a high heat transfer coefficient between the sand particles and the thermal exchanger.

Once the temperature of the fluidized bed reaches a minimum threshold, below which the system is considered fully discharged, the fluidization can be turned off. If the system is only partially discharged and no further thermal power is required, the fluidization system can also be deactivated, allowing STEM® to retain the remaining thermal energy within the packed bed until the next day.

Chapter 4

Heliostat Control applied to STEM

This chapter examines the STEM® system, an advanced TES technology that utilizes sand as a storage medium. Designed to address the limitations of conventional molten salt systems, STEM® provides a scalable, cost-effective solution for integrating renewable energy into power systems and industrial applications, facilitating decarbonization efforts.

At the core of the STEM® system is its solar charging process, which leverages a beam-down reflector configuration combined with a fluidized bed receiver (see Figure 25 e Figure 26). This configuration is managed by an advanced control system, the Magaldi Heliostat Control (MHC). The MHC incorporates two primary innovations: a continuous error-correction algorithm that refines heliostat tracking trajectories based on logged errors, and the use of inclinometers on each heliostat, which enhances pointing accuracy and system robustness by ensuring a precise horizontal reference.

Extensive testing of the MHC control system has been conducted within an industrial context, achieving over 12,000 hours of operation on a 2 MW-scale facility located in San Filippo del Mela, Sicily, Italy (see Figure 28). The outcomes demonstrated significant advancements in pointing precision and reliability, even with the integration of commercially available, off-the-shelf components selected to maintain cost efficiency. A key achievement was the marked reduction in aiming errors, facilitated by the implementation of the integral error-correction algorithm.

The STEM® system integrates several innovative technologies previously uncombined at an industrial scale, including fluidized bed technology, beam-down reflectors, and sophisticated heliostat control with automated calibration through ground-mounted cameras. While these individual technologies have been independently explored in prototypes or conceptual studies, no system has yet unified them into a single operational solution on this scale. This integration allows STEM® to deliver the high accuracy and reliability typical of laboratory environments, while also addressing the cost-effectiveness and durability requirements essential for industrial application.

4.1 MHC - Hardware and Algorithms

This section presents MHC, the heliostats control system of the STEM® technology, developed by Magaldi automation and control R&D department. Figure 30 shows MHC hardware and control connections between components:

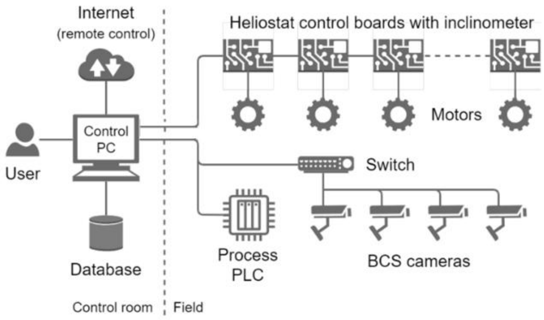

Figure 30 MHC hardware and control connections between main components

This figure represents the hardware architecture for controlling a heliostat system, commonly used in solar thermal energy plants. The system consists of several key components:

- **Control PC**: The central hub in the control room, connected to a database for data logging and analysis. It allows the user to remotely monitor and adjust the system.
- **Database**: Stores data for operational parameters, system performance, and diagnostics.
- **Process PLC (Programmable Logic Controller)**: Interfaces between the MHC and the process field components, executing control commands and managing data flow.
- **Heliostat Control Boards**: Each heliostat is equipped with a control board that includes an inclinometer for precise angular positioning. The control board manages the motors that adjust the heliostat mirrors to reflect sunlight towards the receiver.
- **Motors**: Attached to the heliostats; these linear motors control the movement of the mirrors, adjusting their angles for optimal sunlight reflection.
- **Switch**: Connects the cameras and the PLC to the control PC.
- **BCS (Beam Characterization System) Cameras**: Positioned to monitor the beam alignment and performance of the heliostats, ensuring that the mirrors are correctly focused on the receiver.
- **Internet (Remote Control)**: Enables the system to be monitored and controlled remotely, allowing users to make adjustments and monitor performance from any location.

In this architecture, the PLC according to the needs of the process part, coordinates the actions of the heliostats, controlling the motors based on feedback from the control boards and BCS cameras, while the Control PC provides a user interface and data logging functions for real-time monitoring and control adjustments.

4.1.1 Functionalities

MHC runs on a control PC that communicates with the electronic control boards mounted on every heliostat. The core functionality of MHC is heliostats automatic aiming, performed following as listed below.

1. Aiming trajectories calculation: at a programmable time the control PC calculates the sun path and its relative position with respect to each heliostat, then it converts the trajectory into pitch and roll angles, using kinematic equations. Typically, the calculation is performed at night, obtaining the trajectories of the daylight hours of the following day.
2. Automatic trajectory uploading: the control PC uploads the trajectories to the non-volatile memory of the electronic control boards mounted on every heliostat, communicating by private protocol on serial RS485.
3. Heliostats movement: the control board of each heliostat acts on two motors (one for axis), orienting the heliostat to the desired position, exploiting the signals from incremental encoders. To avoid overloading the power lines, MHC is able to handle the simultaneous movement of configurable sub-groups of heliostats.
4. Heliostats reference positioning: every heliostat is equipped with an inclinometer, used to reset the incremental encoders (mounted on the linear motors) to a known reference position (horizontal). This also rejects potential misalignments, eliminating the need for manual coarse calibration of each heliostat.
5. Heliostats fine calibration based on artificial vision: by means of a camera, target, image processing and a dedicated algorithm, the system verifies the aiming accuracy of each heliostat, correcting the error periodically.
6. Integral error correction system: MHC stores the corrections applied during the heliostat periodic calibration, to take them into account for the following days. In other words, the algorithm uses the experience of past days to improve the pointing of the future days.

4.1.2 Astronomical and Kinematic Model

To calculate sun position, two different algorithms have been implemented: Plataforma Solar de Almerìa algorithm (PSA) [82], Solar Position Algorithm (SPA) [83]. These algorithms take as an input geographical position, date and time to calculate the sun position, in terms of azimuth and elevation angles. The SPA, presenting an average error of ±0.0052 mrad, has been chosen as the default algorithm for STEM®, since it has been proven to be more accurate than PSA [83]. However, it should be noted that, despite the accuracy of the algorithm, the results are affected by the uncertainty on the GPS coordinates of heliostat and receiver. MHC repeats the calculation of the sun position for every minute of the day (or other time interval), obtaining the complete sun path during daylight hours. Then, the target trajectory is calculated for each heliostat, using the roll-tilt/azimuth-elevation equations, knowing the relative position of the heliostat with respect to the central tower, as summarized in Figure 31. The resulting aiming trajectory represents the heliostat orientation angular trajectory to achieve an accurate solar focusing on the receiver cavity. The aiming trajectory is uploaded to the heliostat control board and stored in a non-volatile memory.

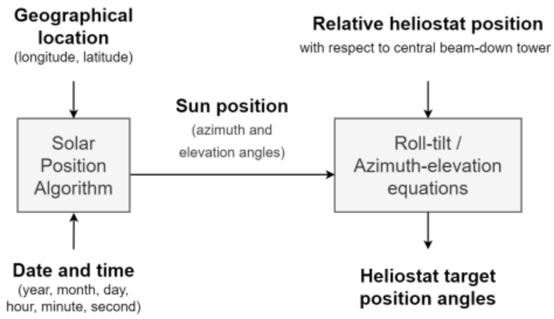

Figure 31 Aiming trajectory calculation algorithm

The mechanical supporting structure of heliostats, made of rigid links and joints, is an industrial robot moved by two linear motors (one per axis). Such a system is described analytically in 3D by a kinematic model, implemented into MHC. The inverse kinematic model, based on one of the Denavit–Hartenberg (D-H) conventions, allows to calculate the motor steps that achieve the desired heliostat orientation, based on data from motor encoders, measuring the current position of the joints and controlling the robot links in space. Two types of D-H conventions exist: classical and modern [84]; both D-H approaches have been implemented in MHC, in order to verify the model validity.

4.1.3 Heliostat calibration and integral error correction system

In concentrating solar systems, pointing must be highly accurate in order to maximize the energy collection at the receiver. It should be noted that the model described above can be used on its own only if proper environmental conditions are guaranteed. Therefore, in real applications a calibration system is needed to improve the heliostat pointing accuracy.

As part of the development of an industrial scale system, more sophisticated algorithms have been used to achieve the accuracy and reliability of state-of-the-art systems with the use of cheaper hardware. In particular, for the pointing of the heliostats, STEM® uses linear actuators equipped with incremental encoders, a less expensive alternative compared to the absolute encoders referred to in the existing literature. This choice required the integration of a Micro Electro Mechanical System (MEMS) chip in each heliostat control board, which measures the gravitational acceleration to act as an inclinometer. The MEMS allows the heliostat to be aligned to the reference (horizontal) position. The motor encoders can be reset to this position. Although it is an open-loop control, this configuration ensures a significant preventive reduction in pointing errors that occur due to ground offset or deformation of the supporting mechanical structure. It should be noted that using inclinometers in this way (in a horizontal position) allows them to be used to their maximum accuracy. In order to assess and correct the pointing error, a calibration system has been implemented by developing a Beam Characterization System (BCS) using artificial vision. Each heliostat periodically points at the BCS target, and a camera captures the target image. The image is processed by the control PC, which measures the displacement between the centroid of the sunspot and the desired pointing position, i.e. a black circle on the

BCS target. Measured pointing errors are processed to calculate corrective adjustments for each heliostat, which are then stored in the control PC for future application. While the BCS described in the literature effectively corrects minor inaccuracies, it cannot compensate for larger errors that prevent the sunspot from focusing accurately on the calibration target, necessitating manual coarse calibration. The MHC addresses this limitation by combining the BCS with MEMS, thereby reducing pointing errors even in challenging environmental conditions (e.g., heavy rain, wind, seismic activity) and mitigating substantial heliostat misalignments. This integration is advantageous for site construction, as it reduces the requirement for extensive civil infrastructure to counteract ground settling.

Furthermore, unlike other systems documented in the literature, MHC employs an innovative algorithm that refines pointing trajectories (pitch and roll angles) during nighttime. This algorithm applies the BCS-corrected adjustments recorded over previous days to further minimize pointing error and improve accuracy. By implementing the integral corrections algorithm, the system leverages historical error data to proactively prevent similar inaccuracies in future days. Figure 32 shows a diagram of the complete trajectory generation procedure.

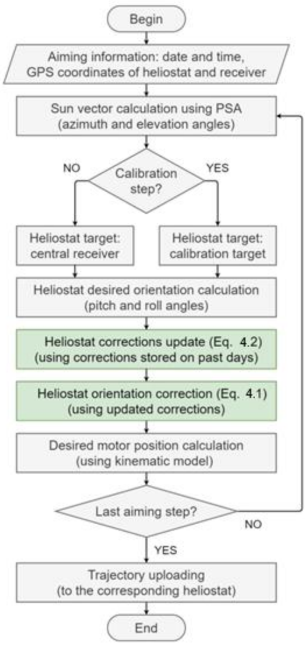

Figure 32 MHC trajectory generation procedure, with integral error correction

The trajectory $\theta_H^{(h,d)}(t)$ of each heliostat h for day d is calculated from the nominal trajectory $\theta_N^{(h,d)}(t)$ obtained from the astronomical and kinematic equations, adding an integral correction $\theta_C^{(h,d-1)}(t)$.

$$\theta_H^{(h,d)}(t) = \theta_N^{(h,d)}(t) + \theta_C^{(h,d)}(t) \tag{4.1}$$

The updated correction is obtained by summing two values saved the previous day $d-1$: the integral correction $\theta_C^{(h,d-1)}(t)$ and the BCS-estimated adjustment $\theta_{BCS}^{(h,d-1)}$

$$\theta_C^{(h,d,n)} = \theta_C^{(h,d-1,n)} + \theta_{BCS}^{(h,d-1,n)} \tag{4.2}$$

$\theta_C^{(h,d-1,n)}$ is the integral corrections term, which incorporates the cumulative error data from previous operational periods of the plant.

4.2 Experimental Test Results

The first experimental STEM® plant was built inside the Magaldi industrial complex in Buccino, in the province of Salerno (Italy). It has produced 100 kW of solar power incident on the heliostat field. A 2 MW industrial plant (Figure 33) with 537 heliostats (divided into 4 fields) has been realized inside the A2A Integrated Energy Pole in San Filippo del Mela, in the province of Messina, Sicily (Italy). The plant was built there in response to A2A's desire to incorporate innovative technologies into its Energy Pole. Actually, CSPs exhibit optimal performance at lower latitudes in Middle East North Africa (MENA) regions; in fact, Sicily's latitudes have lower solar elevation angles and bad weather conditions (in terms of cloudy and rainy days) during the winter season, leading to reduced solar irradiation, limited sunshine hours, and shorter daylight periods, thus implying restricted CSP operation. In summer, however, the environmental conditions in Sicily are close to those found at the installation sites, thus emulating the MENA environment. Therefore, tests on STEM® in deep autumn, winter and early spring have not been reported.

Figure 33 2 MW industrial-scale plant in San Filippo del Mela, Sicily (Italy) [73]

According to the update document on the status of guidelines for heliostat testing activities [85], there is currently no procedure that clearly identifies how to assess the pointing error for a heliostat field. However, SolarPACES has collected and published, with the support of experts, guidelines for the performance testing of individual heliostats [86]. These guidelines have been used to evaluate the pointing accuracy of the MHC system, and although they focus on testing only one sample heliostat, providing a suggestion for dealing with pointing error for a population of heliostats. In order to assess the pointing accuracy of the MHC, which affects the thermal input power delivered to the STEM® receiver, several test campaigns were carried out during the 12000 hours of operation of the system, measuring the pointing error for the *x* and *y* axes on a target for each heliostat *h* several times *t* during the day. As suggested in [86], the results were processed by summing the errors using the root mean square operator (4.3) to obtain a single error value.

$$Err_t = \sqrt{\frac{1}{H}\sum_h Err_{h,t}^2} \tag{4.3}$$

$$Err_{tot} = \sqrt{\frac{1}{T}\sum_t Err_t^2} \tag{4.4}$$

Twenty heliostats were randomly selected for a 5-month test campaign and operated with 4 different control modes to evaluate the effect of different control types.

		Pointing error [mrad]	
BCS	Integral Correction	RMS	Std dev
No	No	1.39	0.86
Yes	No	0.95	0.52
Yes	Learning	0.74	0.21
Yes	Post-Learning	**0.52**	0.38

Table 7 Global pointing error statistics for 5 months, using different control type

Figure 34 shows the daily RMS target error values along 5 months. The 4 control modes are highlighted in different colors. Heliostats were operated without BCS for their first 40 days (red), then with BCS for a further 40 days without integral error correction (yellow), reducing global aiming error by approximately 32%. Finally, after an initial ‘learning’ period of 20 days, activation of the integral correction system reduced the errors by a further 45%. In addition, the system maintained its low global pointing error despite windy and rainy days that could have caused heliostat misalignment, which was prevented by MHC, confirming the quality and reliability of the system developed.

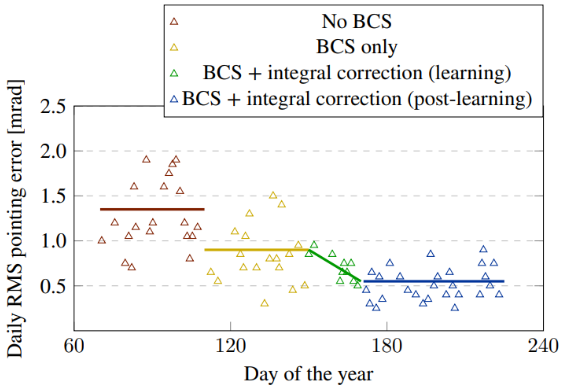

Figure 34 Daily RMS pointing error trend along 5 months, showing the effect of BCS and integral error correction system

As shown in bold in the last row of Table 7, after the learning phase, the system has an RMS error of 0.52 mrad for the global pointing. This value is close to the lower bound of the range 0.1 ÷ 1 mrad, reported in Table 8, summarizing global errors from different scientific documents describing similar heliostat control systems.

Reference Document	Pointing error [mrad]	Value Type
Harper et al. [89]	1.0	declared
Zavoico [90]	1.0	declared
Berenguel et al. [91]	0.9	calculated
Strachan and Houser [92]	0.61	calculated
Sattler et al. [88]	0.1	estimated

Table 8 Global pointing error comparison with similar heliostat control systems in the scientific literature. Berenguel et al. value has been calculated by transforming the error from cm to mrad considering a heliostat at an average distance from the target of 100 m. Strachan and Houser pointing error has been calculated by using the Euclidean distance from the azimuth and elevation components

For [88] and [92], the value of the global pointing error was not explicit, so a calculation was necessary.

Chapter 5
MGTES Charging System Characterization

The MGTES system integrates an electric charging system, utilizing resistive heating elements to absorb energy from a renewable power source and store it as thermal energy within the sand medium. These resistive elements, or heaters, convert renewable electrical energy into thermal energy via the Joule effect, achieving high conversion efficiency. A comprehensive analysis of resistor types and their optimal configuration within the system has been central to the design, with the objective of maximizing electrical-to-thermal energy conversion efficiency. Key factors examined include heating mechanisms, design assumptions, thermal conductivity, electrical resistance properties, and spatial distribution, all of which are crucial for ensuring uniform heat distribution and efficient thermal transfer within the storage medium.

Simulations, based on analytical models, were conducted to evaluate resistive elements designed for heating through conduction, convection, and radiation. This was followed by an experimental testing campaign to validate the theoretical models, confirming both simulation accuracy and the actual performance of the heating systems under study. A SWOT analysis was then conducted, focusing on primary qualitative aspects such as ease of installation, maintenance requirements, replaceability of components, compatibility with the storage medium and cost-effective. These factors were systematically evaluated within the SWOT matrices, providing a structured assessment of the system's potential and challenges.

5.1 Heating Modes

The challenge of heating the storage medium can be addressed from a more general and conceptual perspective, focusing on two key aspects:

- **Heat transfer mechanisms**: In this approach, heat is transferred from the electrical heaters to the heat storage medium (HSM). Several distinct heating modes, outlined below, are possible for this process.
- **Self-heating of the HSM**: This method involves generating heat through the Joule effect, where electrical current flows directly through the HSM, causing the heat up of the HSM and the storage of the energy.

However, the self-heating method, where the heat is directly generated in the storage medium via the Joule effect, is not feasible for MGTES. This is due to the high electrical resistivity of sand, which significantly impedes current conduction. Consequently, only indirect heat transfer methods, where heat is transferred from external sources to the HSM, are considered viable for MGTES applications.

Several methods are available for transferring heat to the fluidized bed, with the most viable options illustrated in the Figure 35. Each method will be rigorously evaluated in terms of quantitative and qualitative parameters, including heat transfer efficiency, thermal diffusivity, and energy conversion rates. Additionally, we will assess the applicability and technical feasibility of these methods in large-scale industrial implementations, considering factors such as scalability, operational reliability, and integration with existing industrial processes. This comprehensive analysis will guide the selection of the most efficient heat transfer mechanism for the industrial version of the system.

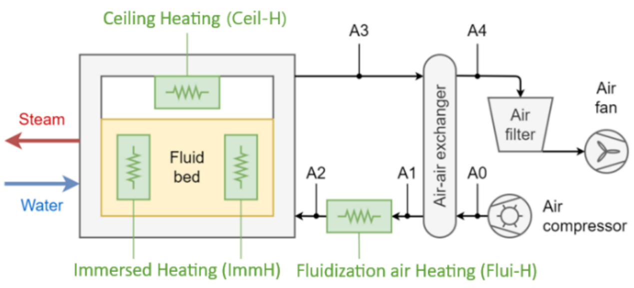

Figure 35 Main MGTES components with different modes for charging: convective, radiating, and fluidization air heating

For a comprehensive analysis of heat transfer within the fluidized bed system, it is crucial to consider all the modes of sensible heating as defined by the laws of thermodynamics. Sensible heating refers to the process of transferring heat to or from a substance, resulting in a change in temperature without a phase change.

5.1.1 Convective Heating (CH)

Convection occurs in the presence of a fluid; in the context of MGTES, the air employed for fluidization generates a mixture with the sand that facilitates enhanced thermal conductivity between the solid particles and the fluidizing air. The governing equation for convective heat transfer is:

$$P_{conv} = hA(T_H - T_S) \tag{5.1}$$

where:

P_{conv} is the convective heat transfer rate (W),

h is the convective heat transfer coefficient ($W/m^2 \cdot K$),

A is the surface area available for heat transfer (m^2),

T_H is the temperature of the heater surface (K),

T_S is the temperature of the sand fluidized bed (K).

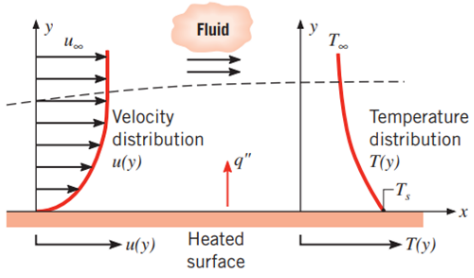

Figure 36 Boundary layer development in convection heat transfer [93]

In the context of MGTES, convective heating occurs when the heaters are strategically located either along the air fluidization circuit or within the tank, immersed in the fluidized bed.

5.1.2 Radiative Heating (RH)

Radiation heat transfer occurs through electromagnetic waves and does not require any medium for heat transfer. In this case, the transferred power P is a function of the fourth power of the temperature of the heaters T_H and that of the sand bed T_S, in accordance with Stefan-Boltzmann's law:

$$P_{rad} = \varepsilon\sigma A(T_H^4 - T_S^4) \qquad (5.2)$$

where:

P_{rad} is the radiative heat transfer rate (W),

ε is the emissivity of the surface (dimensionless),

σ is the Stefan-Boltzmann constant (5.67×10^{-8} W/m^2K^4)

A is the surface area of the radiating body (m^2),

T_H is the temperature of the heater surface (K),

T_S is the temperature of the sand fluidized bed (K).

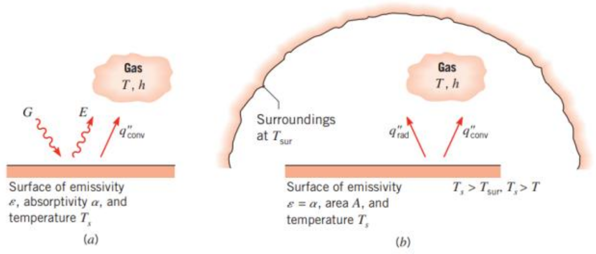

Figure 37 Radiation exchange: (a) at a surface and (b) between a surface and large [93]

When the heaters are positioned on the ceiling of the tank, although there is a minor contribution to heat transfer via convection, the predominant mechanism of heat transfer is radiation.

5.1.3 Conduction Heating

Conduction is a fundamental heat transfer mode in solid materials like the particles of the fluidized bed. In the MGTES system, this could occur between the heaters and the solid sand particles. The rate of heat conduction through the material is governed by Fourier's Law

$$P_{cond} = kA\left(\frac{T_H - T_S}{d}\right) \tag{5.3}$$

P_{cond} is the heat flux due to conduction (W),

k is the thermal conductivity of the sand (W/m·K),

A is the cross-sectional area through which the heat is conducted (m^2),

T_H is the temperature of the heater surface (K),

T_S is the temperature of the sand fluidized bed (K).

d Is the distance between heater surface and the particles sand (m)

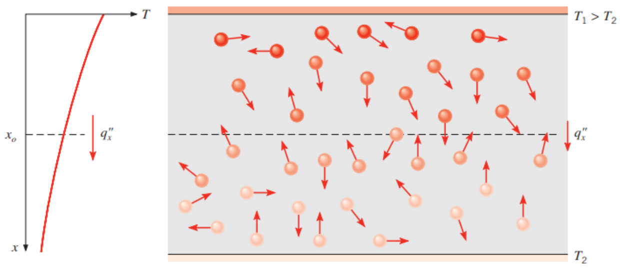

Figure 38 Association of conduction heat transfer with diffusion of energy due to molecular [93]

When the heaters are positioned inside the tank, immersed in the fluidized bed, it could be possible to transfer the heat through this mode.

5.2 Assumptions

It is necessary to examine the previously stated parameters more carefully. Specifically:

1. The fluidized sand bed is considered isothermal, meaning that the sand temperature, T_S is assumed to be uniform throughout the system. In other words, every portion of the bed is assumed to be at the

2. same temperature, without significant gradients within the medium. Similarly, the heaters are modeled as isothermal elements, meaning the temperature T_H is representative of the entire heating element. These assumptions align with reality, particularly when efficient fluidization ensures high thermal diffusivity.
3. Both T_S and T_H are considered time-invariant due to the slow dynamics of thermal phenomena. Furthermore, they can be treated as independent of one another within this model.
4. Given that the walls of the MGTES module are well-insulated, all heat losses to the external environment are neglected. Therefore, heat transfer is assumed to occur exclusively from the heaters to the sand. This simplification implies that the system's thermal energy exchange is confined within the boundaries of the fluidized bed, allowing for a more accurate analysis of heat transfer efficiency between the heaters and the sand medium.
5. The fluidization velocity is considered constant across the entire air inlet area. This approximation is valid because MGTES systems are designed with an optimal distribution of fluidization air nozzles, ensuring uniform air flow and homogeneous fluidization throughout the bed. The uniformity of air distribution minimizes local variations in velocity, which could otherwise lead to uneven fluidization, temperature gradients, or operational inefficiencies. Consequently, this design feature ensures effective heat transfer and consistent performance across the entire bed.
6. Considering the positioning of the heaters along the fluidization circuit, it is assumed that heat transfer occurs exclusively through convection. This assumption is reasonable because, with the heaters immersed in the air, the contributions from radiation and conduction are negligible. In such a configuration, the convective heat transfer dominates due to the continuous movement of air particles around the heaters, enhancing the heat exchange efficiency. The thermal conductivity of air and the low radiative heat transfer in this setup further justify the neglect of conduction and radiation effects in the overall heat transfer process.

$$P = P_{conv} + P_{rad} + P_{cond} \approx P_{conv} \tag{5.4}$$

7. In the configuration where the heaters are positioned inside the tank on the ceiling, the upper surface of the fluidized sand bed receives the majority of irradiation from the heaters. In this arrangement, even though there is air in the space between the ceiling and the bed, the thermal power exchanged through radiation is considered predominant. This is because the air in this region is relatively stagnant, meaning it is not actively forced or convected, and therefore does not significantly contribute to convective heat transfer. Additionally, the heaters are arranged in such a way that their view factors—which describe the geometrical relationship between the radiating surfaces and the receiving surface—favor radiation heat transfer. The direct line-of-sight between the heaters and the sand bed enhances the radiation heat exchange, while the lack of forced air movement means that convective losses are minimal. Consequently, radiation becomes the dominant mechanism of heat transfer in this configuration, as it is the most effective

mode of energy exchange under these conditions.

$$P = P_{conv} + P_{rad} + P_{cond} \approx P_{rad} \tag{5.5}$$

8. Once the heaters are positioned within the tank and fully immersed in the fluidized sand bed, at first glance it would be reasonable to assume that conduction will be the primary mechanism of heat transfer, given that the heaters are in direct contact with the sand particles. Actually, the primary mode of thermal exchange is governed by convection. This arises from the fact that, under fluidized conditions, the sand bed exhibits fluid-like behavior due to the continuous formation and movement of air bubbles. In a bubbling fluidized bed, the continuous motion of air bubbles and sand particles facilitates efficient convective heat transfer between the heaters and the sand. While conduction would indeed dominate if the bed were packed and stationary, in practice, the system is always operated in a fluidized state where convection prevails. Conduction becomes the dominant mode of heat transfer only in a packed bed, but this operational condition is deliberately avoided in MGTES systems to maintain optimal heat transfer performance.

$$P = P_{conv} + P_{rad} + P_{cond} \approx P_{conv} \tag{5.6}$$

9. Assuming uniformity and temporal invariance of the temperatures T_S and T_H, the convective heat transfer coefficient k can be considered uniform throughout the system. With this simplification is possible effectively streamline calculations related to heat exchange, ensuring a consistent approach in both theoretical and practical applications within the system.
10. To calculate the heat exchange between the heaters and the fluidized bed, a simplified and specialized version of the first law of thermodynamics is used, tailored to the specific case. The equation is derived based on the following assumptions: if the fluid is approximated as an ideal gas with constant specific heats , the difference in enthalpies (per unit mass) between the inlet and outlet flows may then be expressed as $i_{in} - i_{out} = c_p(T_{in} - T_{out})$, where cp is the specific heat at constant pressure and T_{in} and T_{out} are the inlet and outlet temperatures, respectively. If the fluid is an incompressible liquid, its specific heats at constant pressure and volume are equal, $c_p = c_v = c$. Assuming steady-state conditions, no changes in latent energy, and no thermal or mechanical energy generation, the equation of the first law of the thermodynamic is simplified in steady-flow thermal energy equation [93].

$$q = mc_p(T_{in} - T_{out}) \tag{5.7}$$

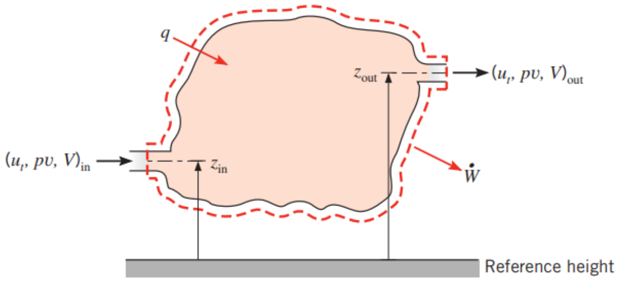

Figure 39 Conservation of energy for a steady-flow, open system [93]

11. The fluidisation velocity is considered uniform and constant over time and calculated as the minimum fluidisation velocity is 2 cm/s [94]:

$$v = \frac{Q_m}{S_{bed}\rho_{bed}(T_{\frac{bed}{2}}, P_{\frac{bed}{2}})} \quad (5.8)$$

where:

v is the fluidization air velocity (cm/s)

Q_m fluidization air mass flow rate (kg/s)

S_{bed} fluid bed section (m^2)

ρ_{bed} air density bed (kg/ m^3)

$T_{\frac{bed}{2}}$ Bed temperature at half height (°C)

$P_{\frac{bed}{2}}$ Bed pressure at half height (mbar)

5.3 Analytical evaluation

In order to predict the behavior of the heaters in various operating modes and assess their practical feasibility, analytical models were developed, incorporating all the assumptions made in the previous section. The simulations were performed using an explicit resolution method, meaning that the quantities were evaluated only at the current and immediately preceding time steps. Part of the code was written in Scilab, while another part was developed in Python.

The simulations were conducted with a setup involving approximately 36 tons of silica sand, a compressor, and heaters positioned in three different locations within the system:

- Inside the tank and immersed in the sand by means of immersed heaters (**Imm-H**),
- Along the fluidization air duct by means of an air-heater (**Flui-H**),
- Mounted on the ceiling of the tank by means of a radiant panel (**Ceil-H**).

The simulations considered thermal charging cycles of the fluidized bed and evaluated the following parameters:

- The temperature reached by the sand at the end of the charging cycle and the charging duration,
- The temperature reached by the heating elements,
- The fluidization velocity,
- The power output of the heaters.

These models provide a detailed analysis of the thermal and fluid dynamic behavior under varying configurations, enabling optimization of the system for different operating conditions.

5.3.1 Imm-H Configuration

In this case the heaters are inside the tank and immersed in the sand, the heat is transferred by convention phenomena, below some simulations results:

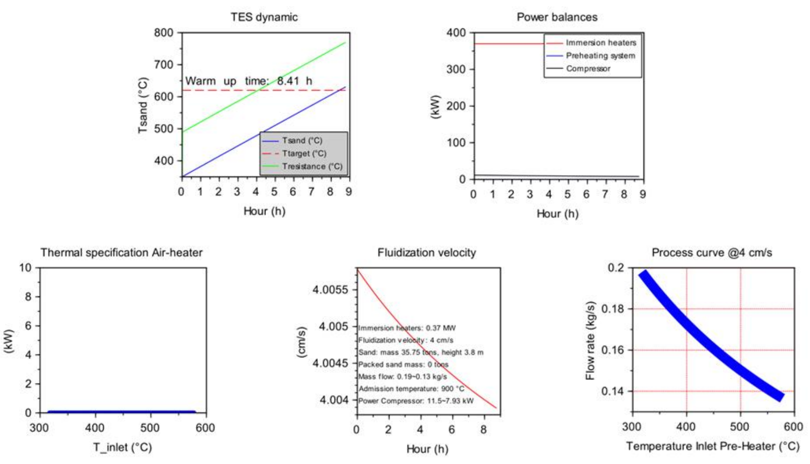

*Figure 40 **Imm-H** heating mode simulation: Silica sand, 36 t, Power compressor ~ 10 kW*

The image contains five different graphs, each representing a specific aspect of the TES system's dynamics and performance during a simulation involving immersion heaters. Here's a commentary on each graph:

1. **TES Dynamic (Top Left)**:

   The graph shows the temperature profile of the sand (T_{sand}), the target temperature, and the temperature of the heaters ($T_{heaters}$) over time. The system reaches the target temperature after a warm-up time of approximately 8.41 hours, as indicated. The behavior of the sand temperature steadily rises towards the target, showing that the system is progressively charging. The heater temperature (T_h) remains slightly above the sand temperature, suggesting effective heat transfer.

2. **Power Balances (Top Center)**:
   This graph depicts the power contributions from different components: immersion heaters, preheating system, and compressor over the same period. The immersion heaters (Imm-H) supply the majority of the thermal power required for the system, as indicated by the power balance graph. The preheating system is set to zero, implying that no power is allocated to this component, and the compressor consumes a minimal amount of power, primarily to maintain fluidization. This power distribution emphasizes the significant role of immersion heaters in transferring thermal energy and the ability of the fluidized bed to efficiently absorb and distribute this heat.
3. **Thermal Specification of Air Heater (Bottom Left)**:
   This graph relates the inlet air temperature of the air heater (T_{inlet}) to its power output. The power heater is set to zero because the simulation provides just the Imm-H case.
4. **Fluidization Velocity (Bottom Center)**:
   The fluidization velocity is plotted against time. The value remains around 4.0045 cm/s, indicating a stable fluidization regime. This stability ensures efficient heat transfer between the sand particles and the heating elements and a minimal compressor power consumption that lead to have a greater efficiency of the entire system.
5. **Process Curve (Bottom Right)**:
   The graph shows a process curve for the fluidization velocity at 4 cm/s as a function of the temperature at the inlet pre-heater. The curve decreases, showing that as the pre-heater temperature increases, the air flow rate decreases. The reduction in air flow rate is due to the increase in air density with rising temperature. As the temperature increases, the air becomes denser, allowing for a lower volumetric flow rate while still maintaining the same fluidization velocity. This, in turn, reduces the workload on the compressor, leading to lower energy consumption. By adjusting the flow rate in response to the temperature change, the system optimizes its operation, achieving energy savings while maintaining effective fluidization of the bed.

Overall, these graphs provide valuable insights into the dynamic thermal behavior of the system, fluidization characteristics, and the distribution of power among components during the heating cycle. The immersion heaters exhibit efficient heat transfer with the sand, operating effectively at a fluidization velocity of 4 cm/s. Additionally, they do not show any signs of over-consumption as the temperature increases, indicating that the system remains energy-efficient even under higher thermal loads.

5.3.2 Flui-H Configuration

In this case the heaters along the fluidization air duct in order to heats the inlet air coming from the compressor, the heat is transferred by convention phenomena:

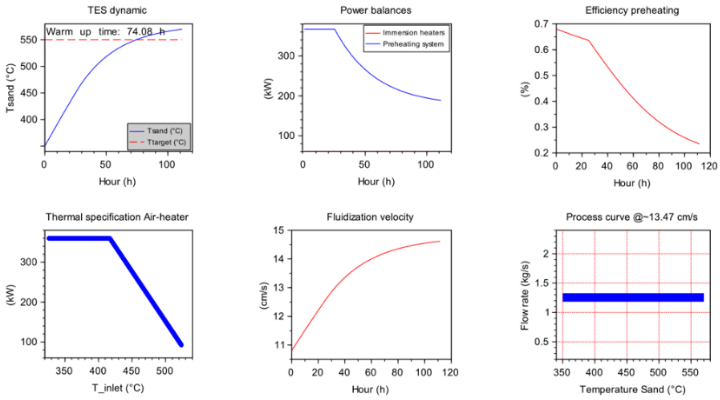

*Figure 41 **Flui-H** heating mode simulation: Silica sand, 36 t,*

This figure provides a detailed analysis of the performance of the air-heater system in a TES setup, which preheats the input fluidization air, offering insights into various thermal and process dynamics.

1. **TES Dynamic (Top Left)**:

   The plot shows the temperature increase in the TES over time, with a target temperature of approximately 550°C. The warm-up time is around 74 hours. The sand temperature (T_{sand}) is consistently rising, suggesting that the preheating phase is ongoing but not yet complete. The extended warm-up period indicates that the system requires a significant amount of time to reach the desired thermal equilibrium.

2. **Power Balances (Top Center)**:

   This graph illustrates the power distribution of the preheating system. Initially, the power input is at its maximum and remains constant, but it gradually decreases as the system temperature increases. This phenomenon is attributed to the action of the air-heater temperature control, which modulates power output based on the temperature of the electrical resistances. Specifically, as the temperature of the sand rises, the temperature of the electrical heaters also increases until reaching a threshold value, beyond which the control system reduces the power to prevent overheating.

3. **Efficiency Preheating (Top Right)**:

   The efficiency of the preheating system decreases as sand temperature increases, with efficiency dropping significantly over the 120-hour period. The reduction in efficiency is due to the reduction in the temperature difference between pre-heated fluidizing air and sand temperature as reports the equation (5.1).

4. **Thermal Specification of Air Heater (Bottom Left)**:

   The plot shows the relationship between the inlet air temperature (Input Fluidizing Air Temperature - T_{inlet}) and the power output of the air heater. As the inlet temperature increases from 300°C to 420°C, the power supplied by the air heater remains relatively constant at around 370 kW. Beyond 420°C the power decreases as the T_{inlet} rises, this is due to power control modulation to avoid resistances overheating (same reason explained for the Power Balances graph).

5. **Fluidization Velocity (Bottom Center)**:

   The graph tracks the fluidization velocity, showing a steady increase from around 11 cm/s to nearly 13.5 cm/s over 120 hours. This increase suggests that as the sand temperature rises, the system needs to raise air flow in order to absorb more power from the heater element of the air-heater to compensate for the reduction of the power explained before.

6. **Process Curve @ 13.47 cm/s (Bottom Right)**:

   This plot represents the relationship between the sand temperature and the flow rate of the air at a fluidization velocity of 13.47 cm/s. The curve is relatively flat, showing that the flow rate remains stable across the temperature range from 350°C to 550°C. The flow rate does not decrease as the sand temperature increase because, although fluidization air becomes denser with temperature so it could be reduce the flow rate, there is a reduction of the power that needs to maintain high the flow rate to absorb more power from the heater elements.

This analysis highlights the thermal dynamics and operational behavior of a fluidized bed TES system equipped with an air heater. The system exhibits power derating as the sand temperature increases, due to the temperature control mechanism of the air-heater. Additionally, the system operates with a high fluidization velocity, which results in a high air flow rate. This, in turn, leads to increased energy consumption by the compressor, contributing significantly to the overall system's operational cost and efficiency.

5.3.3 Ceil-H

In this case the heaters are radiant panels, and they are inside the tank, the heat is transferred by irradiation phenomena:

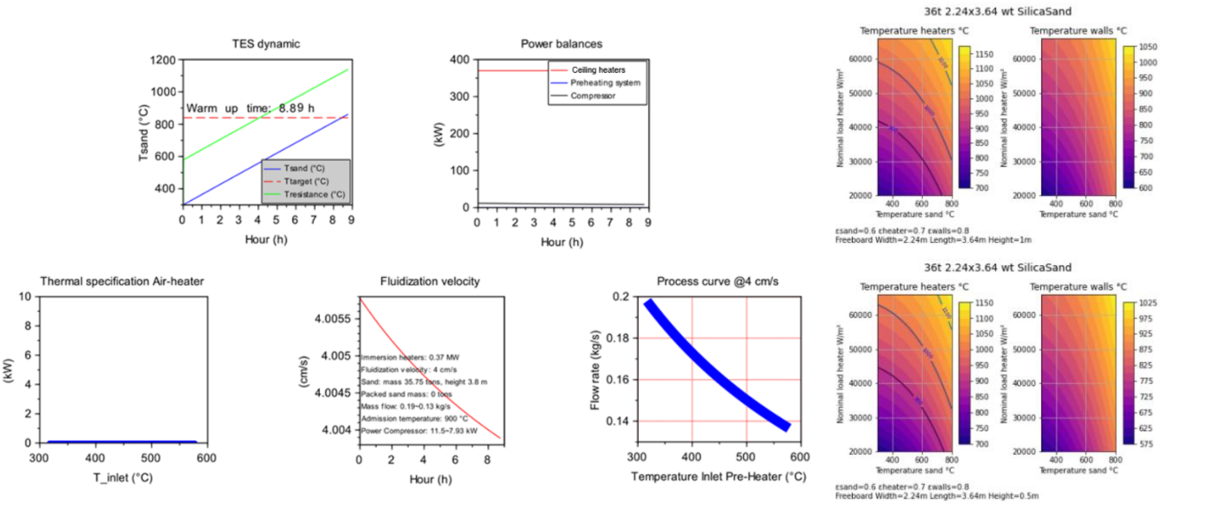

Figure 42 ***Ceil-H*** *Heating modes simulation: Silica Sand 36 t. (a) on the left, dynamic simulation (b) on the right, static simulation*

For the Ceil-H heating configuration, it is assumed that a certain number of heaters, referred to as radiant panels, are fixed to the ceiling of the tank that contains the fluidized bed of sand. Radiant panels provide thermal power to the fluidized bed primarily through radiation. Simulations were performed using the following parameters:

- ε_{sand}: sand emissivity (radiative property of the surface)
- $\varepsilon_{heather}$: heather emissivity
- $\varepsilon_{heather}$: walls emissivity
- *Freeboard Width*: width of the space between the top sand bed surface and the radiative panels
- *Bed Height*: height of the sand volume contained in the tank
- *Distance*: distance between the top sand bed surface and the radiant panels
- *Nominal Load Heater*: power density of the radiant panels
- *Temperature heater*: temperature of radiant panels

In addition to the dynamic simulation (performed to allow a comparative analysis with other heating modalities), a static simulation was conducted using an alternative approach. Below are the considerations derived from the dynamic simulation results (Figure 42 – (a)):

1. **TES Dynamic (Top Left)**:

   The graph shows the temperature profile of the sand (T_{sand}), the target temperature, and the temperature of the heaters ($T_{heaters}$) over time. The system reaches the target temperature after a warm-up time of approximately 8.9 hours, as indicated. The behavior of the sand temperature steadily rises towards the target, showing that the system is progressively charging.

   The heater temperature remains above the sand temperature, suggesting effective heat transfer. A comparison of this chart with the corresponding chart for the Imm-H system reveals a lower rate of heat transfer.

2. **Fluidization Velocity (Bottom Center)**:
   The fluidization velocity is plotted against time. The value remains around 4 cm/s, indicating a stable fluidization regime. This stability ensures efficient heat transfer between the sand particles and the heating elements and a minimal compressor power consumption that lead to have a greater efficiency of the entire system.
3. **Process Curve (Bottom Right)**:
   The graph shows a process curve for the fluidization velocity at 4 cm/s as a function of the temperature at the inlet pre-heater. The curve decreases, showing that as the pre-heater temperature increases, the air flow rate decreases. The reduction in air flow rate is due to the increase in air density with rising temperature. As the temperature increases, the air becomes denser, allowing for a lower volumetric flow rate while still maintaining the same fluidization velocity. This, in turn, reduces the workload on the compressor, leading to lower energy consumption. By adjusting the flow rate in response to the temperature change, the system optimizes its operation, achieving energy savings while maintaining effective fluidization of the bed.

The Figure 42 – (b), presents two cases where all parameters remain constant except for the distance between the radiant panels and the surface of the fluidized bed. In both cases, a pair of graphs (upper and lower) are displayed, showing the nominal loads of the heaters as a function of the sand temperature, indicating the temperature reached by both the heaters and the tank walls.
The simulation results indicate that in both configurations, with a constant power density, increasing the sand temperature also raises the temperature of the heating elements and walls. Moreover, a spatial difference of 0.5 meters in the distance between the radiant panels and the bed surface was considered in the analysis. As demonstrated in the graphs, reducing this distance enhances heat transfer efficiency. Conversely, increasing the separation results in higher temperatures for both the radiant panels and the walls at equivalent sand temperatures and power densities.
These simulations can also be applied to address a synthesis problem. By accounting for the maximum allowable temperatures for both the walls and heaters, the maximum power density compatible with a given sand temperature can be deduced. This approach helps ensure the system operates within safe limits while maintaining effective heat transfer within the fluidized bed.
The simulations indicate that the top-down radiant heating configuration, with heaters positioned above the fluidized bed, aligns optimally with the MGTES system’s geometric and optical parameters. The graphs in Figure 42 illustrate multiple operational points where power density and heater temperatures are well-matched with the thermal profile of the fluidized sand bed. This compatibility promotes efficient heat transfer, enhancing the energy storage and release processes critical to maintaining thermal stability and maximizing system efficiency.
While fluidization velocity is theoretically independent of the heating process in a fluidized bed, practical

application requires that this velocity exceed a minimum threshold. This is essential for proper heat distribution across the bed, as radiated heat on the upper surface must disperse evenly. Failing to meet this condition can result in excessive re-radiation, causing an abnormal rise in radiator temperatures.

In summary, although based on an approximate model, the simulation results are promising. The use of radiant panels has shown potential for efficient heat distribution, minimizing risks of overheating. This outcome highlights the system's thermal stability and effectiveness, crucial for the longevity and performance of the heating technology.

5.4 Experimental Tests

A comprehensive experimental testing campaign was undertaken to validate the outcomes predicted by simulation models. In addition to analytical and simulation assessments, the subsequent section will discuss qualitative evaluations for all three heating methods. These factors identified the Imm-H configuration as the most favorable choice for integration within the MGTES system. Consequently, the experimental efforts detailed in this thesis focused primarily on immersion heaters. However, limited testing was also conducted on the other two heater types to verify their technological viability; the results of these tests are summarized in the appendix.

It is essential to clarify that these tests should not be regarded as comprehensive performance evaluations of the MGTES technology but rather as preliminary, partial assessments. The objective of these tests is to yield valuable insights into the performance and behavior of fluidized bed heating technology under controlled conditions. However, they do not constitute a full evaluation of the system. More in-depth and extensive studies are required to fully validate the efficiency, reliability, and long-term performance of the system in real-world operational environments before any definitive conclusions can be drawn.

Accordingly, the initial experimental tests were conducted on a small-scale fluidized bed prototype with an approximate mass of 1 ton, as illustrated in Figure 43.

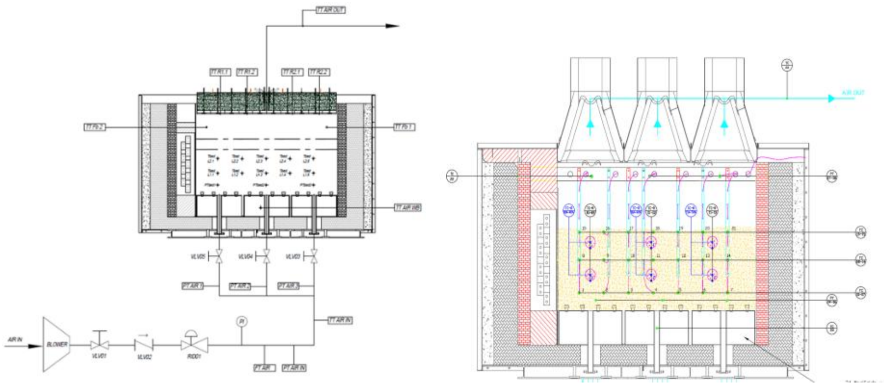

Figure 43 Small-scale test-rig, ~ 1 t

Name	Description
PT AIR	air Pressure sensor and Trasmitter
FT AIR	air Flow meter and Trasmitter
VLVX	Valve nr: X
TT AIR	air Thermocouple
Tbed	bed Thermocouples
TTFb	Free Board Thermocouples
TTRX	Resistor Thermocouple nr: X

Table 9 1 t, small-scale test-rig hardware components

As depicted in schematic, the small-scale prototype of the fluidized bed has a parallelepiped shape and contains approximately 1 ton of silica sand. The sand particles serve as the thermal storage medium, which is fluidized by a series of nozzles located at the bottom of the bed, fed by three air ducts. These ducts are regulated by individual valves, allowing for the direction and modulation of the incoming airflow. The three ducts are supplied by a single pipeline equipped with control valves, pressure reducers, and an inlet compressor. To monitor the fluidization system, an air flow meter, pressure transmitters, and thermocouples are installed (Table 9). A strategically arranged set of thermocouples and pressure sensors is placed within the bed to monitor proper fluidization. The temperature in the freeboard zone is measured, and the temperature of the outgoing air is continuously monitored. Unlike the more comprehensive full-scale system, this simplified setup lacks exhaust air treatment components (such as filters and extractors) as well as inlet treatment (such as an air-to-air heat exchanger). Similarly, the steam heat exchanger is absent, as these tests are specifically focused on evaluating the heat transfer characteristics between the heaters and the fluidized bed.

The main data of the scaled-down test rig are shown in the table. Pictures of the prototype and a screenshot of the process control HMI are shown in the figure.

Name	Value
Sand Mass	1058 kg
Sand bed Height	750 mm
Air Flow Rate Range	1050 ÷ 2400 l/min
Air Pressure	4 bar
Wind box Number	3
Insulating Walls Thickness	480 mm
Ambient Temperature	30 °C
Software	LabView + cDAQ
Thermocouple Type	k
Heater Power	17 kW
PID Regulator Heater nr.	1
Overheating regulator nr	3

Table 10 Main data of the small-scale test-rig in Magaldi's Factory, Buccino (SA), Italy

Figure 44 Pictures of the small-scale test-rig in Magaldi's Factory, Buccino (SA), Italy

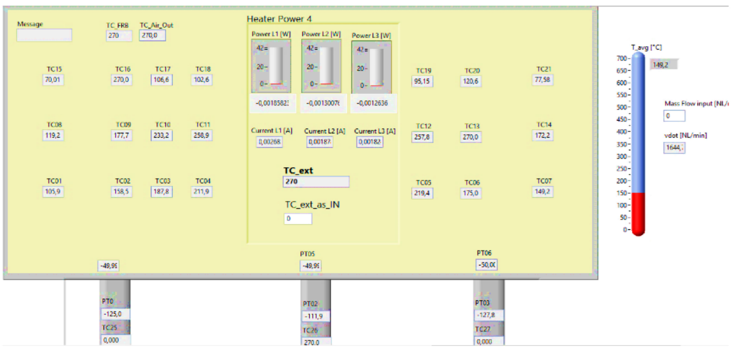

Figure 45 Small-scale test-rig HMI

The experimental tests on the small-scale test rig were conducted not only to identify the optimal type of heat transfer for the fluidized bed and, thereby, the most effective electrical charging system, but also to ensure compatibility with the fluid bed's operational characteristics. Specifically, this test campaign focused on determining the minimum fluidization velocity compatible with the selected charging system. The fluidizing air velocity, which is directly proportional to the air flow rate as described by the equation, plays a critical role in energy efficiency. Optimizing this parameter reduces the energy consumption of the inlet compressor, thus enhancing overall system efficiency. To achieve this, a test protocol was developed, with its flowchart shown in Figure 46

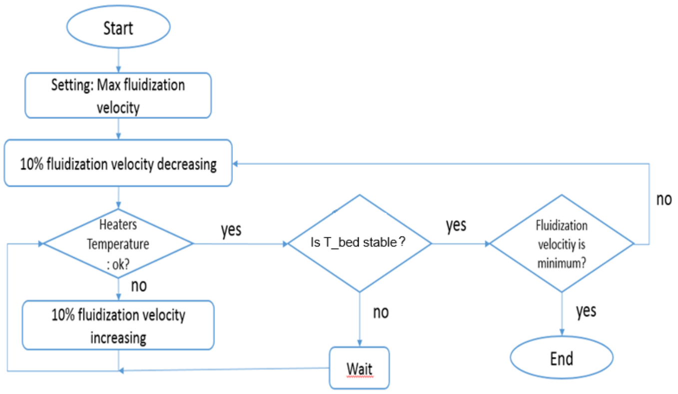

Figure 46 Process Test Protocol

This flowchart describes a control process for adjusting fluidization velocity based on temperature and bed slope conditions in a fluidized bed system. Here's a breakdown of the flow:

1. **Start**: The process begins with setting the maximum fluidization velocity.
2. **10% Fluidization Velocity Decreasing**: The fluidization velocity decreased by 10%.
3. **Check Bed Temperature**:
   - The flow moves to check the bed curve stability.
   - **Yes**: The bed temperature curve is stable; it moves to check another condition.
   - **No**: The bed temperature curve is not stable; the system waits the stabilization.
4. **Check if Fluidization Velocity is Minimum**:
   - **Yes**: If the fluidization velocity has reached the minimum, the process ends.
   - **No**: If not, the system moves to check the heater's temperature.
5. **Heater's Temperature Check**:
   - **No**: If the heater's temperature is not within the acceptable range, the velocity is increased by 10%, and the loop starts again.
   - **Yes**: If the heater's temperature is okay, the process loops back to decrease the velocity by another 10%.

Two main conditions are monitored: the bed temperature curve and heater temperature. Once the velocity reaches a minimum and conditions are satisfied, the process terminates. This process shall be done to different bed temperatures, in fact the following graphs show this process during a ramp up of the bed temperature i.e. a bed charge phase. This flowchart outlines a control system designed to regulate fluidization velocity in response to system parameters, ensuring safe and efficient operation.

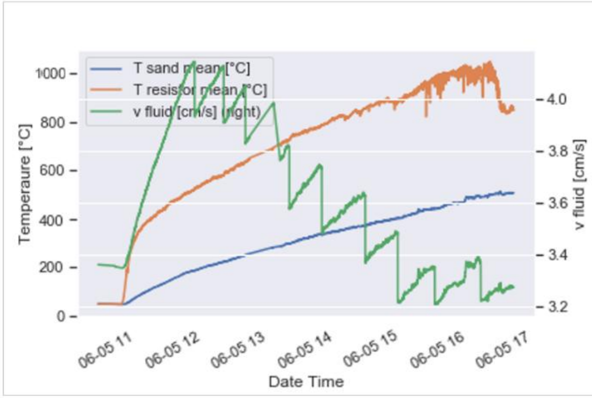

Figure 47 Imm-H experimental tests: bed average temperature, heaters average temperature, air fluidization velocity over time

Figure 47 illustrates the trends of the average temperature of the fluidized bed of sand particles (in blue), the average temperature (in orange) of the resistors comprising the heaters, and the fluidizing air velocity (in green). It can be observed that, over time, both the bed temperature and the resistor temperature increase, indicating a gradual accumulation of thermal energy within the sand bed and therefore a charging phase of the system.

Note that the difference between the temperature of the sand and the temperature of the resistors is significantly higher than expected; this is due to the reduction in fluidization velocity for the purpose of the test. The fluidization velocity values also remain nearly constant, confirming the initial assumptions. It is noteworthy from the experimental results that the fluidization velocity follows a downward trend, as outlined in the test protocol. Additionally, the increase in fluidization velocity within a specific velocity step is observed, which occurs because as the bed temperature rises, the air density decreases, leading to an increase in flow rate, as described by the governing equation.

Figure 48 Imm-H experimental tests: sand bed temperatures at multiple locations over time

The Figure 48 shows the temperature evolution at multiple locations (thermocouples labeled as TC-1A, TC-2A, etc.) within the sand bed. It can be observed that all thermocouples follow a similar trend, indicating that heat is being distributed relatively uniformly, though with slight time delays between different regions. Notably, in the initial phase of the trends, the temperature values are very close to each other, while towards the end of the test, there is a larger gradient, resulting in a spread between the trends. This is due to the fact that the test was conducted by gradually reducing the fluidization velocity over time, leading to a lower degree of fluidization and, consequently, reduced thermal diffusivity.

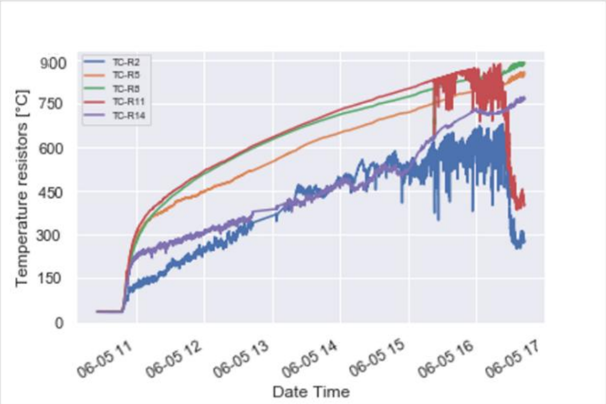

Figure 49 Imm-H experimental tests: heaters resistors temperatures over time

The graph in Figure 49 depicts the temperature evolution of various resistors (TC-R1, TC-R2, etc.).
Although the bed as a whole has a good degree of fluidization to ensure an acceptable heat exchange between the immersed heaters and the sand and, at the same time, between the sand particles, the presence of two trends at a lower temperature indicates a better degree of fluidization in a given area. Comparing the two graphs Figure 48 and Figure 49, it can be seen that the difference between the trends remains approximately constant over time, demonstrating the uniformity of the exchange coefficient between the fluidized bed of sand and the heaters as the sand temperature increases. It should also be noted that the trends of some thermocouples decrease at high temperatures. This phenomenon is not related to a thermodynamic effect but unfortunately to an electromagnetic compatibility problem which makes thermocouples very sensitive above a certain temperature threshold. This problem was solved in subsequent test campaigns by adapting the control system with different types of thermocouples, accompanied by transducers to increase immunity to interference.

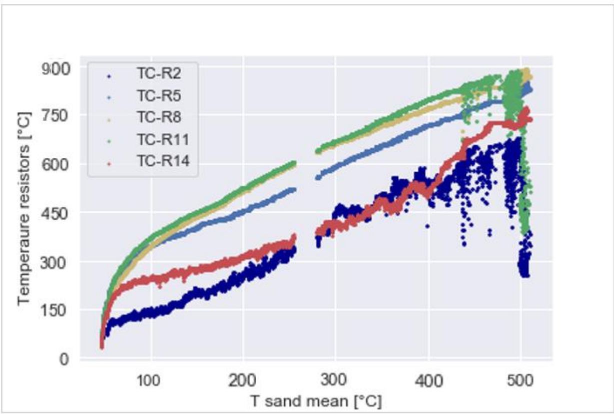

Figure 50 Imm-H heater temperature vs fluidized sand bed

The Figure 50 shows the temperatures recorded by thermocouples on the electric heaters as a function of the fluidized sand bed temperature. Aside from the initial transient, the linear trend follows the convection heat transfer equation$P_{cond}=kA\left(\frac{T_H-T_S}{d}\right)$ (5.3). The slope of the curve is inversely proportional to the convective heat transfer coefficient between the sand and the heaters. A lower slope indicates a higher heat transfer coefficient, which is advantageous as it allows the sand bed to efficiently store energy while keeping the heater temperature relatively low, thus extending their lifespan. Conversely, a steeper slope suggests poor heat exchange, forcing the heaters to operate at higher temperatures and reducing their lifespan.

The stability of the slope suggests a consistent heat transfer coefficient with respect to the sand temperature. A temperature decay in the heaters, at high sand temperature, was observed, which was not due to thermodynamic reasons but rather electromagnetic compatibility issues at high temperatures.

Overall, these results demonstrate the successful operation of the fluidized bed TES system, where the heat transfer between the resistors and the sand bed is well-distributed at approximately 4 cm/s. Although these results are promising, they remain preliminary and partial, intended primarily as an initial assessment of the heating system within the fluidized bed. These tests aim to provide valuable insights into the performance and behavior of fluidized bed heating technology under controlled conditions, but they do not represent a comprehensive evaluation. Further, more detailed investigations will be necessary to fully validate the system’s efficiency, reliability, and long-term performance in real-world operational environments before definitive conclusions can be drawn.

5.4.1 Scaling up strategy

In order to gain a deeper comprehension of the rationale behind this experiment and its contextualization, the Figure 51 illustrates the process of scaling and industrializing the heater system for fluidized beds, specifically for a TES system like MGTES

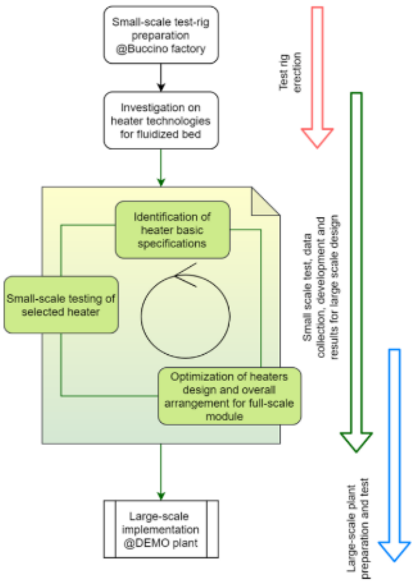

Figure 51 Flowchart of the technology development of MGTES

1. **Small-scale test-rig preparation (@Buccino factory)**: The process begins with the preparation of a small-scale test rig to investigate various heater technologies applicable to fluidized beds. This phase is crucial for gathering initial data and selecting the appropriate heater design.
2. **Investigation on heater technologies for fluidized bed**: At this stage, a thorough investigation is conducted to identify the most suitable heating technologies that meet the performance and operational requirements of the fluidized bed system.
3. **Identification of heater basic specifications**: Based on the investigation results, the basic specifications for the heaters are defined, including parameters like power, size, and operating temperatures.
4. **Small-scale testing of selected heater**: A small-scale version of the heater is tested to validate the performance and ensure it meets the desired specifications in a controlled environment.
5. **Optimization of heater design and overall arrangement for full-scale module**: Following the small-scale testing, the heater design and its integration into the full-scale fluidized bed system are optimized for maximum efficiency, heat transfer, and operational reliability.
6. **Large-scale implementation @DEMO plant**: After final optimization, the heater system is implemented at a large-scale demo plant for real-world testing, which ensures that the system can handle the required load in full-scale applications.

The **red arrow** represents the transition from the preparation of the test rig to the start of testing. The **green arrow** shows the iterative process of small-scale testing and optimization leading towards large-scale application. The **blue arrow** indicates the preparation for large-scale implementation and testing at a demo plant.

In other terms, this flowchart outlines the systematic approach to heater technology development, starting from lab-scale experimentation to full-scale industrial application. The process emphasizes experimental validation, iterative design optimization, and scaling considerations essential for high-efficiency energy storage systems in fluidized beds.

5.5 Heating Technologies Assessment

Traditionally, research in engineering design has focused on quantitative methodologies whose constructs are familiar to engineers. Indeed, in paragraphs 5.3 and 5.4 , quantitative aspects related to objective metrics characterizing the heating system technologies were evaluated. This approach is essential for analyzing and assessing engineering parameters such as performance, operating ranges of components, etc.

However, for a comprehensive analysis that also considers operational factors like installation, maintenance, and replacement, cost-effective, which are crucial for the industrialization of a technology, it is necessary to complement the quantitative analysis with a qualitative evaluation. The qualitative approach allows for a more comprehensive understanding of factors that impact the system’s real-world applicability, usability, and lifecycle [95].

Consequently, a qualitative assessment has been conducted on the Imm-H and Ceil-H configurations. No qualitative assessment was performed for the heating method utilizing heaters along the fluidization line. Both simulations and limited experimental tests indicated significant power derating as sand temperature rises, primarily to prevent resistor overheating. Furthermore, elevated fluidization velocities lead to increased air flow, thereby escalating compressor energy consumption and consequently diminishing the overall system efficiency. In contrast, heating methods employing immersed heaters within the fluidized bed and radiant heaters positioned at the ceiling of the bed have yielded favorable results in both simulations and experimental trials. Below is a preliminary list of qualitative aspects for the evaluation of the two configurations (Imm-H and Ceil-H):

- **Compatibility with the fluidized bed**: Ensures efficient thermal exchange and smooth operation within the fluidized bed system.
- **Compatibility with the storage medium (silica sand)**: Verifies the thermal stability and mechanical interaction between the heating system and silica sand.
- **Ease of installation**: Refers to the simplicity and time efficiency required to set up the heating elements within the system.
- **Ease of maintenance**: Focuses on the system’s maintainability, minimizing downtime and operational costs.
- **Eco-compatibility**: Evaluates the environmental impact, such as emissions and recyclability of materials.

- **Cost per kW**: Economic metric to assess the capital expenditure relative to power output.
- **Potential for in-house manufacturing**: Assesses the feasibility of producing components internally to reduce dependence on external suppliers.
- **Weight**: Affects both structural design considerations and installation procedures.
- **Maximum operating temperature**: Defines the highest operational temperature the system can sustain without degradation.
- **Lifespan**: Refers to the projected operational life of the heating system under normal conditions.
- **Product references**: Demonstrates proven performance in similar applications, ensuring reliability.
- **Application in similar contexts**: Historical deployment in comparable environments for risk mitigation.
- **Availability of raw materials**: Evaluates the ease of providing essential materials for construction.
- **Annual production capacity of components**: Measures the ability to meet demand through manufacturing capabilities.
- **Control and monitoring**: Refers to the system's integration with advanced instrumentation for performance optimization and failure detection.
- **Ease of electrical connection**: Ensures efficient integration into the plant's electrical infrastructure.
- **Thermal exchange efficiency with the bed**: The effectiveness of heat transfer between heating elements and the fluidized bed, crucial for operational efficiency.
- **Space requirements**: Considers the system's footprint relative to available space in the plant.
- **Ease of disposal**: Examines the end-of-life recyclability or environmental considerations for disposal

These characteristics facilitate a qualitative analysis to elucidate key factors critical for strategic technology selection. Specifically, the initial phase of this assessment employs a three-tier scale: low, medium, and high [96] [97]. The following evaluation table systematically classifies and prioritizes these aspects, enabling the identification of relevant technological features and supporting the endorsement of the most suitable option.

Characteristics **• = minimum • • = medium • • • = maximum**	**Imm-heaters**	**Ceil-Imm**
Compatibility with the fluidized bed	• • •	• •
Compatibility with the storage medium (silica sand)	• • •	• •
Ease of installation	• • •	• • •
Ease of maintenance	• •	• • •
Eco-compatibility	• • •	• •
Cost per kW	• •	• •
Potential for in-house manufacturing	• • •	•
Weight	• •	• • •
Maximum operating temperature	• • •	• •
Lifespan	• • •	• •
Product references	• •	• • •

Application in similar contexts	•	•
Availability of raw materials	• • •	• • •
Annual production capacity of components	• • •	• •
Control and monitoring	• • •	• •
Ease of electrical connection	• • •	• • •
Thermal exchange efficiency with the bed	• • •	• •
Space requirements	• • •	• • •
Ease of disposal	• • •	• •

Table 11 Qualitative assessment Imm-heaters and Ceil-Heaters configurations

The Table 11 conducts a comparative evaluation of the two heating methods, providing valuable data to inform the final qualitative analysis. Numerous methodologies can be used to perform the final evaluation, with the SWOT analysis being one of the most prominent. SWOT, an acronym for Strengths, Weaknesses, Opportunities, and Threats, is a strategic tool employed to assess various elements of an organization, project, or technological process. It serves as an effective framework to systematically manage and allocate resources to achieve specific objectives within a defined timeframe [98].

In this context, the SWOT analysis is applied to determine the optimal heating technology for the fluidized bed system, focusing specifically on Imm-h and Ceil-h. The core characteristics of each technology has been gathered and ranked according to their priority in the SWOT matrix. This analysis has been carried out for both heating technologies, ultimately culminating in a final report that identifies the most suitable heating approach based on a synthesis of qualitative and quantitative data.

Strengths	**Weaknesses**
1. Thermal exchange efficiency with the bed 2. Potential for in-house manufacturing 3. Compatibility with the fluidized bed 4. Life span 5. Reliability	1. Low product references and applications in similar context 2. Not easy to maintain
Opportunities	**Threats**
1. Cost reducing thanks to product insourcing	1. The novelty of the solution may lead to unpredictable problems in the long term, despite promising results in the short term.

Table 12 SWOT Analysis for Imm-Heaters

In the context of the SWOT analysis for the Imm-h configuration (Table 12), the key strengths are based on the highly efficient heat exchange mechanism. The immersion of the heaters directly into the fluidized sand bed ensures optimal heat transfer and minimizes heater temperatures, contributing to longer operational lifespans. This direct heat transfer accelerates the thermal energy absorption by the sand, enhancing system performance. Additionally, the ability to construct heater assemblies in-house using globally available raw materials provides scalability, cost efficiency, and control over manufacturing processes.

However, as a novel technology, its long-term reliability remains uncertain due to the absence of extensive real-world application data. Predictive models and simulations, although helpful, are not a substitute for empirical long-term performance data. The innovative nature of the technology means that it might face unforeseen operational challenges over time, which could only become apparent after extended use.

Strengths	**Weaknesses**
1. High referenced product 2. Compatibility with the fluidized bed 3. Ease of installation 4. Ease of maintenance	1. Low applications in similar context 2. Low Compatibility with the silica sand 3. Life span
Opportunities	**Threats**
1. Reducing cost thanks to the procurement product ease	1. Incompatibility of the technology with silica sand can lead to deterioration of the heater

Table 13 SWOT Analysis for Ceil-Heaters

The SWOT analysis for the Ceil-H (Table 13) configuration highlights the system's maturity, as it has been successfully used in other applications, though not in fluidized beds. It exhibits good compatibility with the fluidized bed, largely because its operation does not directly interfere with the bed's dynamics. In this configuration, radiant panels are mounted under the ceiling of the vessel, simplifying both installation and maintenance. However, since the heaters are not in direct contact with the bed, they rely on radiant heat transfer, resulting in higher operating temperatures. This causes the resistors to experience faster material degradation, which is further exacerbated by dust accumulation (elutriate) on the resistors surface from the fluidized bed, settling in the freeboard region. The dust layer negatively impacts thermal exchange, leading to an even greater rise in the heaters' operational temperatures and a reduction in their lifespan.

In contrast to immersion heaters, where heat is transferred more efficiently through direct contact with the fluidized medium, this indirect heating configuration, while offering simplified maintenance, introduces thermal inefficiencies and longevity concerns at some operating temperatures of the system. Nonetheless, its proven track record in other applications makes it a viable option at lower temperatures, with potential operational trade-offs to be carefully considered during the decision-making process for fluidized bed heating.

In conclusion, taking into account both the quantitative and qualitative analyses, it has been determined that, although both heating technologies provide adequate performance, the immersion heating system (Imm-H) is the more advantageous choice for the scale-up of the industrial prototype. The decision is driven by its superior thermal efficiency, enhanced heat transfer between the sand and heaters, and cost-effectiveness. The next step involves adapting the system to a larger fluidized bed, requiring careful recalibration of the heating power to ensure consistent performance at the increased scale.

Conclusions

This doctoral thesis investigates thermal energy storage charge systems designed to provide steam for industrial applications. Specifically, it presents two types of storage technologies based on fluidized sand beds: one that is charged directly by solar energy and another by electrical energy. The two systems were developed and patented by Magaldi Power S.p.A., under the names STEM® and MGTES, respectively.

Key results on STEM®

For the STEM® technology, which utilizes solar energy for charging, two innovative features are highlighted. The first is an advanced algorithm for integral correction of heliostat (solar tracking mirrors) pointing errors integrated into heliostat control system MHC. This algorithm enhances pointing accuracy, thereby increasing the amount of solar energy directed to and captured within the fluidized bed. The second innovation is the deployment of a biaxial inclinometer on each heliostat, which mitigates pointing errors due to ground misalignments, thereby enhancing system reliability. The 12’000 hours of operational data collected from the first industrial-scale STEM® plant in Sicily (Figure 32) have validated the system's quality and reliability. The findings demonstrate that the implemented novel integral correction algorithm, in conjunction with the use of inclinometers, enhances tracking precision, achieving performance levels comparable to state-of-the-art solar tracking systems. Figure 52 shows the daily RMS pointing error values, highlighting the 4 control models with different colors.

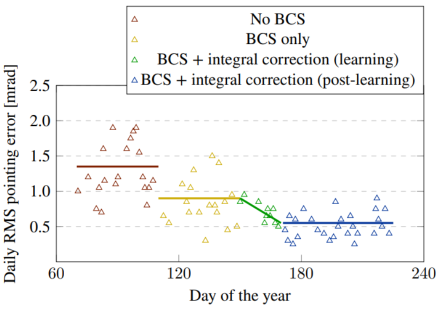

Figure 52 Daily RMS pointing error trend along 5 months, showing the effect of BCS and integral error correction system

BCS	Integral Correction	Pointing error [mrad] RMS	Std dev
No	No	1.39	0.86
Yes	No	0.95	0.52
Yes	Learning	0.74	0.21
Yes	Post-Learning	**0.52**	0.38

Table 14 Global pointing error statistics for 5 months, using different control types

The heliostats were operated without BCS for the first 40 days (red), then for more 40 days with BCS without the integral error correction system (yellow), reducing the global aiming error by about 32%. Finally, the activation of the integral correction system reduced the errors by a further 45%, with an initial “learning” period of 20 days. In addition, the system maintained its low global pointing error, despite windy and rainy days which might have caused heliostats misalignment, prevented by MHC, thus confirming the quality and reliability of the developed system.

Reference Document	Pointing error [mrad]	Value Type
Harper et al. [89]	1.0	declared
Zavoico [90]	1.0	declared
Berenguel et al. [91]	0.9	calculated
Strachan and Houser [92]	0.61	calculated
Sattler et al. [88]	0.1	estimated

Table 15 Global pointing error comparison with similar heliostat control systems in the scientific literature. Berenguel et al. value has been calculated by transforming the error from cm to mrad considering an heliostat at an average distance from the target of 100 m. Strachan and Houser pointing error has been calculated by using the Euclidean distance from the azimuth and elevation components

As shown in bold in the last row of Table 14, after the learning phase, the system showed a global pointing RMS error of 0.52 mrad. This value is close to the lower bound of the range 0.1 ÷ 1 mrad, reported in Table 15, summarizing global errors from different scientific documents describing similar heliostat control systems. For [91] and [92], the value of the global pointing error was not explicit, so a calculation was necessary. Further research activities are planned with the objective of further reducing the pointing error. The focus of these activities will be on the contributions of error sources due to motion implementation.

Key results on MGTES

For the MGTES technology, which employs electric resistances (heaters) for thermal charging through Joule heating, a comprehensive study was conducted to identify the most suitable heating method for the fluidized sand bed. Analytical models were used to simulate different configurations (Figure 53), comparing resistive elements designed to heat by conduction, convection, and radiation.

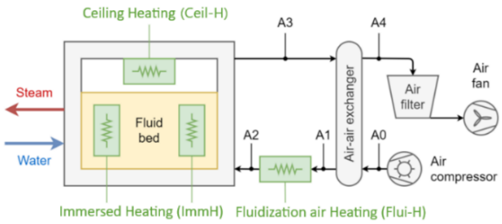

Figure 53 Main MGTES components with different modes for charging: convective, radiating, and fluidization air heating

In the analytical simulations, a fluidized bed system with a sand mass of 36 tons was considered, along with a heating power input of approximately 370 kW. The target nominal parameters included a sand temperature of 600°C and a fluidization velocity of 4 cm/s. To validate the simulation outcomes, an experimental test campaign was conducted on a small-scale prototype. Due to the less favourable performance observed in the analytical results of Flui-H configuration compared to the other two heating methods, the testing phase was exclusively focused on the Imm-H and Ceil-H configurations.

	Analytical Results			Experimental Results	
	Imm-H	Ceil-H	Flui-H	Imm-H	Ceil-H
Charging Time [h]	8.41	8.89	74	8.8	9
Fluidization Velocity [cm/s]	4.05	4.05	13	4.3	4.02
Δ_{Heater_Sand}	152	263	-	255	361

Table 16 Analytical and Experimental Results Comparison

A comprehensive comparison is provided in tabular format (Table 16). The experimental results generally align with the analytical predictions, except for the temperature differential between the heaters and sand, which exceeds ~100 °C in both configurations. Overall, the Imm-H and Ceil-H configurations exhibit comparable performance. However, to identify the most promising heating method, a qualitative analysis was performed alongside the quantitative assessment, aimed at evaluating critical factors relevant to the industrialization of the technology. Key considerations included ease of installation, maintenance requirements, component replaceability, cost-effective, and compatibility of the technology with the storage medium.

A SWOT analysis was conducted to assess these factors, with the resulting matrices presented below for both configurations.

Strengths	Weaknesses
1. Thermal exchange efficiency with the bed 2. Potential for in-house manufacturing 3. Compatibility with the fluidized bed 4. Life span 5. Reliability	1. Low product references and applications in similar context 2. Not easy to maintain
Opportunities	**Threats**
1. Cost reducing thanks to product insourcing	1. The novelty of the solution may lead to unpredictable problems in the long term, despite promising results in the short term.

Strengths	Weaknesses
1. High referenced product 2. Compatibility with the fluidized bed 3. Ease of installation 4. Ease of maintenance	1. Low applications in similar context 2. Low Compatibility with the silica sand 3. Life span
Opportunities	**Threats**
1. Reducing cost thanks to the procurement product ease	1. Incompatibility of the technology with silica sand can lead to deterioration of the heater

Figure 54 SWOT Analysis Matrices for Imm-H and Ceil-H configuration respectively on the left and on the right

The SWOT analysis suggests that qualitative factors play a more significant role in favoring the Imm-H technology, identifying it as the most promising heating configuration. Further testing on larger-scale prototypes is planned to validate these findings and confirm their suitability for industrial application.

Bibliography

[1] United Nations 1992, United Nations Framework Convention On Climate Change, FCCC/INFORMAL/84 GE.05-62220 (E) 20070

[2] IEA, World energy Outlook 2023

[3] International Energy Agency (IEA), Net Zero by 2050 - A Roadmap for the Global Energy Sector

[4] https://www.iea.org/data-and-statistics/charts/global-co2-emissions-by-sector-2019-2022

[5] https://unfccc.int/about-us/about-the-secretariat

[6] Intergovernmental Panel on Climate Change (IPCC), “Climate Change 2023” Synthesis Report

[7] Net Zero Emissions by 2050 Scenario (NZE) – Global Energy and Climate Model – Analysis - IEA

[8] IRENA, Global Energy Transformation: A Roadmap to 2050, 2018, https://doi.org/10.1057/9780230244092. Abu Dhabi

[9] S. Rehman, L.M. Al-Hadhrami, M.M. Alam, Pumped hydro energy storage system: a technological review, Renew. Sustain. Energy Rev. 44 (2015) 586–598, https://doi.org/10.1016/J.RSER.2014.12.040.

[10] M. Budt, D. Wolf, R. Span, J. Yan, A review on compressed air energy storage: basic principles, past milestones and recent developments, Appl. Energy 170 (2016) 250–268, https://doi.org/10.1016/J.APENERGY.2016.02.108.

[11] C.S. Lai, M.D. McCulloch, Levelized cost of electricity for solar photovoltaic and electrical energy storage, Appl. Energy 190 (2017) 191–203, https://doi.org/ 10.1016/J.APENERGY.2016.12.153

[12] K. Mongird, V. Fotedar, V. Viswanathan, V. Koritarov, P. Balducci, B. Hadjerioua, et al., in: Energy Storage Technology And Cost Characterization Report, Pacific Northwest Natl Lab, 2019, pp. 1–120.

[13] Long Duration Energy Storage Council, “Driving to Net Zero Industry Through Long Duration Energy Storage”, November 2023

[14] IEA, “World Energy Investment 2024”

[15] REN21, “Renewable 2024 - Global Status report”

[16] International Renewable Energy Agency (IRENA), “Renewable energy highlights”, 11 July 2024

[17] IRENA, “World Energy Transitions Outlook 2024”, https://www.irena.org/Digital-Report/World-Energy-Transitions-Outlook-2023#page-0

[18] Womble Bond Dickinson, “Energy Transition Outlook Survey Report”, November 2023, https://info.womblebonddickinson.com/energy-report-2024-pdf

[19] IEA, “Renewable Energy for Industry”, Insight series 2017

[20] IEA, “”Renewables 2023, Analysis and forecast to 2028”

[21] C2ES Climate Innovation 2050, “Clean Heat Pathways For Industrial Decarbonization”, August 2021

[22] International Solar Alliance, Long Duration Energy Storage Council “Solar And Ldes: Critical Partners To Ensure 24/7 Reliable Renewable Energy”

[23] Laura Pompei, Fabio Nardecchia, Fabio Bisegna. A review on thermal energy storage. Dept. of Astronautical Electrical and Energy Engineering

[24] A. Hauer. Storage Technology Issues and Opportunities, Committee on Energy Research and

Technology (International Energy Agency), International Low-Carbon Energy Technology Platform, Strategic and Cross- Cutting Workshop “Energy Storage – Issues and Opportunities”, 15 February 2011, Paris. France.

[25] L.F. Cabeza, E. Galindo, C. Prieto, C. Barreneche, A.I. Fernandez, Key performance indicators in thermal energy storage: Survey and assessment, Renewable Energy 83 (2015) 820-827

[26] Lane GA. Solar heat storage: latent heat materials. Technology, vol. 2. Boca Raton, USA: CRC Press; 1985

[27] Kinga Pielichowska, Krzysztof Pielichowski, Phase change materials for thermal energy storage, Progress in Materials Science, Volume 65, 2014, Pages 67-123, ISSN 0079-6425, https://doi.org/10.1016/j.pmatsci.2014.03.005.

[28] S.D. Sharma, H. Kitano, K. Sagara, “Phase change materials for low temperature solar thermal applications”, Res.Rep. Fac. Eng. Mie Univ., 29 (2004), pp 31-64.

[29] Ming Liu, Wasim Saman, Frank Bruno. Review on storage materials and thermal performance enhancement techniques for high temperature phase change thermal storage systems. Renewable and Sustainable Energy Reviews, Volume 16, Issue 4, 2012, Pages 2118-2132, ISSN 1364-0321, https://doi.org/10.1016/j.rser.2012.01.020.

[30] Yate Ding and S.B. Riffat. Thermochemical energy storage technologies for building applications: a state-of-the-art review. Department of Architecture and Built Environment, Institute of Sustainable Energy Technologies, University of Nottingham, Nottingham NG7 2RD, UK

[31] Yate Ding and S.B. Riffat. Thermochemical energy storage technologies for building applications: a state-of-the-art review. Department of Architecture and Built Environment, Institute of Sustainable Energy Technologies, University of Nottingham, Nottingham NG7 2RD, UK.

[32] Edem N’Tsoukpoe K, Liu H, Le Pierre’s N, et al. A review on long-term sorption solar energy storage. Renew Sustain Energy Rev 2009;13:2385 –96.

[33] Bales Chris. Thermal Properties of Materials for Thermo-chemical Storage of Solar Heat. Solar Heating and Cooling Programme. International Energy Agency, 2005

[34] Aveyard R, Haydon DA. An Introduction to the Principles of Surface Chemistry. CUP Archive, 197

[35] Kato Y. Chemical energy conversion technologies for efficient energy use. In: Paksoy H (ed.) Thermal Energy Storage for Sustainable Energy Consumption. Springer, 2007, 377 –91.

[36] Abedin AH. Thermochemical energy storage systems: modelling, analysis and design. Master’s Thesis. University of Ontario, Institute of Technology 2010.

[37] Darkwa K, Ianakiev A, O’Callaghan PW. Modelling and simulation of adsorption process in a fluidised bed thermochemical energy reactor. Appl Therm Eng 2006;26:838–45

[38] K. Vignarooban, Xinhai Xu, A. Arvay, K. Hsu, A.M. Kannan. Heat transfer fluids for concentrating solar power systems – A review. Applied Energy, Volume 146, 2015, Pages 383-396, ISSN 0306-2619, https://doi.org/10.1016/j.apenergy.2015.01.125.

[39] Lukas Heller, Literature Review on Heat Transfer Fluids and Thermal Energy Storage Systems in CSP Plants, STERG Report, Solar Thermal Energy Research Group, Stellenbosch University, 2013

[40] https://e-llo.fr/en/thermodynamic-solar-power-plant/technology/

[41] Thomas Bauer, Nicole Pfleger, Nils Breidenbach, Markus Eck, Doerte Laing, Stefanie Kaesche, Material aspects of Solar Salt for sensible heat storage, Applied Energy, Volume 111, 2013, Pages

1114-1119, ISSN 0306-2619, https://doi.org/10.1016/j.apenergy.2013.04.072
[42] Hatem Ahmad Aljaerani, M. Samykano, A.K. Pandey, K. Kadirgama, R. Saidur, Thermo-physical properties and corrosivity improvement of molten salts by use of nanoparticles for concentrated solar power applications: A critical review, Journal of Molecular Liquids, Volume 314, 2020, 113807, ISSN 0167-7322, https://doi.org/10.1016/j.molliq.2020.113807
[43] Kuravi Sarada, Trahan Jamie, Goswami D Yogi, Rahman Muhammad M, Elias, Stefanakos K., Thermal energy storage technologies and systems for concentrating solar power plants. Prog Energy Combust Sci 2013;39(4):285–319
[44] https://www.frontiersin.org/journals/energy-research/articles/10.3389/fenrg.2022.809663/full
[45] Alexander Bonk, Salvatore Sau, Nerea Uranga, Marta Hernaiz, Thomas Bauer, Advanced heat transfer fluids for direct molten salt line-focusing CSP plants, Progress in Energy and Combustion Science, Volume 67, 2018, Pages 69-87, ISSN 0360-1285, https://doi.org/10.1016/j.pecs.2018.02.002
[46] Paul Gauché, Justine Rudman, Mbalenhle Mabaso, Willem A. Landman, Theodor W. von Backström, Alan C. Brent, System value and progress of CSP, Solar Energy, Volume 152, 2017, Pages 106-139, ISSN 0038-092X, https://doi.org/10.1016/j.solener.2017.03.072.
[47] Lina Ma, Cancan Zhang, Yuting Wu, Yuanwei Lu, Comparative review of different influence factors on molten salt corrosion characteristics for thermal energy storage, Solar Energy Materials and Solar Cells, Volume 235, 2022, 111485, ISSN 0927-0248, https://doi.org/10.1016/j.solmat.2021.111485
[48] V.M.B. Nunes, C.S. Queirós, M.J.V. Lourenço, F.J.V. Santos, C.A. Nieto de Castro, Molten salts as engineering fluids – A review: Part I. Molten alkali nitrates, Applied Energy, Volume 183, 2016, Pages 603-611, ISSN 0306-2619, https://doi.org/10.1016/j.apenergy.2016.09.003.
[49] W.D. Steinmann, "Thermal energy storage systems for concentrating solar power (CSP) technology," Woodhead Publishing Series in Energy, Advances in Thermal Energy Storage Systems, Woodhead Publishing, 2015, Pages 511-531, ISBN 9781782420880, https://doi.org/10.1533/9781782420965.4.511
[50] Mohamed Tawfik, "A review of directly irradiated solid particle receivers: Technologies and influencing parameters," Renewable and Sustainable Energy Reviews, Volume 167, 2022, 112682, ISSN 1364- 0321, https://doi.org/10.1016/j.rser.2022.112682
[51] Khadija El Alami, Mohamed Asbik, Hassan Agalit. Identification of natural rocks as storage materials in thermal energy storage (TES) system of concentrated solar power (CSP) plants – A review. Solar Energy Materials and Solar Cells, Volume 217, 2020, 110599, ISSN 0927-0248, https://doi.org/10.1016/j.solmat.2020.110599.
[52] R. Tiskatine, R. Oaddi, R. Ait El Cadi, A. Bazgaou, L. Bouirden, A. Aharoune, A. Ihlal, Suitability and characteristics of rocks for sensible heat storage in CSP plants, Solar Energy Materials and Solar Cells, Volume 169, 2017, Pages 245-257, ISSN 0927-0248, https://doi.org/10.1016/j.solmat.2017.05.033
[53] Harmeet Singh, R.P. Saini, J.S. Saini, A review on packed bed solar energy storage systems, Renewable and Sustainable Energy Reviews, Volume 14, Issue 3, 2010, Pages 1059-1069, ISSN 1364-0321, https://doi.org/10.1016/j.rser.2009.10.022.
[54] Aubin Touzo, Régis Olives, Guilhem Dejean, Doan Pham Minh, Mouna El Hafi, Jean-François Hoffmann, Xavier Py, Experimental and numerical analysis of a packed-bed thermal energy storage

system designed to recover high temperature waste heat: an industrial scale up, Journal of Energy Storage, Volume 32, 2020, 101894, ISSN 2352- 152X, https://doi.org/10.1016/j.est.2020.101894.

[55] Silvia Trevisan, Rafael Guedez, Design optimization of an innovative layered radial-flow high-temperature packed bed thermal energy storage, Journal of Energy Storage, Volume 83, 2024, 110767, ISSN 2352-152X, https://doi.org/10.1016/j.est.2024.110767

[56] J.Pascal Coutier, E.A. Farber, Two applications of a numerical approach of heat transfer process within rock beds, Solar Energy, Volume 29, Issue 6, 1982, Pages 451-462, ISSN 0038-092X, https://doi.org/10.1016/0038-092X(82)90053-6.

[57] Sampson Tetteh, Gabriel Juul, Mika Järvinen, Annukka Santasalo-Aarnio, Improved effective thermal conductivity of sand bed in thermal energy storage systems, Journal of Energy Storage, Volume 86, Part B, 2024, 111350, ISSN 2352-152X, https://doi.org/10.1016/j.est.2024.111350

[58] Jiang K., Du X., Kong Y., Xu C., Ju X., A comprehensive review on solid particle receivers of concentrated solar power (2019) Renewable and Sustainable Energy Reviews, 116, art. no. 109463, Cited 55 times. DOI: 10.1016/j.rser.2019.109463

[59] Bellan S., Kodama T., Gokon N., Matsubara K., A review on high temperature thermochemical heat storage: Particle reactors and materials based on solid–gas reactions (2022) wiley Interdisciplinary Reviews: Energy and Environment, 11 (5), art. no. e440. DOI: 10.1002/wene.440

[60] C. Ho, J. Christian, D. Gill, A. Moya, S. Jeter, S. Abdel-Khalik, D. Sadowski, N. Siegel, H. Al-Ansary, L. Amsbeck, B. Gobereit, R. Buck, Technology Advancements for Next Generation Falling Particle Receivers, Energy Procedia, Volume 49, 2014, Pages 398-407, ISSN 1876-6102, https://doi.org/10.1016/j.egypro.2014.03.043.

[61] Tregambi C., Troiano M., Montagnaro F., Solimene R., Salatino P., Fluidized Beds for Concentrated Solar Thermal Technologies—A Review (2021) Frontiers in Energy Research, 9, art. no. 618421, Cited 24 times. DOI: 10.3389/fenrg.2021.618421

[62] Al-Ansary H, El-Leathy A, Jeter S, Djajadiwinata E, Alaqel S, Golob M, Nguyen C, Saad R, Shafiq T, Danish S, Abdel-Khalik S, Al-Suhaibani Z, Abu-Shikhah N, Haq MI, Al-Balawi A, Al-Harthi F. On-sun experiments on a particle heating receiver with red sand as the working medium. AIP Conf Proc 2018;2033:040002.

[63] Lee T, Lim S, Shin S, Sadowski DL, Abdel-Khalik SI, Jeter SM, Al-Ansary H. Numerical simulation of particulate flow in interconnected porous media for central particle-heating receiver applications. Sol Energy 2015;113:14–24.

[64] E. Alonso, A. Gallo, M.I. Roldán, C.A. Pérez-Rábago, E. Fuentealba, "Use of rotary kilns for solar thermal applications: Review of developed studies and analysis of their potential," Solar Energy, Volume 144, 2017, Pages 90-104, ISSN 0038-092X, https://doi.org/10.1016/j.solener.2017.01.004

[65] Wu W, Amsbeck L, Buck R, Uhlig R, Ritz-Paal R. Proof of concept test of a centrifugal particle receiver. Energy Proc 2014;49:560–8.

[66] C. Tregambi, R. Chirone, F. Montagnaro, P. Salatino, R. Solimene, Heat transfer in directly irradiated fluidized beds, Solar Energy, Volume 129, 2016, Pages 85-100, ISSN 0038-092X, https://doi.org/10.1016/j.solener.2016.01.057

[67] G. Xiao, K. Guo, Z. Luo, M. Ni, Y. Zhang, C. Wang, "Simulation and experimental study on a spiral solid particle solar receiver," Applied Energy, Volume 113, 2014, Pages 178-188, ISSN 0306-2619, https://doi.org/10.1016/j.apenergy.2013.06.045

[68] C. Tregambi, C. Bevilacqua, M. Troiano, R. Solimene, P. Salatino, “A novel autothermal fluidized bed reactor for concentrated solar thermal applications,” Chemical Engineering Journal, Volume 398, 2020, Issue 125702, ISSN 1385-8947, https://doi.org/10.1016/j.cej.2020.125702

[69] Zhang H, Benoit H, Gauthier D, Degreve J, Baeyens J, Lopez IP, Hemati M, Flamant G. Particle circulation loops in solar energy capture and storage: gassolid flow and heat transfer considerations. Appl Energy 2016;161:206–24

[70] A. Vecchi, K. Knobloch, T. Liang, H. Kildahl, A. Sciacovelli, K. Engelbrecht, Y. Li, Y. Ding, “Carnot Battery development: A review on system performance, applications and commercial state-of-the-art”, Journal of Energy Storage, Volume 55, Part D, 2022, 105782, ISSN 2352-152X, https://doi.org/10.1016/j.est.2022.105782.

[71] M. King, A. Jain, R. Bhakar, J. Mathur, J. Wang, Overview of current compressed air energy storage projects and analysis of the potential underground storage capacity in India and the UK, Renew. Sustain. Energy Rev. 139 (2021), 110705, https://doi.org/10.1016/J.RSER.2021.110705.

[72] Z. Song, J. Li, X. Han, L. Xu, L. Lu, M. Ouyang, et al., Multi-objective optimization of a semi-active battery/supercapacitor energy storage system for electric vehicles, Appl. Energy 135 (2014) 212–224, https://doi.org/10.1016/J.APENERGY.2014.06.087.

[73] https://www.magaldi.com/it/magaldi-green-energy-srl

[74] https://www.magaldi.com/it/applicazioni/mgtes-magaldi-green-thermal-energy-storage

[75] Moghtada Mobedi , Gamze Gediz Ilis. Fundamentals of Heat Transfer. Springer. Prabir Basu, Chapter 6 - Design of Biomass Gasifiers, Editor(s): Prabir Basu, Biomass Gasification and Pyrolysis, Academic Press, 2010, Pages 167-228, ISBN 9780123749888, https://doi.org/10.1016/B978-0-12-374988-8.00006-4. (https://www.sciencedirect.com/science/article/pii/B9780123749888000064)

[76] Romano Acri, Fulvio Bassetti, Maria Carmen Falvo, Letizia Magaldi, Matteo Manganelli, Lorenzo Romagnoli, Federico Santi, and Antonio Scafuri. A new thermal energy storage technology for power system services. In 2021 IEEE International Conference on Environment and Electrical Engineering and 2021 IEEE Industrial and Commercial Power Systems Europe (EEEIC / I&CPS Europe), pages 1–6, 2021. doi: 10.1109/EEEIC/ICPSEurope51590.2021. 9584535.

[77] Claudio Tregambi, Carla Bevilacqua, Antonio Cammarota, Riccardo Chirone, Piero Salatino, Roberto Solimene, Fulvio Bassetti, Antonio Picarelli, Mario Magaldi; ”Experimental characterization of granular materials for directly irradiated fluidized bed solar receivers” AIP Conf. Proc. 25 July 2019; 2126 (1): 030060. https://doi.org/10.1063/1.5117572

[78] Vant-Hull. L., ”Issues with beam-down concepts”, SolarPACES 2013, Energy Procedia, vol. 49, pp. 257-2

[79] Mutuberria A., Sánchez M., Testani C., Fernandez J., Rinaldi A., Moya E. Z., ”Challenges and handicaps on the design of an efficient beam-down system at an existing heliostat field layout”, 2020 IEEE International Conference on Environment and Electrical Engineering and 2020 IEEE Industrial and Commercial Power Systems Europe (EEEIC / I&CPS Europe), 2020, pp. 1-4.

[80] Tregambi C., Troiano M., Montagnaro F., Solimene R., Salatino P., Fluidized Beds for Concentrated Solar Thermal Technologies—A Review (2021) Frontiers in Energy Research, 9, art. no. 618421, Cited 24 times. DOI: 10.3389/fenrg.2021.618421

[81] C. Tregambi, R. Chirone, F. Montagnaro, P. Salatino, R. Solimene, Heat transfer in directly irradiated fluidized beds, Solar Energy, Volume 129, 2016, Pages 85-100, ISSN 0038-092X,

https://doi.org/10.1016/j.solener.2016.01.057
[82] Blanco M.J., Kypros M., Bonanos A.M., ”Updating the PSA sun position algorithm”, Solar Energy 212, pp. 339- 341, 2020, DOI: 10.1016/j.solener.2020.10.084.
[83] Reda I., Andreas A., ”Solar Position Algorithm for Solar Radiation Applications”, National Renewable Energy Laboratory (NREL), 2008, NREL/TP-560-34302.
[84] Siciliano B., Sciavicco L., Villani L., Oriolo G., ”Robotics Modelling, Planning and Control”, Springer, 2000.
[85] Marc Röger, Kristina Blume, Tim Schlichting, et al. , ”Status update of the SolarPACES heliostat testing activities”, AIP Conference Proceedings 2445, 2022, doi: 10.1063/5.0087037
[86] Röger M., ”Heliostat Performance Testing Guideline”, 2017 SolarPACES Task III Meeting, Santiago de Chile
[87] Abraham Kribus, Irina Vishnevetsky, Amnon Yogev, Tatiana Rubinov, ”Closed loop control of heliostats”, Energy, Volume 29, Issues 5–6, 2004, Pages 905- 913, ISSN 0360-5442, https://doi.org/10.1016/S0360- 5442(03)00195-6.
[88] Sattler J.C., Röger M., Schwarzbözl P., Buck R., Macke A., Raeder C., Göttsche J., ”Review of heliostat calibration and tracking control methods”, Solar Energy, vol. 207, pp. 110-132, 2020, ISSN 0038-092X, https://doi.org/10.1016/j.solener.2020.06.030
[89] Harper P.J., Dreijer J., Malan K., Larmuth J., Gauche P., ”Use of MEMs and optical sensors for closed loop heliostat control”, AIP Conference Proceedings, 2016.
[90] Sandia National Laboratories, Alexis B. Zavoico, ”Solar Power Tower Design Basis Document” SAND2001-2100
[91] Berenguel M., Rubio F.R., Valverde A., Lara P.J., Arahal M.R., Camacho E.F., López M., ”An artificial visionbased control system for automatic heliostat positioning offset correction in a central receiver solar power plant”, Solar Energy, vol. 76, Issue 5, pp. 563-575, 2004.
[92] Sandia Laboratories, SAND92-1381-UC-235, John W. Strachan and Richard M. Houser, ”Testing and Evaluation of Large-Area Heliostats for Solar Thermal Applications”
[93] Theodore L. Bergman, Adrienne S. Lavine, Frank P. Incropera, David P. DeWitt. Fundamentals of Heat and Mass Transfer. Seventh Edition, Wiley.
[94] Daizo Kunii, Octave Levenspiel. Fluidization Engineering. Butterworth – Heinemann
[95] Shanna Daly, Anna Mcgowan, Panos Papalambros. Using Qualitative Research Methods In Engineering Design Research. International Conference On Engineering Design, Iced13 19-22 August 2013, Sungkyunkwan University, Seoul, Korea.
[96] C R, Sharath Kumar & K.B, Praveena. (2023). SWOT ANALYSIS. International Journal of Advanced Research. 11. 744-748. 10.21474/IJAR01/17584.
[97] Ministero degli affari esteri e della cooperazione internazionale. 3.1 Tipi di Valutazione. https://www.esteri.it/mae/doc/6_40_176_e.pdf
[98] Gürel, Emet. (2017). SWOT ANALYSIS: A THEORETICAL REVIEW. Journal of International Social Research. 10. 994-1006. 10.17719/jisr.2017.1832.
[99] S. Ahmad, M. Shafiullah, C. B. Ahmed, M. Alowaifeer, A Review of Microgrid Energy Management and Control Strategies (2023). doi:10.1109/ACCESS.2023.3248511.
[100] M. Thirunavukkarasu, Y. Sawle, H. Lala, A comprehensive review on optimization of hybrid renewable energy systems using various optimization techniques (4 2023).

doi:10.1016/j.rser.2023.113192
[101] H. A. Muqeet, H. Javed, M. N. Akhter, M. Shahzad, H. M. Munir, M. U. Nadeem, S. S. H. Bukhari, M. Huba, Sustainable Solutions for Advanced Energy Management System of Campus Microgrids: Model Opportunities and Future Challenges (3 2022). doi:10.3390/s22062345.
[102] M. F. Zia, E. Elbouchikhi, M. Benbouzid, Microgrids energy management systems: A critical review on methods, solutions, and prospects (7 2018). doi:10.1016/j.apenergy.2018.04.103.
[103] M. N. Naz, M. I. Mushtaq, M. Naeem, M. Iqbal, M. W. Altaf, M. Haneef, Multicriteria decision making for resource management in renewable energy assisted microgrids (2017). doi:10.1016/j.rser.2016.12.059
[104] A. Cabrera-Tobar, A. Massi Pavan, G. Petrone, G. Spagnuolo, A Review of the Optimization and Control Techniques in the Presence of Uncertainties for the Energy Management of Microgrids (12 2022). doi:10.3390/en15239114
[105] K. Gao, T. Wang, C. Han, J. Xie, Y. Ma, R. Peng, A review of optimization of microgrid operation, Energies 14 (10) (5 2021). doi:10.3390/en14102842
[106] X. Zhong, W. Zhong, Y. Liu, C. Yang, S. Xie, Optimal energy management for multi-energy multi-microgrid networks considering carbon emission limitations, Energy 246 (5 2022). doi:10.1016/j.energy.2022.123428.
[107] Paolo D'Angelo, Antonio Scafuri, Walter Zamboni. Modeling, optimization and management strategies for a microgrid with integrated thermal energy storage. ELECTRIMACS 2024 – Castello de la Plana, Spain, 27-30 May 2024.
[108] Magaldi M., Carrea A., 2017. Dispositivo, impianto e metodo per l'accumulo e lo scambio di energia termica di origine solare, IT201700050467A1.
[109] Magaldi M., 2013, System of secondary reflectors with high level of efficiency for storage and use of energy from a solar source, US10156383B2.
[110] Magaldi M., De Michele M., Salatino P., 2010. Device and method for storage and transfer of thermal energy originated from solar radiation based on fluidization of a bed of particles, US8960182B2.
[111] Magaldi M., Bassetti F., 2020, Device for the storage of thermal energy of solar origin based upon multiple reflections, WO2021156649A1.
[112] Magaldi M., Bassetti F., 2020. Fluidized bed heat exchanger and process, ES2984079T3.
[113] Magaldi M., Bassetti F., 2019. Plant and method for accumulation of energy in thermal form, AU2019412536A1.

Appendix A
Magaldi Heliostat Control

In this section some screenshots of the principal MHC HMI with relative code written G Language on the Labview platform of National Instruments company. Additionally, is reported the libraries organization and the relative hierarchy of a system control software section.

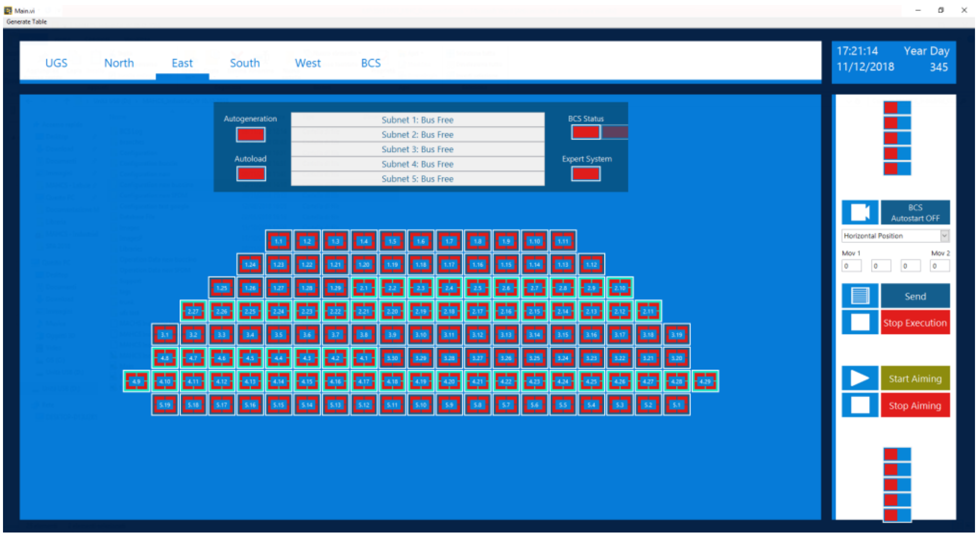

Figure 55 Human Machine Interface Magaldi Heliostat Control

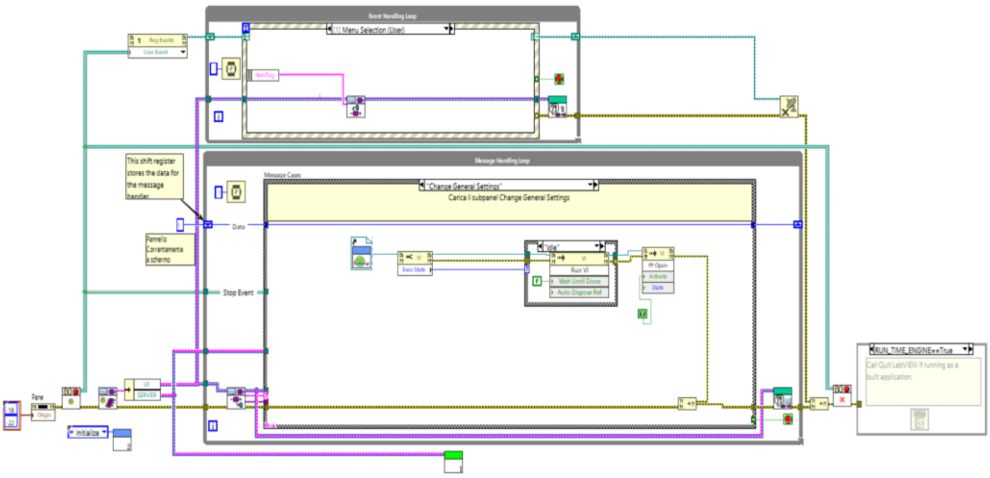

Figure 56 MHC Block Diagram (Code)

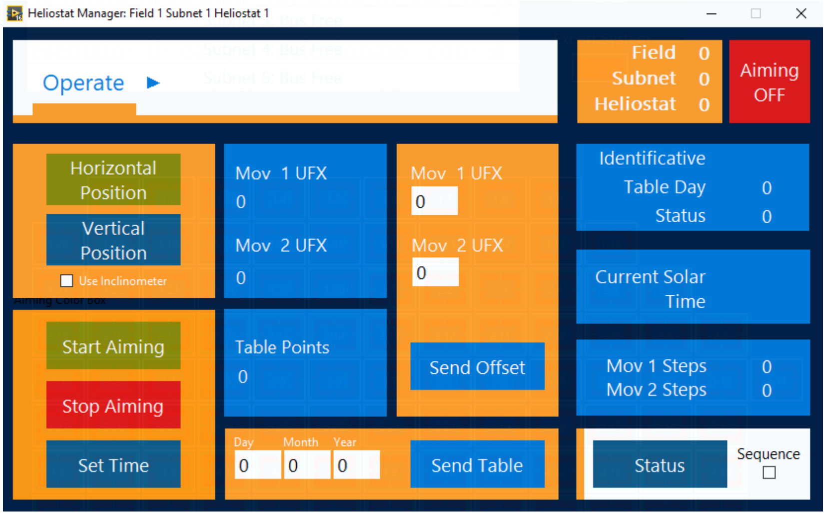

Figure 57 General screen single heliostat access

Figure 58 GUI library hierarchy

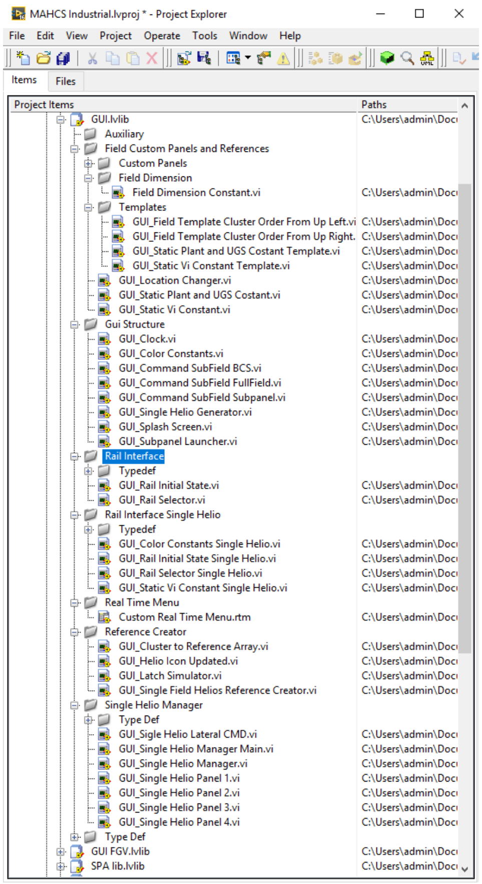

Figure 59 Organization of the GUI management library

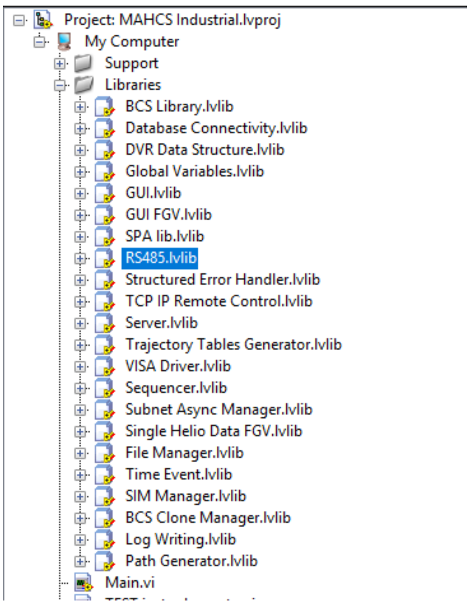

Figure 60 MHC Library Organization

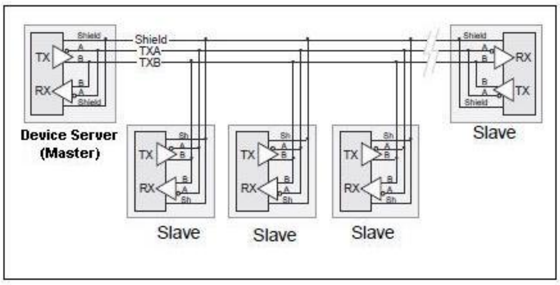

Figure 61 Communication Serial Bus Topology RS485:: Daisy Chain, Master-Slaves

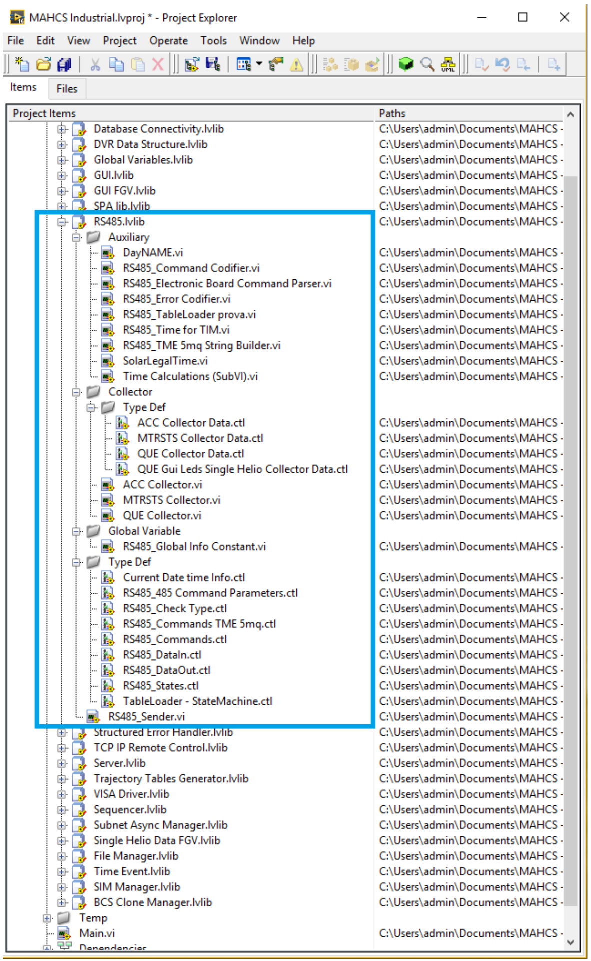

Figure 62 RS485 Library

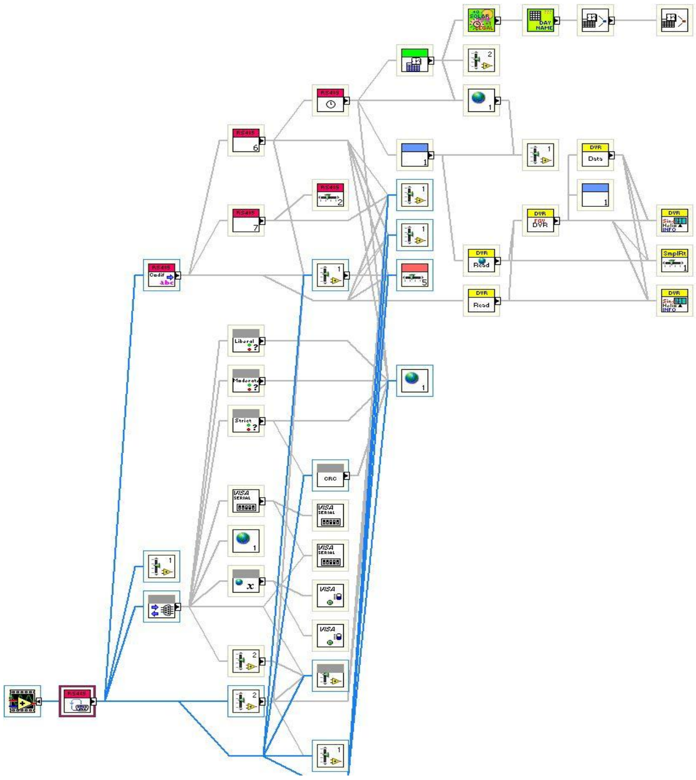

Figure 63 Structure of VIs, subVIs and RS485 data type

Appendix B
Analytical Evaluation Code

	Imm-H	Ceil-H	Fluid-H
Sand Mass [t]	36	36	36
Heaters Power [kW]	370	370	370
Fluidization Velocity Nominal [cm/s]	4	4	4
T_{Sand} Nominal Target [°C]	600	600	600

Table 17 Input parameters for Analytical Simulation

```
// INITIALIZATION
clear   // pulisce tutti le variabili
clc // pulisce variabili
clearglobal
close
xdel(winsid())  // close all figures
exec("heat_exchanger.sci");

// HEAT EXCHANGER
U=21    // relative to air heat exchanger
A_air=700;  // surface of air heat exchanger
mdot=5;

// SIZING IMMERSION HEATER
pow_density_nom=40000;  // W/m2
Pel_nom=2e6;  // MW
A=Pel_nom/pow_density_nom;   // m2 - surface immersed heater FOAK
d=0.1;  // m - outer diameter
L=A/(3.14*d);   // m - overall length resistances
h=350;  // W/m2/K - convective coefficiente sand-tube

// SYSTEM
m_sand=350000;
cp_sand=1100;
Tsand_max=680;
// DIFFERENCIAL EQUATION
Tsand=350;
Tsand_store=[Tsand];
Tres=Tsand;
Tres_store=[Tres];
dt=10;
t=0;
P_imm=[];
```

```
P_pre=[];
eta_store=[];

while Tsand<Tsand_max+20
    Tsand_pre=Tsand;
    // Immersion heaters
    P_immersion=Pel_nom*(1-exp(100*(Tsand_pre-Tsand_max)/Tsand_max))
    if P_immersion>Pel_nom
        P_immersion=Pel_nom
    end
    if P_immersion<0.05*Pel_nom
        P_immersion=0.05*Pel_nom
    end

    Tres=Tsand_pre+P_immersion/h/A
//    Tres=950;   // °C
//    h=350;
//
//    P_immersion=h*A*(Tres-Tsand_pre)
//    if P_immersion/A>pow_density_nom
//        P_immersion=pow_density_nom*A
//    end

    // Preheating
    [flux,T_hot_out,T_cold_out,cp]=NTU_flux_AirAir(U, A_air,mdot, mdot, Tsand_pre, 114)
    P_preheating=mdot*1000*(750-T_cold_out);
    P_pre_tobed=mdot*1000*(750-Tsand_pre);
    eta=P_pre_tobed/P_preheating;
//    P_preheating=eta*2*1e6; // MW
    if eta<100
        P_pre_tobed=0
    end
//    P_immersion=5e6-P_pre_tobed


    Tsand=(P_immersion+P_pre_tobed)/(m_sand*cp_sand)*dt+Tsand_pre;

    if abs(Tsand-680)/680<0.0001
        warm_up_time=t($)/3600; // h - warm up time
    end
        // ending
    P_imm=[P_imm P_immersion]
    P_pre=[P_pre P_pre_tobed]
    t=[t t($)+dt];
    Tsand_store=[Tsand_store Tsand]
    Tres_store=[Tres_store Tres]
    eta_store=[eta_store eta]
end
//Tsand0=350;
//t0=0;
```

```
//t=0:0.1:(10*3600);
//Tsand = ode(Tsand0,t0,t,f);
figure(1)
plot(t/3600,Tsand_store);
plot([0,t($)/3600],[680 680],'--r');
plot(t/3600,Tres_store,'g');
legend('Tsand (°C)','Ttarget (°C)','Tresistance (°C)',4);
xtitle( 'TES dynamic', 'Hour (h)', 'Tsand (°C)') ;          //title and labels
a=gcf();
a.background=8;
b=gca();
b.font_size=3
b.title.font_size=3
b.x_label.font_size=3
b.y_label.font_size=3
xstring(0.1,685,['Warm','up','time: ',string(floor(warm_up_time*100)/100),' h'])

figure(2)
plot(t(1:$-1)/3600,P_imm/1e6,'r')
plot(t(1:$-1)/3600,P_pre/1e6,'b')
xtitle( 'Power balances', 'Hour (h)', '(MW)') ; //title and labels
legend('Immersion heaters','Preheating system',4);
a=gcf();
a.background=8;
b=gca();
b.font_size=3
b.title.font_size=3
b.x_label.font_size=3
b.y_label.font_size=3
figure(3)
plot(t(1:$-1)/3600,eta_store,'r')
//plot(P_pre/1e6,'b')
xtitle( 'Efficiency preheating', 'Hour (h)', '(MW)') ;      //title and labels
//legend('Immersion heaters','Preheating system',4);
a=gcf();
a.background=8;
b=gca();
b.font_size=3
b.title.font_size=3
b.x_label.font_size=3
b.y_label.font_size=3
```

Appendix C

Ceil-heaters Experimental test

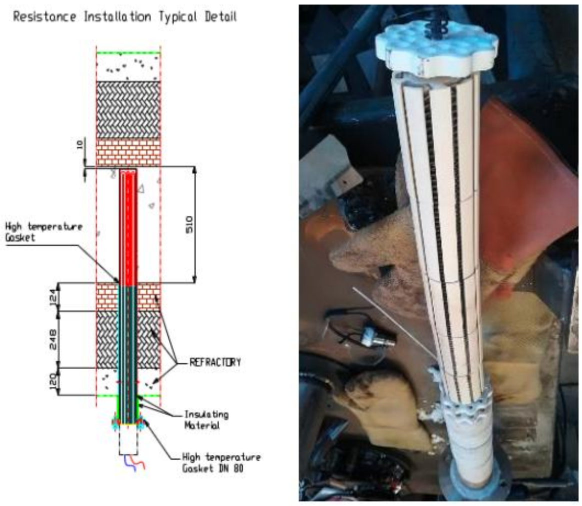

Figure 64 Picture of an immersion heater tested in fluidized bed (A)

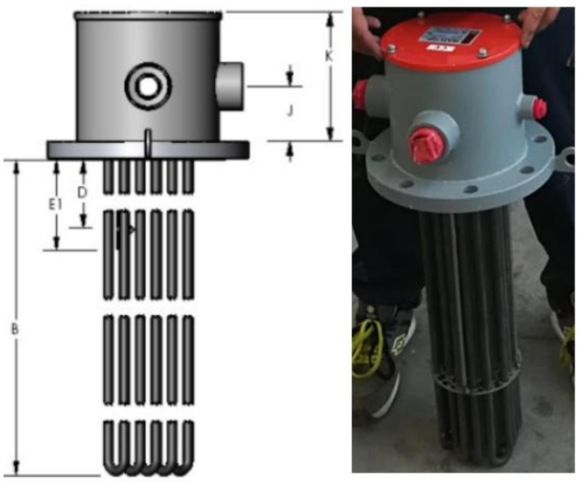

Figure 65 Picture of an immersion heater tested in fluidized bed (B)

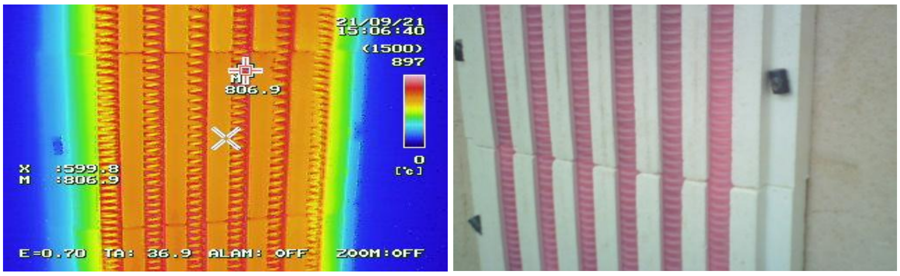

Figure 67 IR and visible frequency picture of Radiant Panel

Figure 68 Screen of Ceil-Heaters test

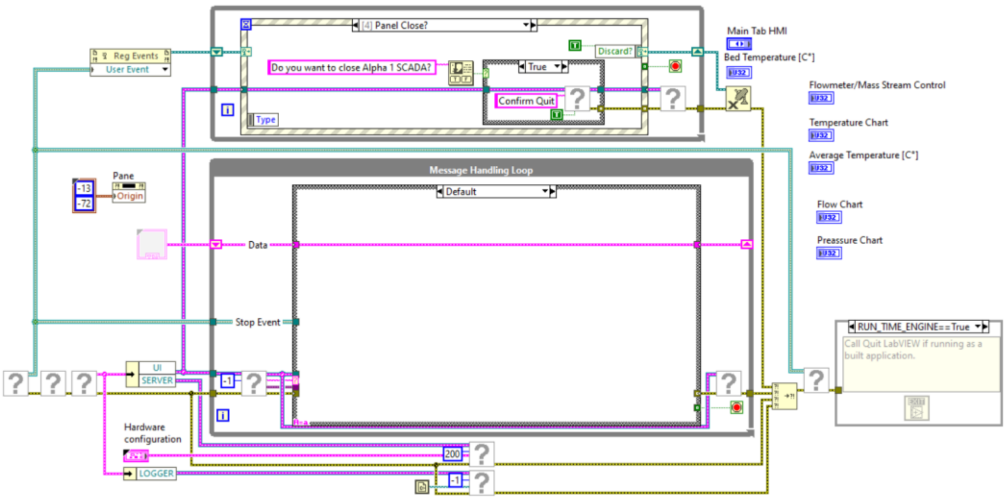

Figure 69 Screen of block diagram Ceil-Heaters test

Appendix D

Introducing to Optimization Model for a microgrid with integrated TES

The growing need to reduce carbon dioxide (CO_2) emissions in energy districts, particularly in the industrial sector, requires a new concept of controlled microgrid, where an optimal management of both, electrical and thermal resources, is required [99][100][101]. To ensure the optimal use of distributed energy resources, an adequate energy management system (EMS) is essential [102]. The nature of EMS optimization changes with the context (operational, planning and design). Different management objectives can be pursued, such as minimizing costs, reducing CO_2 emissions and maximizing reliability [103]. This can be done developing intelligent algorithms, modeling and optimization techniques [104][105], for example, mixed integer programming is used for a management strategy of a multi-energy multi-microgrid with combined heat and power generation [106]. For a multi-energy microgrid with electrical and thermal storage, a day-ahead forecast and a real-time dispatch model are used in a multi-stage optimal EMS.

This section points out just to introduce the optimization model mentioned with a preliminary basic set of equations used to characterize it. The model is based on a TES system for thermal management. The storage material can be heated by electric heaters to store thermal energy, also from renewable electric energy to produce green heat.

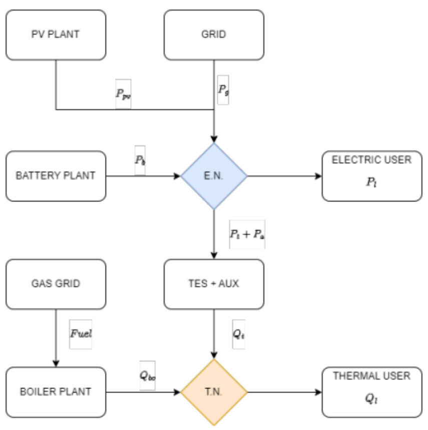

Figure 70 Microgrid power flows through electric and thermal nodes [107].

$P_{pv}[k] = N_{pv}P_{sp}\frac{G[k]}{G_{STC}}(1+\gamma_P(T_c[k]-T_{c,STC}))$
$T_c[k] = T_{air}[k] + \frac{T_{c,NOCT}-T_{a,NOCT}}{G_{NOCT}}G[k]$
$E_b[k] = (100\% - \sigma_b)E_b[k-1] - (P_b^-[k]\eta_b\Delta_t + \frac{P_b^+[k]}{\eta_b}\Delta_t)$
$Q_{st}[k] = (100\% - \sigma_t)Q_{st}[k-1] + (P_t^-[k]\eta_t\Delta_t + \frac{Q_t^+[k]}{\eta_t}\Delta_t)$
$T_s[k] = T_s[k-1] + M\frac{\{Q_{st}[k]-(100\%-\sigma_t)Q_{st}[k-1]\}\Delta_t}{m_{sm}c_{sm}}$

Table 18 Ppv is the output power of PV plant, Tc is the PV cell temperature, Eb is the remaining capacity (charge) of batteries, Qst is the thermal energy stored in the TES, Ts (storage temperature) represents the state of charge of TES

Research has been initiated to develop the EMS model aimed at optimizing power flows to reduce both energy costs and CO_2 emissions. This topic will form the core of future research efforts.

Acknowledgement

In questo lavoro di tesi sono racchiusi non solo gli sforzi maturati durante il percorso di dottorato, ma anche l'esperienza accumulata nell'intera mia carriera lavorativa, senza la quale le attività di ottimizzazione che hanno caratterizzato questi tre anni di dottorato industriale non sarebbero state possibili. Questo progetto di ricerca scientifica è stato orientato allo sviluppo e al miglioramento di tecnologie innovative dedicate alla decarbonizzazione e alla tutela del nostro pianeta, per contrastare il declino ambientale attuale. Questo è il nucleo e la motivazione che mi ha spinto, attraverso modelli matematici, simulazioni, algoritmi, e prove sperimentali – spesso condotte senza limiti di orario – ad affrontare con entusiasmo, dedizione e determinazione le sfide di questo cammino.

Un ringraziamento speciale va alla Magaldi Power, a Letizia e Raffaello Magaldi, ma in particolar modo al Cavaliere Mario Magaldi, la cui visione ambiziosa e il cui impegno nel perseguire gli obiettivi aziendali mi hanno ispirato a mettermi in gioco e a contribuire al raggiungimento di questi traguardi. Ho creduto profondamente in questa visione e continuo a crederci. Per questo ho investito mente, anima e corpo, percorrendo una strada che mi ha dato l'opportunità di seminare e raccogliere, di cadere e rialzarmi, accumulando esperienze di ogni tipo, che hanno arricchito il mio percorso umano e professionale. Indipendentemente dagli sviluppi futuri, resterò sempre legato a questo sodalizio, che tanto contribuisce allo sviluppo e al benessere del nostro territorio e a cui va la mia profonda stima e riconoscenza.

Un sincero grazie va ai miei Tutor, accademico e aziendale, Prof.ssa Maria Carmen Falvo e Ing. Rocco Sorrenti, per le preziose indicazioni e per il costante supporto offerto lungo questo percorso.

Se ho saputo affrontare con il giusto approccio le opportunità professionali incontrate, lo devo soprattutto ai valori di lealtà, coraggio, sincerità, rispetto per gli altri e dedizione alla famiglia che mi accompagnano. Con questi strumenti credo di aver affrontato al meglio le sfide quotidiane, tanto per me stesso quanto per gli altri. Di ciò ringrazio profondamente i miei genitori, Giovanni ed Antonietta, che con il loro esempio mi hanno trasmesso questi valori, lasciandomi sempre e comunque libertà di pensiero e di azione.

Il confronto sincero e costruttivo con mio fratello Luca mi ha aiutato a guardare le situazioni della vita in modo obiettivo, a volte persino distaccato dai miei stati emotivi; a lui va il mio ringraziamento per essere sempre stato presente e pronto al mio fianco.

Grazie alla mia Famiglia, che mi ha reso prima Marito e poi Papà di due splendidi bambini, Gianluca e Ilaria, dai quali ho imparato tanto, nonostante il molto che ancora hanno da apprendere. Alla mia amata Moglie Dalila va tutta la mia riconoscenza per essere un continuo sostegno nella mia crescita personale, professionale ed emotiva, una vera e propria metà di me stesso.

Un grazie speciale a Raffaele Pastore, amico prezioso, che mi ha insegnato il senso della praticità, del pragmatismo e del buon senso, applicabili a ogni contesto della vita.

Infine, grazie a Umberto, amico di una vita, sempre presente per condividere con me la realtà per come è e per come potrebbe essere.